CHEMICAL GENOMICS CENTRE
OF THE MAX PLANCK SOCIETY
MAX PLANCK INSTITUTE
OF MOLECULAR PHYSIOLOGY

technische universität
dortmund

IMPRS
FOR LIVING MATTER
International Max Planck
Research School

Structural basis for specific inhibition of the mitochondrial deubiquitinase USP30 revealed by chimeric protein engineering

Dissertation

For the achievement of the degree of

Doctor of Natural Sciences (Dr. rer. nat.)

Submitted to

Department of Chemistry and Chemical Biology

TU Dortmund University

by

Nafizul Haque Kazi

Dortmund, Germany

February 2025

The work presented in this thesis was performed during the period from January 2022 to December 2024 under the supervision of Dr. Malte Gersch at the Chemical Genomics Centre (CGC) of the Max Planck Society, the Max Planck Institute of Molecular Physiology (MPI), and the faculty of Chemistry and Chemical Biology at the TU Dortmund University.

1st Examiner: Dr. Malte Gersch

2nd Examiner: Prof. Dr. Dr. h.c. Herbert Waldmann

Supervisor: Dr. Malte Gersch

Disclaimer

All of the protein biochemistry and structural biology work presented in this dissertation, including protein engineering, molecular cloning, protein expression and purification, in vitro biochemical and biophysical characterization of wild type and mutant constructs, protein crystallization trials, X-ray crystallography data collection and X-ray structure solution, was performed by me.

Protein crystal data blending, final rounds of structure refinement, and PDB deposition of final protein structures were performed by Dr. Malte Gersch. All chemical compounds used in this study were synthesized by Nikolas Klink (Gersch group, CGC). All cellular assays were performed by Kai Gallant and Gian-Marvin Kipka (Gersch group, CGC).

The work presented in this dissertation has been published as a preprint in bioRxiv (*1*), and has also been accepted for publication in Nature Structural & Molecular Biology (December 2024).

Acknowledgements

First and foremost, I express my deepest gratitude to my PhD supervisor, Dr. Malte Gersch, for conceiving this project and providing unwavering support, mentorship, and inspiration throughout my PhD journey. Your guidance in designing experiments, analyzing data, and interpreting results has been invaluable. I am especially grateful for your trust, encouragement, and the opportunity to contribute to impactful research.

I would like to thank Nikolas Klink, Kai Gallant and Gian-Marvin Kipka for their collaborative spirit, expertise, and dedication. Working alongside you all has been a privilege, and I have learned so much from your insights and efforts in both chemical synthesis and cellular experiments.

I would like to express my gratitude to Prof. Herbert Waldmann for taking on the role of my second examiner, and for his vision in the establishment of the Chemical Genomics Centre, which has provided me with the opportunity to contribute to cutting-edge research in the field of chemical biology. The work in this dissertation would not have been possible without the generous funding provided by the Chemical Genomics Centre (AstraZeneca, Merck KGaA, Pfizer Inc., and Max Planck Society, CGCIII-352S) and the German Research Foundation (DFG, CRC1430, 424228829). I also acknowledge the additional support from an Emmy Noether grant (DFG, GE 3110/1-1) and the State of North Rhine-Westphalia's CANcer TARgeting Network (NW21-062C), which significantly bolstered the Gersch lab's research endeavors.

I acknowledge the X-ray beamtime provided by the European Synchrotron Radiation Facility (ESRF) and sincerely thank Raphael Gasper and Petra Geue of the MPI ZE-CB for their technical expertise and support during crystallization studies. Your assistance was pivotal in overcoming the challenges of structural biology and driving my research forward. A special thanks goes to the

Max Planck Computing & Data Facility for the provision of computing resources, which greatly helped in the analysis of complex X-ray crystallography data.

I am profoundly grateful to all members of the Gersch lab for fostering a stimulating and collaborative environment. Your thoughtful discussions, advice, and expertise enriched my work in countless ways. A special thanks to Dr. Rachel O'Dea and Kai Gallant for helping me to get settled in the lab and ensuring that my stay in Dortmund was comfortable.

I would like to extend my gratitude to the outstanding staff at the BMZ, CGC, MPI Dortmund and TU Dortmund University for their excellent support and infrastructure. A special thanks to Dr. Lucia Sironi, Christa Hornemann, and Antje Peukert of the MPI welcome office for their constant support and guidance throughout my stay in Dortmund and taking care of all the administrative technicalities of visa, residence, and the PhD curriculum, thus helping me to focus solely on my research and making my life easier.

Finally, I am deeply thankful to my family for their support and unwavering belief in me. I will forever be grateful to my parents for their sacrifices and support throughout my academic journey from the early school days to B.Sc. and M.Sc., so that I could ultimately reach at this level today obtaining my PhD. I would like to thank my elder sister with whom I have always discussed my academic and career decisions. She has always helped me in taking decisive steps and navigating through all kinds of technicalities at all the stages of my academic life such as filling forms, submitting applications, making payments, visa applications and many more, and I am really thankful for her support throughout my academic journey. To my parents and my sister - your love, support and encouragement have been my anchor through the challenges and triumphs of this journey.

Contents

Abstract

The mitochondrial deubiquitinase USP30 is a key antagonistic regulator of mitophagy. The potential of USP30 inhibition as a therapeutic strategy for Parkinson's disease is currently being explored in clinical trials. However, the molecular basis for specific inhibition of USP30 by small molecules has remained elusive because of the limited crystallizability of USP30. This dissertation reports the crystal structure of human USP30 in complex with a specific inhibitor, enabled by chimeric protein engineering. The thesis uncovers a unique mode of deubiquitinase inhibition in which the inhibitor extends into a cryptic pocket facilitated by a compound-induced conformation of the USP30 switching loop. The thesis underscores the potential of exploring induced pockets and conformational dynamics to obtain specific deubiquitinase inhibitors and identifies underlying USP30-specific residues. More broadly, the obtained structure helped to delineate a conceptual framework for specific USP deubiquitinase inhibition based on a common ligandability hotspot in the Leu73-Ubiquitin binding site and on diverse compound extensions. Collectively, this dissertation establishes a generalizable chimeric protein engineering strategy to aid deubiquitinase crystallization and enables structure-based drug design with relevance to neurodegeneration.

Zusammenfassung

Die mitochondriale Deubiquitinase USP30 ist ein wichtiger antagonistischer Regulator der Mitophagie. Das Potenzial der Hemmung von USP30 als therapeutische Strategie für die Parkinson-Krankheit wird derzeit in klinischen Studien untersucht. Die molekulare Grundlage für die spezifische Hemmung von USP30 durch kleine Moleküle ist jedoch aufgrund der begrenzten Kristallisierbarkeit von USP30 noch nicht bekannt. Wir stellen hier die Kristallstruktur von humanem USP30 im Komplex mit einem spezifischen Inhibitor vor, der durch chimäres Protein-Engineering ermöglicht wurde. Unsere Studie deckt einen einzigartigen Modus der Deubiquitinase-Hemmung auf, bei dem der Inhibitor in eine kryptische Tasche eindringt, die durch eine durch die Verbindung hervorgerufene Konformation der USP30-Schaltschleife erleichtert wird. Unsere Arbeit unterstreicht das Potenzial der Erforschung induzierter Taschen und der Konformationsdynamik zur Gewinnung spezifischer Deubiquitinase-Inhibitoren und identifiziert die zugrunde liegenden USP30-spezifischen Rückstände. Darüber hinaus hat uns die erhaltene Struktur geholfen, einen konzeptionellen Rahmen für die spezifische USP-Deubiquitinase-Inhibition zu entwerfen, der auf einem gemeinsamen Ligandabilitäts-Hotspot in der Leu73-Ubiquitin-Bindungsstelle und auf verschiedenen Verbindungserweiterungen basiert. Zusammenfassend lässt sich sagen, dass unsere Arbeit eine verallgemeinerbare Strategie für die Entwicklung chimärer Proteine zur Unterstützung der Deubiquitinase-Kristallisation darstellt und ein strukturbasiertes Wirkstoffdesign mit Relevanz für die Neurodegeneration ermöglicht.

1. Introduction

1.1. The ubiquitin system

Ubiquitination is a highly conserved post-translational modification, primarily earmarking substrate proteins for degradation. This critical modification is highly conserved and regulates nearly all cellular processes of the eukaryotic system through a combination of proteolytic processing of proteins and non-proteolytic pathways such as cell signaling networks, protein-protein interactions, subcellular localization of proteins, cell cycle regulation, DNA repair systems and apoptosis (*2*, *3*).

The ubiquitin system operates as a multi-enzyme system that organizes free ubiquitin into a complex molecular code that governs the cellular fate of substrate proteins (*4*). The ubiquitin code is written by the covalent attachment of ubiquitin - a small regulatory protein of 76 amino acids, by the action of the E1 E2 E3 enzyme cascade. Ubiquitin can be attached to substrate proteins as monoubiquitin or polyubiquitin with a variety of distinct architectures. Specific architectural types of ubiquitin chains are recognized by ubiquitin binding domains which are called the readers of the ubiquitin code. The specific interactions between distinct ubiquitin chains and their corresponding readers determine the cellular fate of target proteins. Deubiquitinating enzymes (DUBs) are a class of ubiquitin code erasers that play a counter-regulatory role in the ubiquitin system. These enzymes reverse ubiquitin modifications on target substrates, thus counteracting the E3 ligases. The balance in between the activity of E3 ligases and DUBs is critical in regulating cellular processes **(Fig. 1a)**.

Dysregulation of the ubiquitin system is implicated in a wide array of diseases, such as cancer, neurodegenerative diseases, inflammation and immune disorders and cardiovascular diseases. Given its pivotal role in such pathologies, the ubiquitin system has emerged as a promising therapeutic target with ongoing development of proteasome inhibitors, E3 ligase modulators, DUB inhibitors and Proteolysis targeting chimeras (PROTACs). By advancing our understanding of the ubiquitin system, particularly in the context of disease mechanisms, critical biological processes can be unraveled, and novel therapeutic strategies can accordingly be developed.

1.2. Building the ubiquitin code: E1, E2, E3 ligases

Ubiquitin is covalently attached to lysine residues of substrate proteins via isopeptide linkage in between the carboxyl group of the ubiquitin C-terminal glycine and epsilon amino group of the substrate lysine. The attachment of ubiquitin to substrates is driven by the coordinated action of E1 (ubiquitin activating enzyme), E2 (ubiquitin conjugating enzyme) and E3 (ubiquitin ligase) **(Fig. 1a)**.

Ubiquitin is first activated by attachment to cysteine residue of E1 by a thioester linkage which is driven by ATP hydrolysis. The ubiquitin is then transferred to cysteine residue of E2 enzyme through a trans-esterification reaction. The ubiquitin-E2 complex then interacts with E3 enzyme to facilitate transfer of ubiquitin to substrate proteins (*5*). The E3 enzyme has substrate recognition domains and often by themselves or in concert with ubiquitin-E2 complexes provide the specificity for ubiquitination of target substrates.

Depending on the cellular process, substrates can be modified by the addition of a single ubiquitin molecule (monoubiquitination) or a chain of ubiquitin molecules (polyubiquitination).

Polyubiquitin chains are formed when the C-terminal Gly of an incoming ubiquitin molecule (distal ubiquitin) attaches to any of the seven lysine residues of the ubiquitin already attached to the substrate (proximal ubiquitin) via isopeptide linkage. The typical polyubiquitin linkages are Lys6-, Lys11-, Lys27-, Lys29-, Lys33-, Lys48, Lys63-linked polyubiquitin chains (*6*). The nature of the polyubiquitin chain often determines the fate of the substrate protein.

1.3. Arrangement of the ubiquitin code: distinct ubiquitin chain structures affect cellular fate

Polyubiquitin chains on substrate proteins attain diverse chain architectures, encoding information for distinct cellular outcomes **(Fig. 1b-c)**. The ubiquitin code is further modulated by the specific conformations of different chain types. Lys48-, Lys11- and Lys6-linked chains are compact, where adjacent ubiquitin moieties interact with each other through an interface. In contrast, Lys63- and Met1-linked chains exhibit open conformations, where adjacent ubiquitin moieties do not interact with each other through any interface other than the linkage itself. These structural differences result in differential recognition by ubiquitin binding domains (UBDs). Compact ubiquitin chains are recognized by UBDs that exploit the geometry attained by the interacting interfaces of ubiquitin moieties, whereas open ubiquitin chains are recognized by UBDs that exploit the distance in between the ubiquitin moieties. The differential binding of UBDs to specific ubiquitin chain structures dictates the cellular fate of ubiquitinated substrates, forming the basis of the ubiquitin code (*7*).

1.4. Decoding the ubiquitin code: UBDs

Certain proteins contain ubiquitin binding domains (UBDs) that facilitate the recognition of specific ubiquitin modifications on proteins, thus interpreting the ubiquitin code. Translating the ubiquitin code is a mechanism of the UBDs by which they can also distinguish between different ubiquitin chain architectures. This distinction is done based on the differential chain structure, flexibility and geometry of ubiquitin molecules within the chains. For instance, Rap80 contains two spatially separated UBDs that can conveniently recognize extended Lys63-linked chains but not the compact Lys48-linked chains. So, Rap80 exploits the distance in between the ubiquitin molecules within the chain. Conversely, Ataxin-3 has two closely-spaced UBDs that prefer binding to the compact Lys48-linked chains over the extended Lys63-linked chains (*8, 9*).

UBDs can also distinguish between structurally similar chain types by exploiting the flexibility of the ubiquitin chain and the geometry of the individual ubiquitin molecules within the chain. For example, the structurally similar Lys63- and Met1-linked chains are distinguished by a certain UBD called Npl4-like zinc fingers (NZFs). Crystal structure of NZF bound to Lys63-linked diubiquitin shows that the ubiquitin molecules are bent at 90° such that the Ile44 patch of each ubiquitin molecule interacts with the same NZF (*10, 11*). Such bending flexibility is not observed for Met1-linked chains. Conversely, UBD of NEMO subunit of IkB kinase forms a dimer that can recognize Met1-linked chains by interacting with the Ile44 patch of distal ubiquitin and Phe4 patch of proximal ubiquitin. These interactions are not possible for Lys63-linked chains because of the different geometry of the ubiquitin molecules in these chains that do not give access to the Phe4 patch crucial for this interaction. (*12, 13*).

UBDs are also present in certain eraser proteins called deubiquitinases. These enzymes remove ubiquitin modifications from substrates, thereby regulating the ubiquitin system.

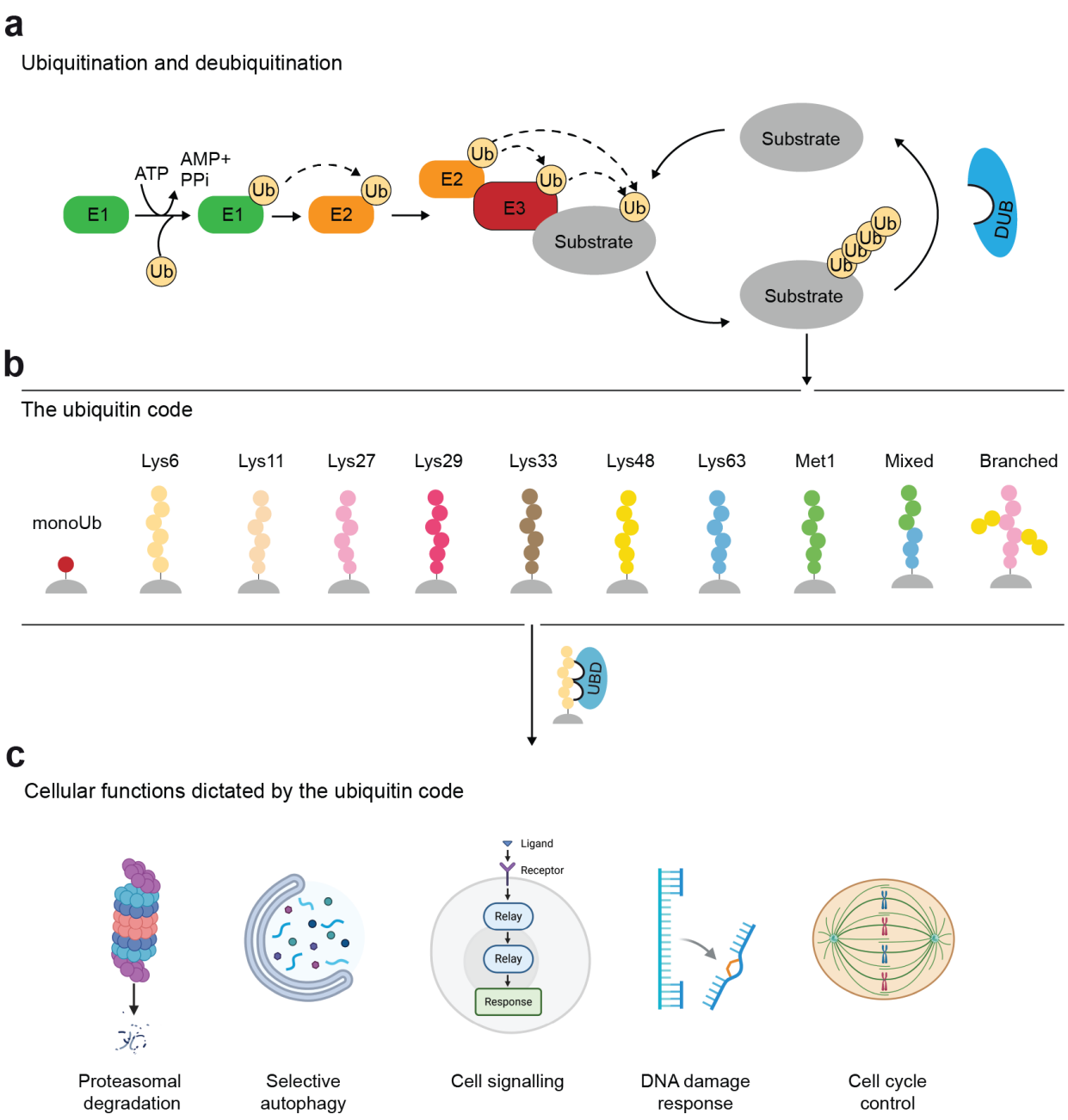

Figure 1 | Overview of the ubiquitin system.

a, The process of ubiquitination and deubiquitination of target substrate proteins. **b,** Arrangement of the ubiquitin molecules on the substrate protein laying the basis of differential recognition by ubiquitin binding domains (UBDs). **c,** Cellular functions dictated by the ubiquitin code. Figures adapted from Damgaard et. al., 2021 (*2*).

1.5. Deubiquitinases: Balancing the ubiquitin system

Deubiquitinases (DUBs) are a class of proteases that reverse ubiquitination by cleaving ubiquitin molecules from target substrates. In doing so, DUBs oppose the E3 ligases. The balance in the activities of DUBs and E3 ligases is crucial in regulating critical cellular processes **(Fig. 2)** (*14*). Dysregulation of DUBs is involved in various cancers, inflammation, immune disorders and neurodegenerative diseases (*15-21*) and therefore DUBs are emerging as effective drug targets.

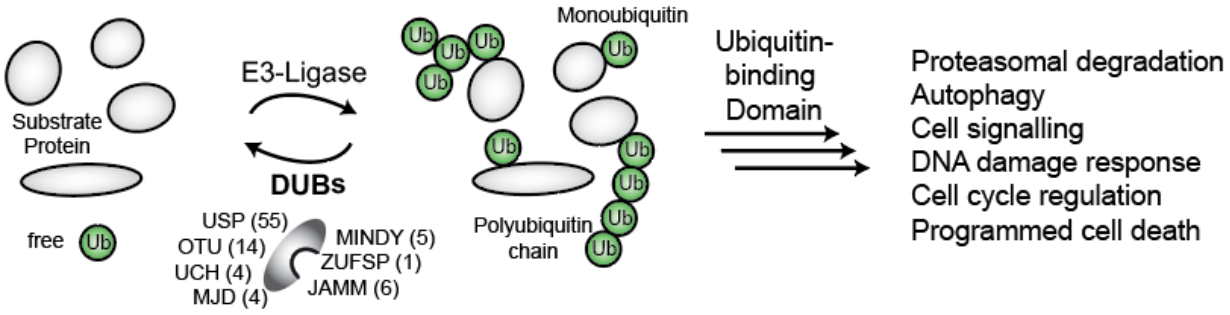

Figure 2 | Overview of DUBs counteracting E3 ligases.
Deubiquitinating enzymes (DUBs) counteract E3 ligases by removing ubiquitin modifications from target substrates, subsequently regulating cellular processes.

1.5.1. Classification of DUBs

Based on the mechanism of their catalytic activities, DUBs are classified into two classes: the cysteine proteases and the metallo proteases (*22, 23*). In humans, the cysteine protease class of DUBs comprises over 80 proteins and is the best characterized class in terms of domain annotation, structure, function and inhibition (*24, 25*). The cysteine protease class of DUBs is further divided into six families according to similarities in specific functional domains, protein fold and dynamics: the ubiquitin specific proteases (USPs, 55 members), the ubiquitin C-terminal hydrolases (UCHs, 4 members), ovarian tumour domain containing proteases (OTUs, 14

members), Machado-Josephin disease proteases (MJD, 4 members), tandem motif interacting with ubiquitin (MIU) domain containing proteases (MINDY, 5 members) and zinc finger with ubiquitin fold modifier domain containing proteases (UFM, 1 member) (*25-29*).

The metallo protease class of DUBs contains enzymes with JAB1/MPN1/MOV34 (JAMM) domain with 6 members capable of hydrolyzing ubiquitin conjugates. These enzymes contain a zinc ion at the catalytic site which facilitates hydrolysis of isopeptide linkage in ubiquitin chains (*30*).

USPs are by far the largest family of DUBs and are the most significant in terms of structural characterization, cellular functions and drug targeting potential.

1.5.2. Ubiquitin specific proteases (USPs)

The human genome encodes 55 USPs, which are similar in their domain architecture and protein fold, but differ in the length of their catalytic domains, subcellular localization and subsequently cellular functions. The need for USPs to evolve into such a large family can be explained by the innovation, amplification and divergence (IAD) model (*31, 32*), which implicates that USPs have evolved from a shared common ancestor as is reflected by the presence of conserved domains and protein folds across the different USPs. However, their diverse functions reflect evolutionary modifications leading to divergence from the common ancestor. Such divergence pattern began when deubiquitination became a dynamic process and was involved in numerous critical cellular processes. With evolving organismal complexity, these functions became more complex and so a dormant portion of the ancestral gene may have been required for this newly evolved function (Innovation). This portion of the gene was positively selected and amplified over generations (Amplification), ultimately causing it to diverge from the ancestral gene (Divergence), and give

rise to a different gene which is highly similar to the ancestral gene but has different function because of the amplification of a specific portion of the gene. With evolving organismal complexity, deubiquitination functions became more complex and thus USPs duplicated at several points in evolution to have different functions, and this gave rise to such a large number of USPs present now. A specific example is the evolution of the USP16-HERC2 interaction. A primitive USP16/45 gene may have had a rudimentary coiled coil domain. Its interaction with HERC2 was found to be favourable and therefore this coiled coil domain was amplified over generations in USP16 which led to its divergence from USP45. So USP16 and USP45 are highly similar in sequence but have varied functions. This is how homologous USPs have variations, resulting in the wide repertoire of USP functionalities (*31*).

Despite their diverse functions, USPs have statistically significant similarities in their sequence and structure. Some hallmark features of USP DUBs are: (i) Papain cysteine protease fold with catalytic triad composed of Cys, His and Asp/Asn/Ser **(Fig. 4b)**. (ii) Aromatic gatekeeper residue adjacent to the catalytic His. which allows entry of only the GG motif of ubiquitin C-terminus into the active site **(Fig. 4b)**. (iii) Blocking loops and a switching loop which guard the active site preventing unnecessary activation of USPs and coordinates switch between inactive and active state upon ubiquitin binding **(Fig. 4a)**. (iv) Conserved residues at the major ubiquitin binding site that recognize ubiquitin through its Ile44 patch and form salt bridge interactions with the LRLRGG motif of the Ub C-terminus tail, thus guiding the tail into the active site. These USP residues form the so-called ubiquitin binding domains (UBDs) (v) Conserved hydrophobic pocket that anchors the ubiquitin Leu73 side chain, facilitating the entry of ubiquitin C-terminus into the active site **(Fig. 4a)** (*25, 33*).

1.5.3. Domain architecture, structure and dynamics of USP DUBs

USP DUBs have the major USP catalytic domain where important ubiquitin binding dynamics and ubiquitin-chain cleavage chemistry occur. In addition to the USP catalytic domain, some USPs have various ubiquitin binding domains (UBDs) which include the ubiquitin-associated (UBA) domain, ubiquitin-interacting motif (UIM), zinc finger ubiquitin specific protease domain (ZnF-UBP) and ubiquitin like domains (UBLs). These UBDs facilitate the binding of ubiquitin to support the function of the USP catalytic domain. The domains across USPs have low sequence homology and vary in length, however they adopt similar protein folds. The USP catalytic domain forms open-handed conformation and the UBDs have similar fold as ubiquitin, and these structural features are conserved across all USPs (*34*).

The USP catalytic domain adopts a hand-like structure and is divided into the thumb, palm and fingers subdomains **(Fig. 3a)**. The catalytic site is at the center of the thumb and palm subdomains. The palm subdomain forms the β-sheet rich core of USP, the thumb subdomain is mostly helical and forms the proximal ubiquitin binding site, and the fingers subdomain consists of 4 large β-sheets and forms the major distal ubiquitin-binding site. Most USPs coordinate zinc at the tip of their finger subdomains (*25*, *34*) **(Fig. 7b)**.

The USP catalytic domain is further subdivided into six conserved boxes based on sequence conservation **(Fig. 3b)**. Box 1 starting from the N-terminus has the conserved GNTC motif carrying the catalytic Cys. Box 1 also has conserved Asn and Gln residues close to the catalytic Cys, which form oxyanion hole facilitating the catalytic mechanism of USP DUBs **(Fig. 4b)**. Box 2 has a conserved QQD motif, where the Asp is absolutely conserved across all USP DUBs. Boxes 3 and 4 have conserved CxxC motifs that coordinate zinc in most USP DUBs. Interestingly, the USP DUBs that lack zinc coordination have a higher representation among the structurally

characterized USP DUBs **(Table 1)**, indicating higher crystallization propensity of these zinc-free DUBs, which is the basis of the chimeric protein engineering strategy presented in this dissertation (more details in **Section 2.1**). Box 5 has the conserved GHY motif, carrying the catalytic His and an adjacent aromatic gatekeeper Tyr. Box 6 has the conserved Asp/Asn as the third catalytic residue with an adjacent Asp which is even more highly conserved and forms a fourth critical residue shown to be important for catalytic activity in certain DUBs (*35*) **(Section 1.5.4.)**. Using USP7 as a model structure, mapping the boxes show that Boxes 1 and 2 form the helical thumb subdomain, boxes 3 and 4 form the extended beta-sheets of the finger subdomain, including the zinc finger motif CxxC, and boxes 5 and 6 form the palm subdomain having the beta-sheet core of the protein **(Fig. 3b)** (*36*).

Expanding this box subdivision to the structure of other USPs interestingly reveals the presence of common insertion points in between the boxes across all USPs **(Fig. 3b)**. Insertions at these points can fold into motifs/domains of different sizes and structure across all USPs, and may serve specific functions. The reason for the presence of insertions in the USP catalytic domain could be explained by the IAD model (*31*), according to which certain portions added to the USP catalytic domain adapted certain conformations to serve certain functions over time. These insertions in some USPs have been mostly conserved and have evolved to form motifs/domains with specific functions, while in other USPs they have low conservation (*25, 34*) and have become rudimentary remains of once existing functional units, which don't serve any specific purpose now, and can instead be exploited for engineering the USP catalytic subdomain for structural studies **(Table 1; Section 2.1)**. Most common insertions are between boxes 3 and 4 and boxes 4 and 5. Insertions between boxes 3 and 4 reside in the finger subdomain forming the ubiquitin-like (Ubl) domain, which could directly affect distal ubiquitin binding. 8 USPs have the Ubl domain - USP4, USP6,

USP11, USP15, USP19, USP31, USP32, USP43. Insertion between boxes 4 and 5 extend the platform for ubiquitin binding. These insertions form ubiquitin associated domains (UBA) in USP5 and USP13, while in USP37 they form Ubiquitin interacting motifs (UIM). CYLD contains a B-box insertion at this point which does not interact with ubiquitin, but is important for protein interactions and localization. Insertions between boxes 1 and 2 might affect proximal ubiquitin binding which gives linkage specificity to DUBs such as the pronounced Lys63-linkage specificity of CYLD and AMSH. Insertions between boxes 2 and 3 and boxes 5 and 6, which are away from the catalytic site, have not been predicted to form ubiquitin-like folds and are not known to have particularly important roles in USP function (*25*).

USPs thus have a modular architecture in which the USP subdomains work in concert to facilitate ubiquitin substrate binding to USP and guide the substrate to the active site for efficient cleavage of ubiquitin chains.

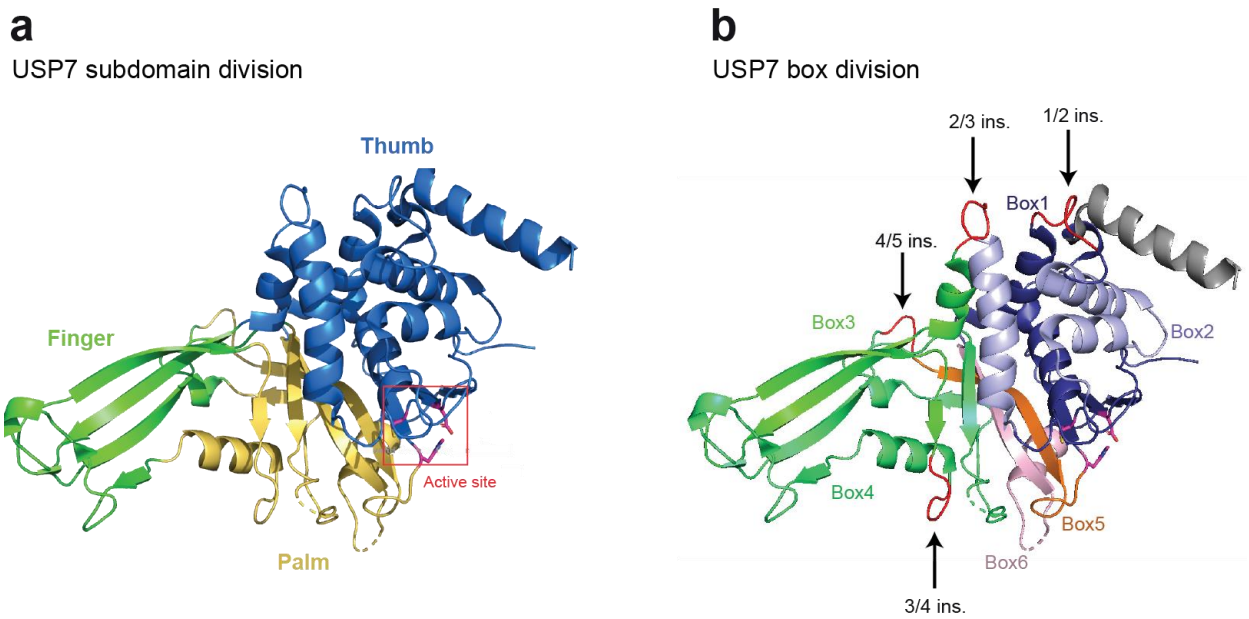

Figure 3 | Architecture of the USP catalytic domain.
a, Cartoon representation of USP7 catalytic domain (PDB: 1NB8) highlighting the different subdomains and the active site. **b,** Cartoon representation of the same protein as in panel a, highlighting box subdivision of the USP7 catalytic domain and common insertion points.

1.5.4. Mechanism of USP DUB activity

USP fingers subdomain forms the major distal ubiquitin binding surface (S1 site), which is the primary ubiquitin interaction surface as it covers up to 40% of the ubiquitin surface **(Fig. 4a)**. Interaction with the proximal ubiquitin (S1' site) in the thumb subdomain is less extensive. Distal ubiquitin sits on the finger subdomain through its Ile 44 patch. The C-terminus of ubiquitin then extends towards the catalytic site, which is located at the interface of the palm and thumb subdomains (*4, 25*) **(Fig. 4a-b)**. The ubiquitin C-terminus is guided towards the catalytic site by anchoring of the ubiquitin Leu73 side chain in a conserved hydrophobic USP pocket (*37*) **(Fig. 4a)**. Also, the ubiquitin C-terminus is held in place by salt bridge interactions of the LRLRGG motif of ubiquitin C-terminus with conserved residues in the ubiquitin binding interface at the USP fingers subdomain. Further, a gatekeeper aromatic residue adjacent to the catalytic His. **(Fig. 4b)** ensures that only the GG motif of the ubiquitin C-terminus tip is able to enter the active site and prevents entry of other amino acids with more bulk, thus contributing to specificity of USPs towards ubiquitin (*33*).

The activity of USP DUBs is tightly regulated such as to prevent leaky or aberrant ubiquitin chain cleavage activity. DUB activity is ensured only when ubiquitin substrate binds to the enzyme. Certain DUBs such as USP7 are inactive in the apo state, with the catalytic triad misaligned. Distal ubiquitin binding to USP7 causes conformational changes leading to alignment of the catalytic triad (*38*). Other DUBs such as USP14 are already active, with an aligned catalytic triad. However, ubiquitin C-terminus entry to the active site is occluded by the presence of blocking loops and a switching loop **(Fig. 4a)**. Distal ubiquitin binding induces conformational changes in these loops thus opening the pathway for ubiquitin C-terminus into the active site (*39*).

The canonical catalytic triad at the active site consists of conserved Cys, His and Asp/Asn. Structural superposition shows that the positioning of the catalytic residues is highly similar across USPs (*40*). In the active conformation of the catalytic triad, His and Asp are connected through H-bonding and the His is positioned such that it also forms H-bond with the Cys. The classical mechanism of USP enzyme activity **(Fig. 4b)** dictates that the Cys residue is the primary nucleophile that attacks the carbon of the carbonyl group in the ubiquitin isopeptide linkage. The His acts as the proton donor/acceptor and activates the Cys for nucleophilic attack. The His in turn is stabilized in position by the Asp/Asn. Upon the execution of this mechanism, the oxygen of the carbonyl group in the ubiquitin isopeptide linkage forms an oxyanion, which is stabilized by a network of H-bonds formed by the adjacent residues (*38*).

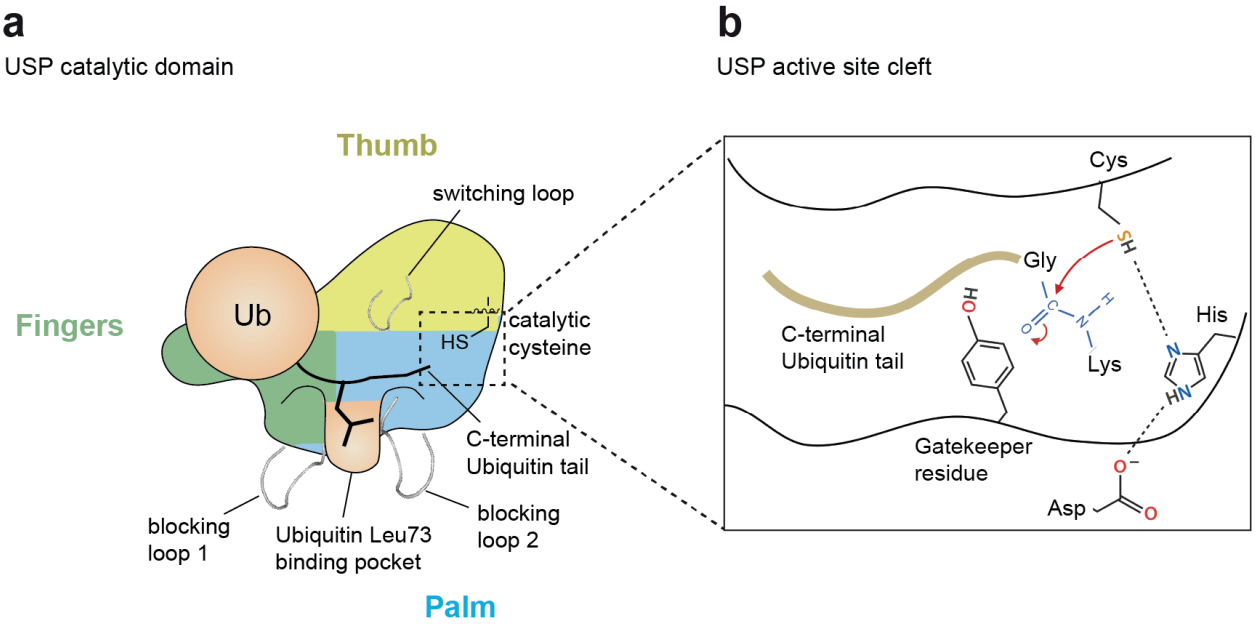

Figure 4 | Ubiquitin binding and USP active site mechanisms.
a, Illustration highlighting the major ubiquitin binding site on the USP catalytic domain. **b,** Illustration highlighting the entry of the ubiquitin C-terminal tail into the active site and subsequently the reaction mechanism involving the catalytic residues.

Though the positioning of the catalytic triad is highly conserved, some variability exists in the roles of these residues. It has been found that there is a 4th critical Asp residue, adjacent to the 3rd critical Asp/Asn, that is actually necessary for enzyme activity in USP1, USP15, USP40 and USP48, while in USP7, the canonical 3rd critical Asp is the crucial residue for enzyme activity. Such plasticity in the roles of the catalytic triad residues opens up new opportunities for selective targeting of different USPs involved in various diseases (*35*).

1.6. Role of USP DUBs in diseases and drug discovery efforts

1.6.1. Rationale of targeting DUBs

USP DUBs are involved in critical cellular processes in which they maintain protein and ubiquitin homeostasis and regulate protein functions, localization and interactions. It is no wonder that USP DUBs are involved in various diseases, and hence are attractive drug targets **(Fig. 5)**.

The advantage of targeting DUBs is that it can help indirectly target proteins that are difficult to target or are undruggable. Certain transcription factors, drug resistant enzymes and proteins that structurally lack specific ligand-binding features fall under the undruggable category. An example is the DUB USP28 which promotes tumor progression by stabilizing the oncoprotein c-MYC, which is notorious for being undruggable (*41*). A highly selective USP28 inhibitor treatment significantly reduced c-MYC levels and substantially regressed lung cell carcinoma in a murine model, thus confirming that difficult to target proteins can be targeted indirectly via USP DUB inhibition. This also highlights that specific DUB inhibition will amplify the ubiquitination and subsequent degradation of only the specific substrates of the DUB without altering the global ubiquitin and protein levels (*42*).

1.6.2. Targeting USP DUBs with small molecule inhibitors

1.6.2.1. USP14 inhibitors

USP14 regulates proteasomal degradation. Its inhibition has been explored for potential therapeutic benefits, particularly in neurodegenerative diseases, by enhancing proteasomal activity and reducing pathological protein accumulation (*43*). Structure activity relationship (SAR) studies led to the development of IU1-47 **(Fig. 5)** as a potent (IC_{50} = 0.6 μM) and selective USP14 inhibitor. IU1-47 treatment was shown to enhance proteasomal activity and reduce Tau levels in neurons (*44*). Co-crystal structures of IU1-analogs highlight a unique steric blockade mechanism in which the inhibitor sterically blocks entry of ubiquitin C-terminus into the USP14 active site, explaining the basis of high selectivity of these class of compounds (*45*).

1.6.2.2. USP2 inhibitors

USP2 was found to deubiquitinate and stabilize cyclin D1, a major factor in cancer progression. USP2 knockdown was found to arrest growth in cyclin D1 expressing cell lines (*46*), thus providing the rationale of targeting USP2 to halt the progression of cyclin-D1 driven cancer by inducing cyclin D1 degradation.

A high throughput screening (HTS) campaign screened >200,000 compounds and optimized hits to develop ML364 **(Fig. 5)**, a 1.1 μM USP2 inhibitor (*47*). ML364 demonstrated good absorption, distribution, metabolism and excretion (ADME) properties and effectively reduced cyclin D1 levels in cancer cell lines. It was selective against 102 kinases and four non-DUB proteases but showed strong activity against USP8. However, ML364 was only tested against two DUBs and not assessed in a panel of all USP DUBs, leaving potential off-target effects uncharacterized.

Another group independently performed a saturation transfer difference (STD) NMR-based fragment screen targeting USP2 (*48*). They found one hit, STD1T **(Fig. 5)**, that inhibited USP2 (3.3 μM IC50). STD1T was confirmed to induce cyclin D1 degradation, and is a promising starting point for lead optimization.

1.6.2.3. USP7 inhibitors

USP7 is a highly expressed DUB involved in multiple disease pathways, particularly through its regulation of p53 and MDM2 (*49*). With MDM2 inhibitors entering clinical trials, USP7 inhibition provides an alternative strategy to stabilize p53 and promote tumour suppression. Various USP7 inhibitors have been developed, with a series of 4-hydroxypiperidines (*50*) emerging as an effective class of USP7 inhibitors.

Crystal structure of USP7 in complex with a highly selective and potent 4-hydroxypiperidine compound FT671 (IC_{50} = 52 nM) **(Fig. 5)**, highlights the basis of compound potency and selectivity. FT671 binds at a dynamic pocket near the USP7 active site in its auto-inhibited apo state, which is different from other USP DUBs. This structural revelation was supplemented with cellular studies in which FT671 was found to destabilize USP7 substrates including MDM2, increased levels of p53, and resulted in the transcription of p53 target genes, subsequently inhibiting tumour growth in mice (*50*).

Further structure-based drug development led to the emergence of a class of ether-linked pyrrolidine compounds as reversible inhibitors of USP7. Among these, compound 23 **(Fig. 5)** emerged as a highly potent (1.2 nM) and selective USP7 inhibitor which was found to be highly effective in increasing p53 levels and had significantly improved pharmacokinetic properties

owing to its simplified structure. Crystal structure revealed that the compound retained critical contacts in the USP7 active site cleft despite its simpler structure (*51*).

1.6.2.4. USP25/USP28 inhibitors

USP25 and USP28 are involved in the stabilization of oncogenes (*52*). Therefore, targeting these DUBs has emerged as an alternative to targeting oncogenes that cannot be directly pharmaceutically addressed. USP25 and USP28 being highly homologous (*53*) provide the potential of the development of bi-specific DUB inhibitors.

An HTS campaign lead to the identification of a benzylaminoethyl class of lead compounds as USP25/28 bi-specific inhibitors. Among these compounds, AZ1 **(Fig. 5)** was found to be the most potent inhibitor (IC_{50} = 0.6 μM). AZ1 was characterized against a panel of all recombinant human DUBs (10 μM) and tested against caspases and cathepsins (30 μM), showing selectivity for USP28 and USP25. In cellular studies, AZ1 inhibited DUB active site probe binding to USP25/USP28 and induced c-Myc degradation in multiple cancer cell lines (*54*).

Further SAR was used to develop a thienopyridine carboxamide derivative compound FT206 **(Fig. 5)**, which was optimal in its drug metabolism and pharmacokinetics properties while retaining the high potency towards USP25/28 exhibited by the previously characterized benzylaminoethyl class of inhibitors. FT206 treatment significantly reduced c-myc and other oncogenic levels and regressed lung cell carcinoma in a murine model (*42*).

Recently, co-crystal structures of USP28 with AZ1 and FT206 were published, highlighting the structural basis of bi-specificity of these inhibitors towards USP25 and USP28 (*55*). The structures

show that the compounds bind at an allosteric pocket in between the thumb and palm subdomains towards the S1 site, a cleft that is common in USP25 and USP28.

1.6.2.5. USP1 inhibitors

The USP1/UAF1 complex is a key regulator of DNA damage response (DDR), specifically in the translesion synthesis (TLS) and Fanconi anaemia (FA) pathways (*56*). Inhibiting USP1/UAF1 disrupts DNA repair, making it an attractive target for cancer therapy, especially in tumours reliant on DDR mechanisms.

ML323 **(Fig. 5)** was developed as a nanomolar inhibitor of USP1–UAF1 with remarkable selectivity and no substantial cytotoxicity to the human cells tested. ML323 treatment was shown to inhibit USP1/UAF1 mediated TLS and FA pathways in cancer cells and interestingly enhanced chemosensitivity in cancer cells by reducing resistance to cisplatin (*57*).

A cryo-EM structure of USP1-UAF1 in complex with ML323 shows the inhibitor binding at an allosteric cryptic pocket, explaining the basis of high potency and selectivity of this compound towards USP1-UAF1 (*58*).

Interestingly, USP1 is one of only two DUBs (other being USP30) for which inhibitors have entered into clinical trial. KSQ-4279 was the first potent and selective USP1 inhibitor to enter into clinical trials. Dosing KSQ-4279 in combination with PARP inhibitors regressed BRCA tumours and overcame PARP inhibitor resistance in patients with BRCA mutations (*59*).

1.6.2.6. USP30 inhibitors

USP30 is the only DUB located on the mitochondria outer membrane, where it regulates mitochondrial morphology (*60*). When further studies established that conjugation of phosphorylated ubiquitin to mitochondrial outer membrane proteins was the driving force of mitophagy (*61, 62*), the role of USP30 in antagonizing this process garnered significant interest. Genetic experiments (*63*) demonstrated that inhibition of USP30 could rescue defects associated with impaired mitophagy, providing potential for a strong alternative for treating Parkinson's disease.

Mission Therapeutics developed a class of N-cyanopyrrolidine compounds as covalent, irreversible USP30 inhibitors exhibiting high potency and selectivity to USP30. Among these compounds, MTX115325 **(Fig. 5)** was profiled in Parkinson's disease mouse model. Treatment with MTX115325 significantly improved mitophagy index in neuronal cells and reversed Parkinson's disease-associated toxicity (*64*). Also, two related compounds have been advanced successfully to phase II clinical trials by Mission Therapeutics, addressing the role of USP30 in acute kidney injury (*65*), making USP30 one of only two DUBs having compounds in clinical trials.

Mitobridge developed an effective class of phenylalanine derivatives as reversible, non-covalent USP30 inhibitors, out of which, Compound 39 **(Fig. 5)** was found to be remarkably potent and specific to USP30 (*66*) (more details in **Section 1.7.4.**). With its remarkable characteristics, Compound 39 is a promising candidate for structure-based characterization which would illuminate the principles of potent and specific inhibition of USP30.

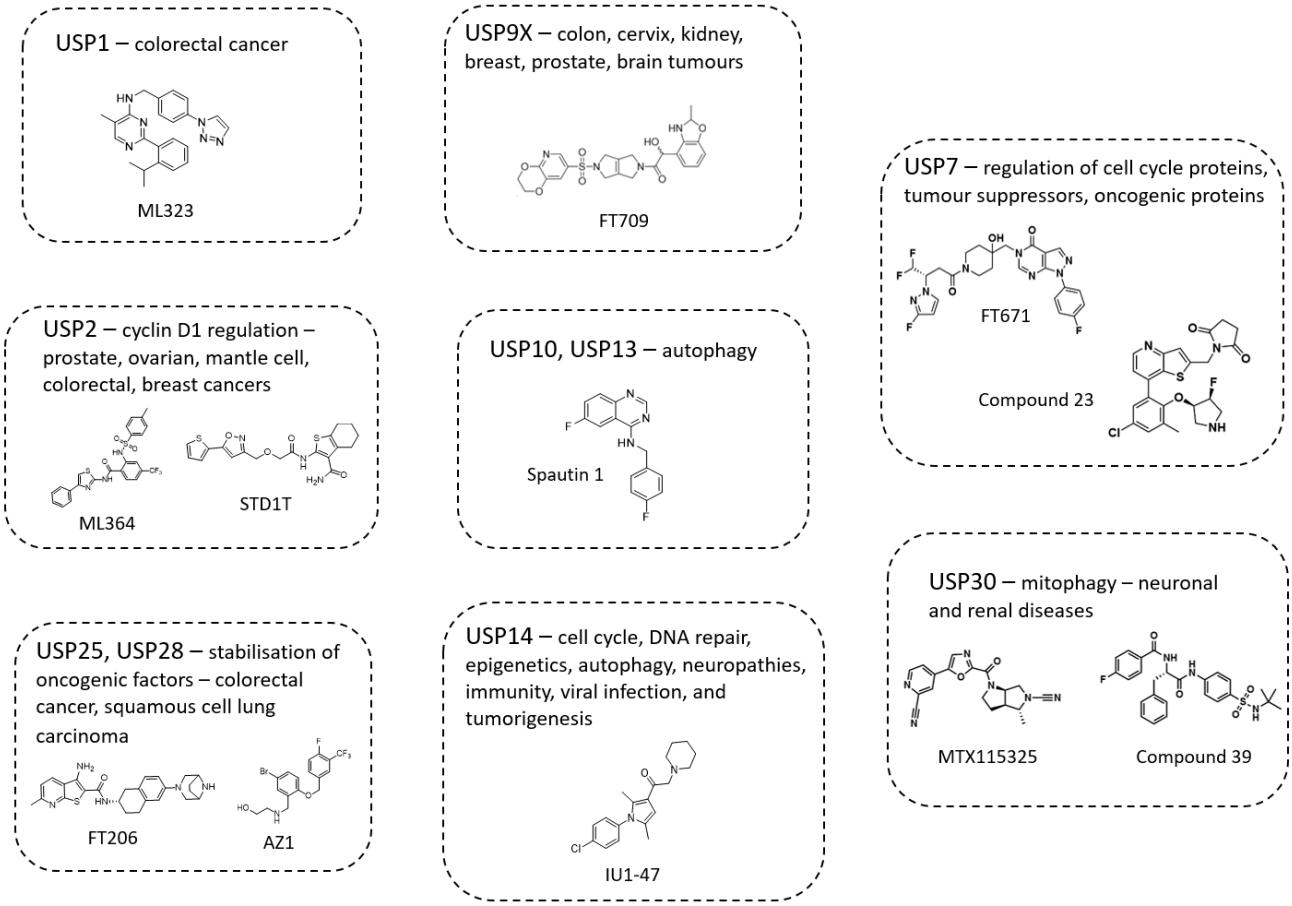

Figure 5 | USP DUBs as drug targets

Illustrations highlighting the involvement of USP DUBs in diseases and some notable small molecule inhibitors developed to target these USP DUBs – ML323 (*57*), FT709 (*67*), ML364 (*47*), STD1T (*48*), Spautin 1 (*68*), FT671 (*50*), Compound 23 (*51*), FT206 (*42*), AZ1 (*54*), IU1-47 (*44*), MTX115325 (*64*), Compound 39 (*66*)

1.6.3. Challenges in DUB inhibitor discovery

Though various USP DUB inhibitor scaffolds have been developed and characterized, very few USP DUBs have been targeted pharmacologically and even fewer have been structurally characterized **(Table 1)**. Obtaining specific USP DUB inhibitors has always been a challenge because the USP family members have subtle differences in their overall structures, with the major USP fold remaining conserved across all the members. Inhibitor specificity can be improved by structure-guided drug design, however, limited crystallizability of most USP DUBs is a major hindrance towards a structure-guided approach. The structures of the few USP DUBs solved required protein engineering efforts **(Table 1)**, indicating that USP DUB-inhibitor co-crystallization is not straightforward, and advanced protein engineering methods would be needed to streamline and accelerate structure-guided DUB drug discovery.

Moreover, high throughput screening of USP DUB inhibitors has also been challenging because of the vast expanse of the USP family with over 50 members. Additionally, most biochemical assays are focused on just the catalytic USP domain, thus hindering accurate and complete coverage of all USP DUB members. Combinatorial approaches are being developed to accelerate USP DUB inhibitor screening processes, for example, using existing USP DUB structures to create a library of compounds diversified to target other regions around the catalytic USP domain and coupling this focused library with activity-based protein profiling (ABPP) – MS/MS approach has been effective in developing inhibitors rapidly, targeting the USP family and other DUB family members (*69*).

Table 1. Crystal structures of human USP family DUB catalytic domains.

USP	Zn^{2+} coordination at tip of fingers subdomain	PDB accession codes of			Comments
		apo structures	Ub-bound structures	Inhibitor-bound structures	
USP1	yes	7AYO*	7 AY2*	7ZH4[#] (by Cryo-EM)	*in complex with UAF1 [#]with Ub-conjugated to FANCD2
USP2	yes		2HD5, 2IBI, 3NHE, 5XU8*, 5XVE, (+ with Ub variants)		*in complex with Ub and 6-thioguanine
USP4	yes	2Y6E*			*insertions removed by limited proteolysis
USP5	**no**		3IHP*		*full-length
USP7	**no**	1NB8, 2F1Z, 4M5W, 4M5X, 5FWI, 5J7T	1NBF, 5JTJ, 5JTV	5N9R, 5N9T, 5NGE, 5NGF, 5UQV, 5UQX, 5VS6, 5VSB, 5VSK, 5WHC, 6F5H	
USP8	yes	2GFO	3N3K*		*with ubiquitin variant
USP9X	yes	5WCH*			*with surface entropy reducing mutations
USP11	yes		8OYP*		*with Ub-GGG, insertion replaced by RDFrzS tag
USP12	yes	5K1A*, 5K1B*, 5K1C*[#], 5K16	5L8W*		*in complex with UAF1 [#]in complex with WDR20
USP14	**no**	2AYN	2AYO, 5GJQ*	6IIN, 6IIM, 6IIL, 6IIK	*Cryo-EM structure of 26S proteasome
USP15	yes	6GHA	6ML1*, 6CPM*, 6CRN*	6GH9	*with ubiquitin variant
USP21	yes		2Y5B, 3I3T, 3MTN*		*with ubiquitin variant
USP25	**no**	5O71, 6H4J, 6HEL			
USP28	**no**	6H4I, 6HEH*, 6HEJ, 8P19*	6H4H, 6HEI*, 6HEK	8HJE*, 7TUO*, 8P14*, 8P1P*, 8P1Q*	*insertions removed
USP30	yes		5OHK[#], 5OHN[#], 9F6G*	9F19*, 8D0A[+], 8D1T[+]	[#]insertions removed and with mutations *chimeric construct [+] with Fab
USP34	yes	7W3R	7W3U		
USP35	yes		5TXK*		*insertions removed
USP36	yes		8BS9, (8BS3*)		*with Fubi-PA
USP46	yes	6JLQ*[#]	5CVO*, 5CVN*, 5CVM, 5L8H		*in complex with UAF1 [#]in complex with WDR20
CYLD	**no**	2VHF			

1.6.4. Structural principles of USP DUB inhibition

From the few structures of USP DUB-inhibitor complexes so far, certain structural principles of specific DUB inhibition can be derived. Based on the mode of binding, DUB inhibitors can be broadly classified into active site inhibitors and allosteric inhibitors.

Active site DUB inhibitors bind within the catalytic cleft and can trap the catalytic triad either in an active (Type I) or inactive (Type II) conformation **(Fig. 6)**, thus directly blocking the DUB catalytic activity. Active site DUB inhibitors are mostly covalent in nature, but some of them can be non-covalent. The covalent active site inhibitors have warhead groups that can attack the catalytic Cys directly. For example, the USP7 active site inhibitor FT827 (*50*) has a vinyl-sulfonamide moiety that can form covalent linkage with the USP7 catalytic Cys **(Fig. 28c)**.

Allosteric inhibitors bind at a site other than the active site, inducing conformational changes in the catalytic triad, thus indirectly blocking the DUB catalytic activity. Based on the binding pocket, allosteric inhibitors can further be classified as ubiquitin competitive or non-ubiquitin competitive. The ubiquitin competitive allosteric inhibitors bind at or near the S1-distal (Type III-D) or S1'-proximal (Type III-P) ubiquitin binding sites **(Fig. 6)**, thus competitively blocking ubiquitin binding to DUB. For example, the USP7 inhibitor FT671 **(Fig. 5)** sits on a pocket that is at the interface of the palm and thumb subdomains, and extends towards the S1 ubiquitin binding site in the fingers subdomain **(Fig. 28c)**, thus blocking ubiquitin-mediated activation of USP7 (*50*). Non-ubiquitin competitive inhibitors (Type IV) bind at a pocket which is away from the ubiquitin binding sites and the catalytic site **(Fig. 6)**, and inhibit DUBs in a manner which is independent of ubiquitin binding mechanisms. For example, the USP1 inhibitor ML323 sits in a cryptic pocket in the thumb subdomain of USP1, inducing conformational changes that disrupt the hydrophobic core of USP1 (*58*).

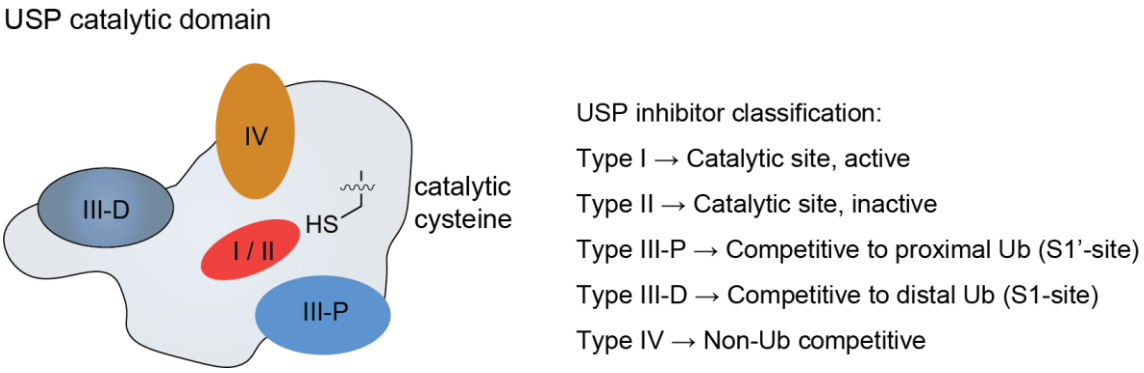

Figure 6 | Classification of USP DUB inhibitors
Illustration highlighting the different inhibitor binding sites within the USP catalytic domain (*70*).

DUB inhibitors can be elegantly designed to have a core scaffold that has chemical groups targeting unique features of DUBs, such as the plasticity of the blocking loops and the switching loop which show subtle variations across USPs. These inhibitors with a common scaffold can be further modified to have specificity handles, exhibiting differential binding mode. For example, the USP7 inhibitors FT671 and FT827 **(Fig. 5)** have the common 4-hydroxypiperidine moiety that forms interactions with the unique conformation of the USP7 switching loop in the inactive state. FT827 is further modified to have a vinyl-sulfonamide warhead causing it to branch towards the catalytic cysteine, whereas FT671 has fluoropyrazole group that forms interactions at the interface of thumb, palm and fingers subdomains, causing it to branch towards the S1 site in the fingers subdomain opposite to the catalytic site (*50*). Thus, DUB inhibitors with a common scaffold can branch towards different pockets based on differential specificity handles **(Fig. 28c)**, underlying the basis of specific DUB inhibition.

The structural analysis of USP7 inhibitors highlight that specific structural features of DUBs and subtle differences in structure across DUBs can be exploited to develop highly specific DUB inhibitors, which is why it is very important to structurally characterize USP DUBs. However, as

stated earlier, structural characterization of USP DUBs has always been challenging and this has hindered drug development. A prominent example is USP30, which is a key factor in Parkinson's disease (PD). Several inhibitors with diverse scaffolds have been developed to target USP30, one of the only two DUBs for which inhibitors have entered into clinical trials for PD and chronic kidney disease, underscoring its significance as a major drug target. However structural information about the specific mode of USP30 inhibition is missing, which hinders the development of inhibitors. Achieving the structure of USP30 in complex with inhibitors has been highly coveted, as a breakthrough in the structure would elucidate the principles of specific USP30 inhibition, and accelerate the development of effective therapeutics targeting PD.

1.7. USP30 – a promising drug target

1.7.1. Domain architecture, structure and regulation of USP30

USP30 is the only DUB that is constitutively located on the mitochondrial outer membrane. It has an N-terminal transmembrane domain (residues 1-56) consisting of a mitochondrial intermembrane portion (residues 1-35) and a transmembrane alpha helix (residues 36-56). The USP catalytic domain spans from residues 57-517 **(Fig. 7a)**. Immunofluorescence microscopy studies confirmed that the USP30 N-terminus is essential for its mitochondrial translocation and this is independent of its catalytic activity. While the N-terminus is lodged in the intermembrane, the C-terminus, including the entire catalytic domain, extends into the cytosol (*60*).

The catalytic triad consists of Cys77, His452 and a non-canonical Ser477 instead of Asp/Asn as in other USP DUBs **(Fig. 7a)**. The USP30 catalytic site has a unique hydrophobic patch composed of His445, His452 and Trp475 that accommodate Phe4 of ubiquitin, such that USP30 has strong preference for Lys6-linked ubiquitin chains (*71*).

The overall fold of the USP30 catalytic domain is similar to other DUBs, with modular architecture comprising of the finger, thumb and palm subdomains **(Fig. 7b)**. Notably, USP30 has two large insertions in between boxes 2 & 3 and boxes 4 & 5 **(Fig. 7c)**.

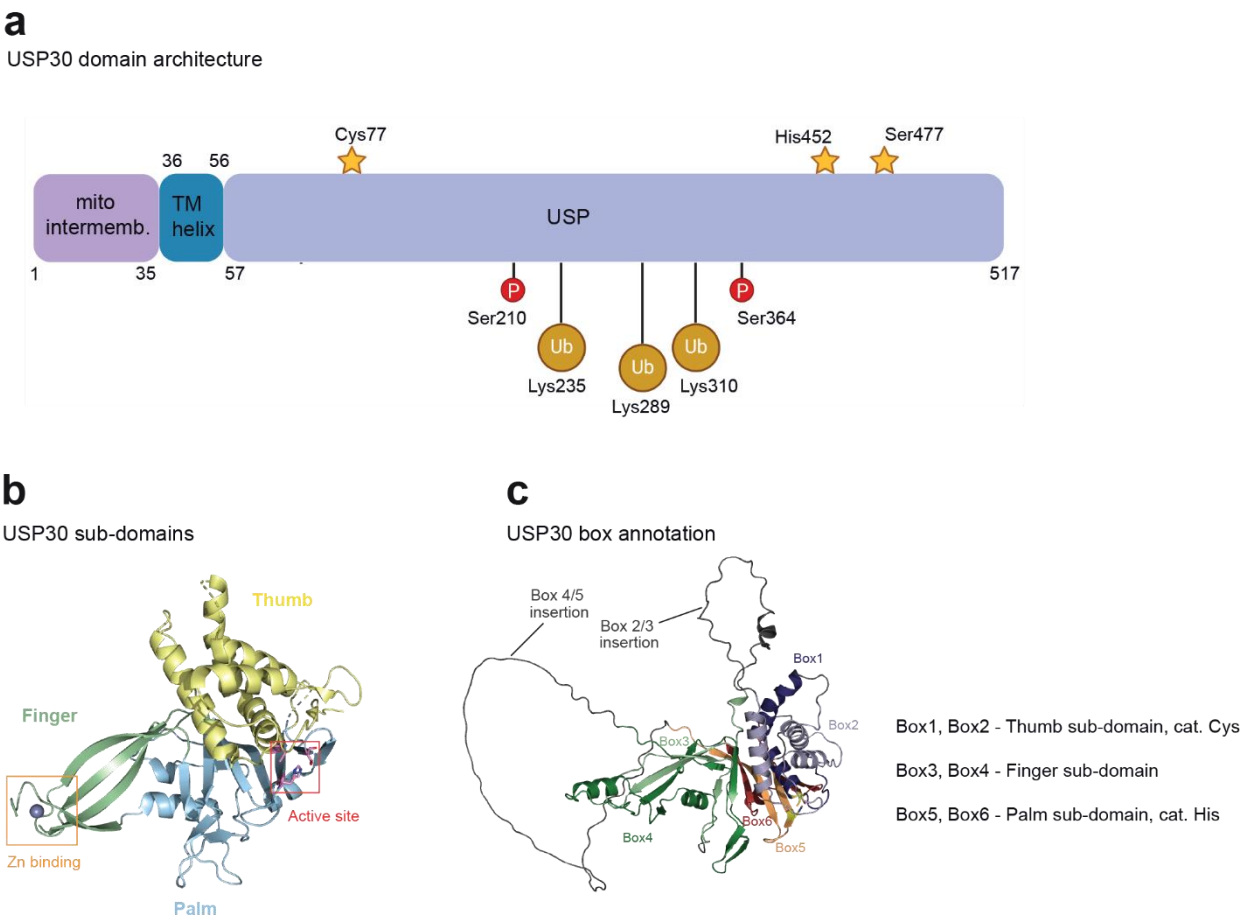

Figure 7 | USP30 domain architecture and structure

a, Illustration highlighting the different domains in human USP30. The yellow stars represent the catalytic residues, the red circles represent phosphorylation sites and the yellow circles represent ubiquitination sites. **b,** Cartoon representation of a previously engineered USP30 construct (PDB: 5OHK) highlighting the USP30 subdomains. **c,** AF2 model of full length human USP30 highlighting the box division of the catalytic domain and insertions in between the boxes.

USP30 is regulated by various post-translational modifications. With USP30 being the only DUB anchored onto mitochondrial outer membrane, its counter-play with the mitochondrial E3 ligase Parkin garnered significant interest. Parkin has been shown to ubiquitinate USP30 both in vitro and in vivo (*71*). These ubiquitination sites have been mapped to be present on the USP catalytic domain **(Fig. 7a)**. Furthermore, the key mitophagy signaling molecule PINK1 has been shown to indirectly regulate USP30 by phosphorylating the ubiquitin substrate (*72*). Upon mitochondrial

depolarization, PINK1 phosphorylates mitochondrial ubiquitin molecules to form Ser65-phosphorylated ubiquitin. Notably, USP30 has significantly lower activity towards Ser65-phosphorylated ubiquitin substrate (*71*). Therefore, Parkin and PINK1 tightly regulate the activity of USP30 in mitochondrial signaling pathways. Another notable pathway in which USP30 is involved is the IKKβ pathway, where the kinase IKKβ induces phosphorylation of USP30 at Ser210 and Ser364 **(Fig. 7a)**. This event in turn facilitates stabilization of USP30 which promotes tumour growth in hepatocellular carcinoma (*73*).

Therefore, regulation of USP30 by post-translational modifications is the hallmark feature of critical cellular pathways such as PINK1-Parkin mediated mitophagy, pexophagy, IKKβ-ACLY signaling and BAX/BAK-dependent apoptosis. Dysregulation of USP30 thus leads to neurodegenerative diseases, hepatocellular carcinoma, pulmonary disorders and peroxisome biogenesis disorders. USP30 being a major factor in these diseases is therefore a high potential drug target (*74*).

1.7.2. Role of USP30 in diseases

Broadly, USP30 is involved in two types of disorders: (i) Cancers, such as hepatocellular carcinoma and breast cancer, and (ii) autophagy-related disorders such as Parkinson's disease, chronic kidney disease, pulmonary disorders and peroxisome biogenesis disorders.

USP30 is a major factor in hepatocellular carcinoma (HCC), where it is part of the IKKβ-USP30-ACLY axis, regulating lipogenesis/tumorigenesis. This axis was studied in HCC mouse model, where USP30 is upregulated by IKKβ-induced phosphorylation. Upregulated USP30 in turn deubiquitinates and stabilizes the critical lipogenesis enzyme ATP citrate lyase (ACLY), causing

aberrant quality control in lipogenesis, in turn promoting tumorigenesis. USP30 knockout mice showed fewer tumour nodules and decreased tumour load, thus establishing USP30 as a major and possibly druggable factor in HCC (*73*).

The role of USP30 in Parkinson's disease is associated with mitophagy, where the interplay of USP30 with PINK1/Parkin is dysregulated, which affects mitochondrial quality control. Involvement of USP30 in mitophagy has been established experimentally by overexpression of USP30 that blocks PINK1/Parkin-driven mitophagy, while knockdown of USP30 was shown to significantly improve mitophagy (*60, 63*). The role of USP30 in pulmonary disorders is similar, where USP30-PINK1/Parkin regulation is disrupted, causing dysregulated mitophagy. Inhibition of USP30 has been shown to promote mitophagy in lung fibrosis models (*75*). USP30 is also involved in pexophagy, the process of peroxisomal quality control, where USP30 is regulated by PEX2-mediated ubiquitination. In peroxisomal biogenesis disorders, such as Zellweger syndrome, the USP30-PEX2 interplay is dysregulated, which leads to aberrant peroxisomal biogenesis and quality. Overexpression of USP30 has been shown to hinder pexophagy, and deletion of USP30, on the other hand, has been shown to induce pexophagy (*76, 77*).

The role of USP30 as a critical mitophagy regulator has drawn substantial interest towards studying its involvement in the pathology of mitophagy-related disorders, mainly neurodegenerative diseases. With several USP30 drug candidates characterized and two undergoing clinical trials, USP30 indeed is a highly relevant and promising therapeutic target.

1.7.3. USP30 is a major factor in mitophagy and consequently Parkinson's disease

1.7.3.1. Parkinson's disease

Parkinson's disease (PD) is a neurodegenerative disorder that is characterized by loss of dopaminergic neurons in substantia nigra, a critical portion of the midbrain that controls motor functions (*78*). A rare, hereditary form of PD termed autosomal recessive juvenile Parkinsonism (AR-JP) typically begins in individuals before the age of 40 and progresses with aging (*79*). Understanding the genetic causes of AR-JP can provide insights into disease etiology, reveal new pathways and provide potential for earlier diagnosis and better-targeted therapies. Biochemical and genetic studies reveal that mutations in genes encoding the PINK1 kinase and the E3 ligase Parkin are associated with AR-JP. Further investigation revealed PINK1 and Parkin working together in a selective autophagy mechanism for mitochondrial quality control called mitophagy, which was also one of the first biological processes found to be associated with PD, thus uncovering mitochondrial damage as a central factor in PD pathogenesis (*80*).

1.7.3.2. PINK1/Parkin pathway in mitophagy

In the process of mitophagy, PINK1 is stabilized and activated on mitochondrial outer membrane with reduced membrane potential during mitochondrial stress. Activated PINK1 phosphorylates ubiquitin conjugated to mitochondrial outer membrane proteins (MOMP) (*61*). This triggers recruitment of cytosolic Parkin to mitochondria, where Parkin is in turn phosphorylated and activated by PINK1. Activated Parkin then further builds ubiquitin chains on the MOMPs, and these ubiquitin molecules keep getting phosphorylated by PINK1, thus leading to a positive feedback loop causing hyper-ubiquitination of the damaged MOMPs which are recognized by autophagy receptors and marked for clearance via lysosomal degradation (*62*).

1.7.3.3. Role of USP30 in mitophagy

The ubiquitination of MOMPs provides a substrate for PINK1 to mediate mitophagy. Ubiquitination being a central process in mitophagy is in turn regulated by deubiquitination. Consequently, the mitochondrial deubiquitinase USP30 has emerged as a critical negative regulator of mitophagy because of its ability to deubiquitinate MOMPs, which was established by knockdown studies in HEK-293 cells in which knockdown of USP30 or overexpression of catalytically inactive USP30 significantly increased ubiquitination of certain MOMPs upon depolarization (*63*). The deubiquitinating activity of USP30 is directly antagonistic to Parkin as was established in the same study. Under depolarized conditions, Parkin overexpressing cells showed enhanced ubiquitination of certain MOMPs. Co-transfection with catalytically active USP30, but not catalytically inactive USP30, strongly decreased ubiquitination of the same MOMPs. USP30 being antagonistic to mitophagy was further shown in neurons (*60*, *81-83*) in which USP30 knockdown enhanced mitophagy index significantly by about 60%. Similar elevation of mitophagy was observed when these neurons were transfected with catalytically inactive USP30, while overexpression with catalytically active USP30 significantly reduced mitophagy index. Thus, it is well established that the catalytic DUB activity of USP30 directly antagonizes PINK1/Parkin-mediated ubiquitination and consequently mitophagy.

Notably, in addition to PINK1/Parkin-driven mitophagy, USP30 also negatively regulates basal mitophagy, when there is no mitochondrial stress. Under such basal conditions, USP30 works antagonistically to FBXO7, an E3 ligase complex subunit, to regulate ubiquitination of MOMPs (*84*). In accordance with this model, previous studies confirmed USP30 knockdown leading to increased basal mitophagy levels. In analogy to previous observations that USP30 is directly antagonistic to Parkin in stress-induced mitophagy, it would be interesting to see if in basal

mitophagy USP30 has an antagonistic component, such as PINK1 itself, since Parkin is not recruited to the mitochondria under basal conditions. To investigate this (*76*), Parkin-deficient cells were used, in which USP30 depletion led to increased basal mitophagy levels in line with previous observations. PINK1 depletion did not change basal mitophagy levels. However, PINK1 depletion suppressed the increase in basal mitophagy levels caused by USP30 knockdown. This suggests that basal mitophagy is PINK1-dependent/Parkin-independent, and USP30 works upstream to PINK1 in basal mitophagy. Ubiquitination of MOMPs by FBXO7 provides ubiquitinated substrate for PINK1, where PINK1 phosphorylates ubiquitin and activates enhanced mitophagy above basal levels, an event which should occur only under stress. USP30 ensures removal of the ubiquitin from the MOMPs, making these substrates unavailable for PINK1, thus maintaining basal level of mitophagy when there is no stress. Thus, the role of USP30 is critical in setting a threshold for mitophagy (*76*).

To summarize the model of PINK1-Parkin-USP30 in mitophagy **(Fig. 8)**, in basal conditions, USP30/FBOX7 work upstream to PINK1 and maintain the threshold for mitophagy. USP30 ensures that MOMPs are not degraded needlessly before stress, so that during actual stress condition, enough MOMP substrate is available for ubiquitination and subsequently available for phosphorylation by PINK1 to trigger PINK1/Parkin-dependent mitophagy. Under stress conditions, PINK1/Parkin get activated, that drive hyper-ubiquitination and hyper-phosphorylation on the MOMPs. Parkin in turn ubiquitinates USP30, marking it for degradation, so the role of USP30 in stress condition becomes downstream to PINK1. Also, USP30 has significantly weak activity towards phosphorylated ubiquitin (*71*)., which consolidates PINK1/Parkin-mediated ubiquitination of damaged MOMPs and ensures their efficient clearance by mitophagy.

USP30 also has other critical functions in mitochondrial import (*85*) and mitochondrial morphology. Depletion of USP30 knockdown led to elongated mitochondrial morphology, which was reversed by ectopic expression of catalytically active USP30. This was one of the first evidences of USP30 being involved in the regulation of mitochondrial morphology (*86*).

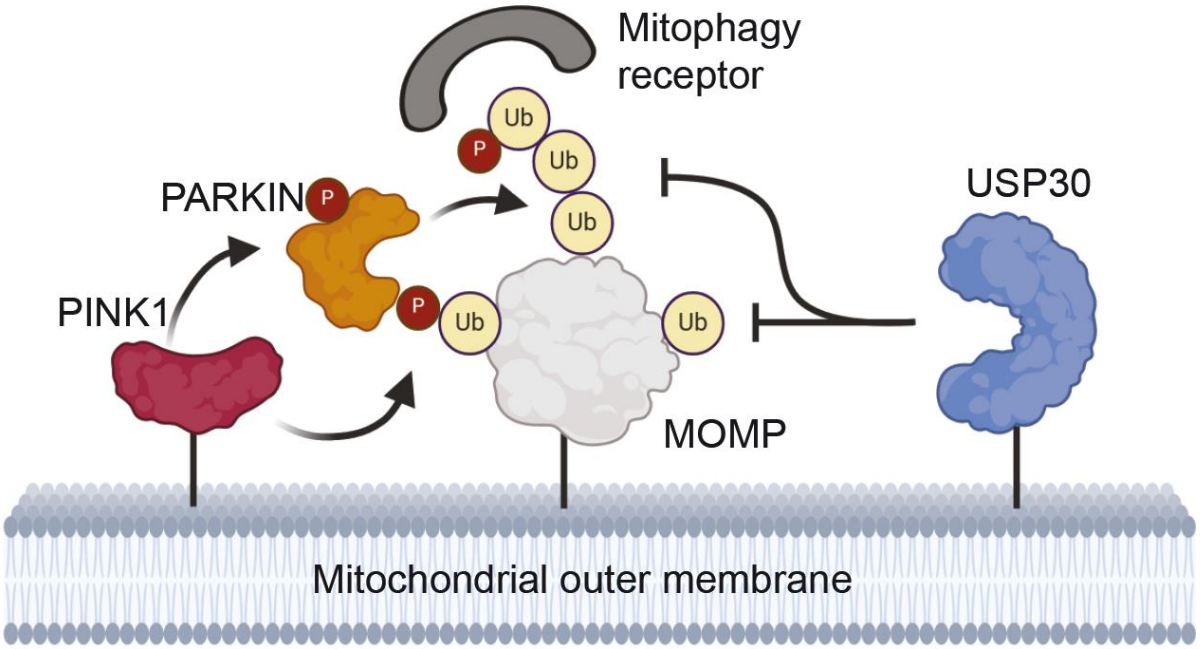

Figure 8 | USP30 domain architecture and structure
Illustration highlighting the antagonistic role of USP30 against PINK1/Parkin-mediated mitophagy.

1.7.3.4. Role of USP30 in the pathogenesis of Parkinson's disease

Comprehensive studies of the critical role of USP30 in mitophagy suggest that USP30 is a highly promising drug target for Parkinson's disease **(Fig. 9)**. Studies in neuronal cells, flies and mice have shown to improve mitophagy in PD conditions by knockdown or small molecule inhibition of USP30 (*64*, *84*, *87-90*). In neurons, USP30 knockdown rescued impaired mitophagy associated with Parkin pathogenic mutations. Similar observation was found in Drosophila PD models with pathogenic PINK1 or Parkin mutants, in which USP30 KD significantly improved mitophagy and restored mitochondrial morphology (*63*). In dopaminergic neurons derived from PD patients carrying loss of function Parkin mutations, USP30 inhibition by a small molecule compound significantly improved mitophagy (*89*). In PD mouse model, both knockdown and inhibition of USP30 by a small molecule compound led to significant improvement in mitophagy in dopaminergic neurons, protection of these neurons from α-synuclein associated toxicity and even revival of normal dopamine levels (*64*).

Alongside PD, inhibition of USP30 is also being explored as a therapeutic strategy in acute kidney injury (AKI) due to links to mitochondrial dysfunction (*65*). Mission therapeutics has advanced two USP30 compounds successfully to phase II clinical trials addressing the role of USP30 in AKI. With clear effects of USP30 inhibition towards improving mitophagy defects and with USP30 compounds in clinical trials, USP30 has emerged as a prime drug target, sparking the development of several scaffolds of small molecule inhibitors, covering covalent and non-covalent modes of inhibition **(Fig. 10)**.

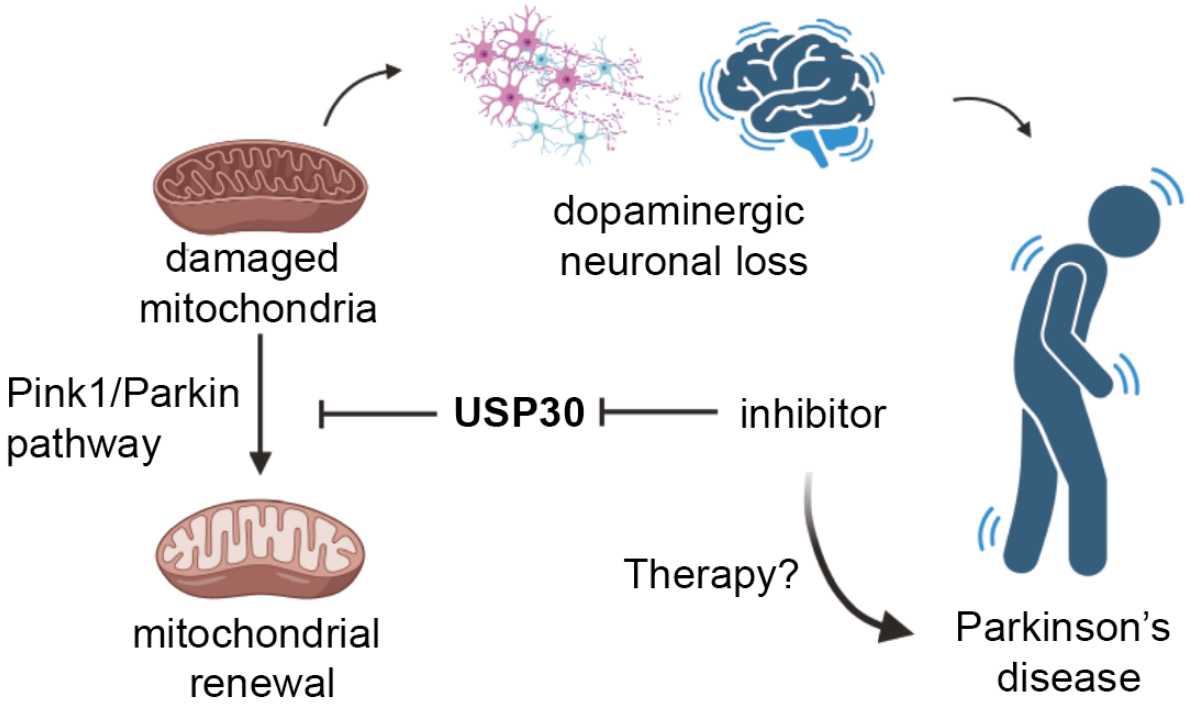

Figure 9 | USP30 in Parkinson's disease
Illustration highlighting the critical role of USP30 in Parkinson's disease pathology and the potential of inhibiting USP30 as a therapeutic strategy.

1.7.4. Development of USP30 inhibitors

One of the first characterized USP30 compound was a natural diterpenoid derivative. Treatment with this compound induced mitochondrial elongation and fusion in mitofusin 1 deficient cells (*86*). The effect of USP30 inhibition with small molecule compounds towards improved mitochondrial quality sparked the development of various USP30-specific compound scaffolds, covering covalent and non-covalent modes of inhibition **(Fig. 10)**, with two compounds developed by Mission therapeutics that have been advanced into clinical trials. An effective class of USP30 compounds that emerged from an SAR campaign (*66*) were a group of non-covalent phenylalanine derivatives. Attachment of naphthylsulfonamide to the phenylalanine core proved to be an

effective design to produce Compound 1, which was relatively specific to USP30, not inhibiting 3 other USPs at <10 µM compound concentration, and has an in vitro IC_{50} < 1 µM. SAR improvement of compound 1 by substitution with cyclohexyl, to produce the compound MF094 **(Fig. 10)**, dramatically increased the potency by 10 folds, with IC_{50} of 120 nM and moderate selectivity to USP30, exhibiting <30% inhibition for 22 USPs at <10 µM. Also, MF094 treatment accelerated mitophagy in mouse myoblast cells. Further SAR development of MF094, with introduction of benzenesulfonamide moiety and fluorophenyl group to the phenylalanine core led to the development of the benzenesulfonamide class, the most selective and potent class of USP30 inhibitors so far (*66*).

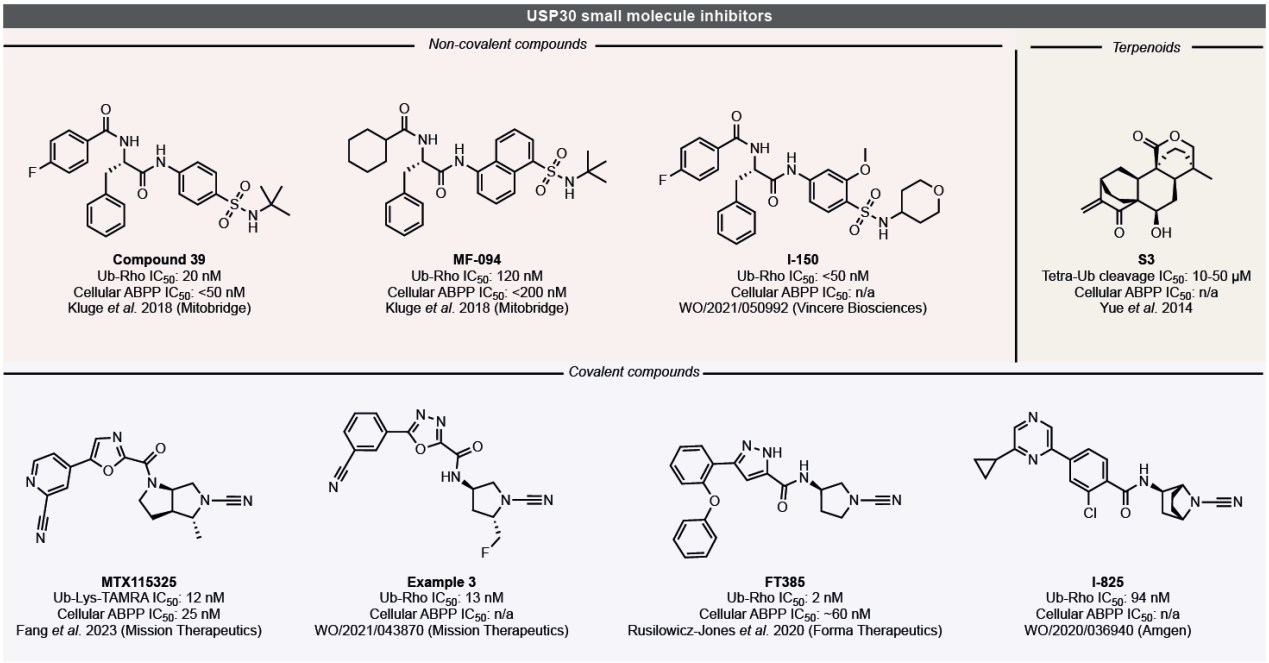

Figure 10 | Small molecule inhibitors of USP30

Chemical structures of representative examples of small molecule USP30 inhibitors are given together with characterization data and references. Cyanamides of covalent inhibitors form isothiourea linkages with the active site cysteine of USP30. Non-covalent inhibitors belong either to chemical series which were developed from phenylalanine derivatives (with either a benzenesulfonamide or a naphthylsulfonamide) or are natural product derivatives.

Compound 39 of the benzenesulfonamide class **(Fig. 11)** is a highly effective USP30 inhibitor, displaying IC_{50} values against recombinant USP30 of 2 to 20 nM and cellular target engagement in the 10-50 nM range **(Fig. 10)** (*66, 90, 91*). Moreover, the compound features pronounced specificity for USP30 both in cellular and in vitro assays, with no other DUB being inhibited at 100 µM in a panel of recombinant enzymes (*66, 89*) **(Fig. 11)**. Compound 39 has also been benchmarked in a range of cellular mitophagy assays (*89, 91, 92*). In dopaminergic neurons derived from PD patients, treatment with Compound 39 significantly improved mitophagy index, underscoring the therapeutic potentials of such a compound specifically targeting USP30 (*89*). Interestingly, Compound 39 was shown to exhibit a slow and tight binding kinetics, and thus its mode of binding has been proposed as "pseudo-covalent", despite it being a non-covalent compound (*91*). Compound 39 binding within the USP30 catalytic domain has been predicted by molecular docking and hydrogen-deuterium exchange mass spectrometry (HDX-MS) (*91*).

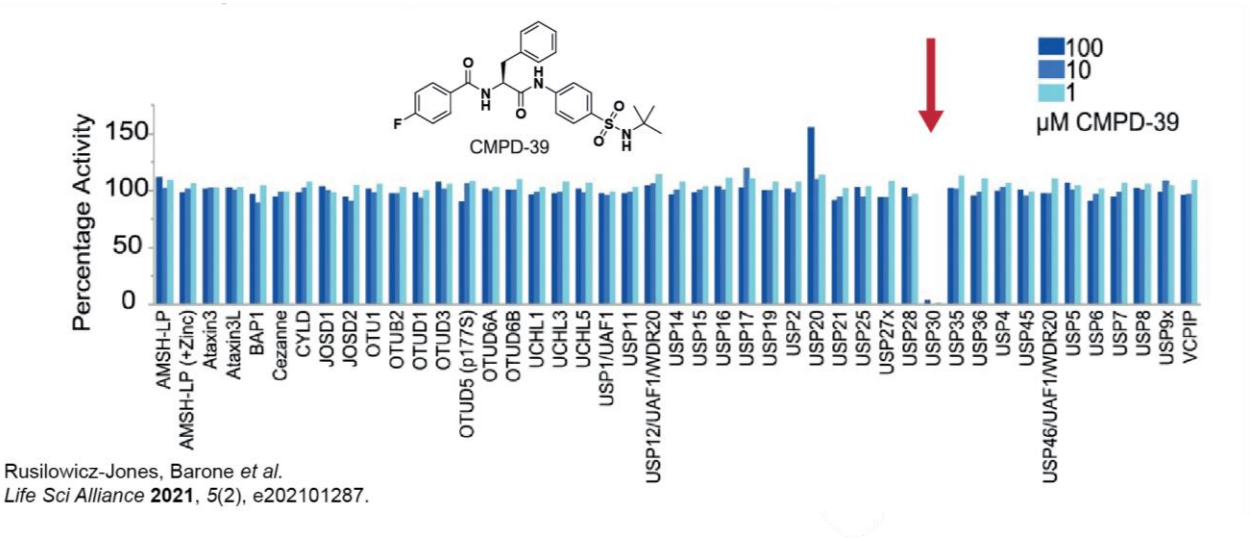

Figure 11 | Selectivity of Compound 39

Inhibitor potency assay data for a panel of recombinant human DUBs. The data represents loss in enzyme activity in the presence of 3 different concentrations of Compound 39.

However, the molecular basis of such remarkably high specificity and potency, and the unusual "pseudo-covalent" binding mode is currently unknown, which has been hindering structure-based development of USP30 inhibitors. This is likely related to the high flexibility and comparably poor crystallizability of the human USP30 protein. Multiple rounds of USP30 construct optimization were required for structural characterization in ubiquitin-bound states (*71*), so advanced protein engineering methods could likely facilitate structural characterization of USP30 inhibition.

2. Chimeric deubiquitinase engineering reveals structural basis for specific inhibition of USP30

2.1. Rationale

Limited crystallizability of USP30 has been a major hindrance in structure-based drug development. This is likely because of large disordered loops and flexible subdomains in USP30. Two large insertions in between boxes 2 & 3 and boxes 4 & 5 were found to be highly flexible by HDX-MS. These insertions were deleted to create USP30^{c1}, which was crystallizable with ubiquitin probe (*71*) **(Fig. 12a)**. However, screening of USP30^{c1} in complex with small molecule compounds did not yield any crystals.

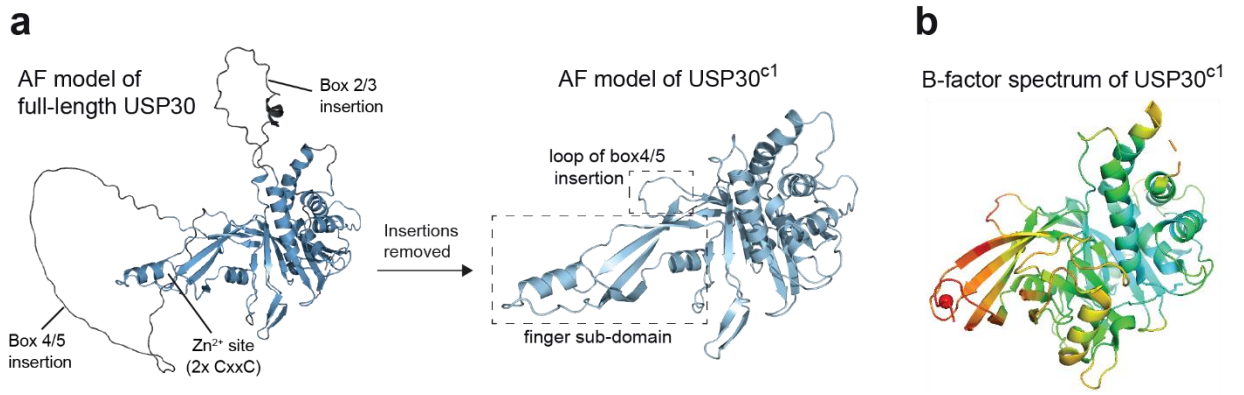

Figure 12 | Initial engineering of USP30
a, AF2 models highlighting the engineering strategy to create USP30^{c1} (*71*) (PDB: 5OHK). Dotted boxes show the potential regions for further engineering. **b,** B factor spectrum derived from PyMOL. Red, orange, yellow coloured regions represent regions of high flexibility, and blue, green regions represent regions of low flexibility. Flexibility from high to low is in the order: Red>Orange>Yellow>Green>Blue.

The hypothesis presented in this dissertation for the limited crystallizability of USP30^{c1}, is that despite engineering of USP30, high flexibility still remains in the fingers subdomain, which consists of 4 large β-sheets coordinated at the tip by zinc. This is supported by previous HDX-MS analysis (*71, 91*) and B-factor spectrum of USP30^{c1}, showing high flexibility in the fingers subdomain, especially the zinc coordination site at the finger tip **(Fig. 12b)**. Drawing this hypothesis was further guided by a systematic review of all crystal structures of human USP DUBs deposited in the protein data bank (PDB) **(Table 1)**. Out of the 55 human USP DUBs, apo or inhibitor-bound structures are available only for 14 (25%) of them, highlighting the limited crystallizability of USP DUBs in general. Notably, only 8 (15%) of the 55 human USP DUBs do not coordinate zinc at the tip of their fingers subdomain, while the majority 47 USP DUBs (85%) do coordinate zinc at the finger tip. Overall, zinc coordinating USP DUBs are over-represented. However, a majority 6 out of the 8 (75%) non-zinc coordinating USP DUBs have apo or inhibitor-bound structures, while only 8 out of the 47 zinc coordinating USP DUBs (17%) have apo or inhibitor-bound structures **(Fig. 14b)**. So, among the structurally characterized human USP DUBs, the ones which do not coordinate zinc at the finger subdomain tip are over-represented, suggesting that zinc free USP DUBs have higher propensity for crystallization.

The solution proposed in this dissertation is that systematic replacement of USP30 fingers subdomain with equivalent regions from other zinc free, well-crystallizable DUBs, to create chimeric constructs of the USP30 catalytic domain, may facilitate crystallization. The idea of such a chimeric engineering approach was further motivated by (i) previous engineering strategies that were applied to obtain most of the human USP DUB structures so far **(Table 1)** (ii) previous HDX-MS and molecular docking prediction of Compound 39 binding in the palm and thumb subdomains, which are spatially separated from the chimeric engineering site focused at the finger

subdomain (*91*). For the USP30 chimeric engineering design in this dissertation, the finger subdomains of USP7 and USP14 were chosen as prime candidates, as they lack zinc ions and both of these DUBs have been crystallized in multiple apo and inhibitor-bound forms **(Table 1)** (*38, 39, 45, 50, 93-95*). The USP DUB CYLD, which features truncated zinc-free fingers, was also included.

The aim of this project was to obtain the crystal structure of at least one chimeric USP30 construct in complex with a potent and selective small molecule compound, preferably Compound 39. Broadly, the aim of the dissertation work was to unravel the molecular basis of potency and specificity of USP30 targeting compounds, thus significantly contributing to the rapid structure-based therapeutics development towards neurodegenerative diseases. Figure 13 highlights the workflow employed for this project.

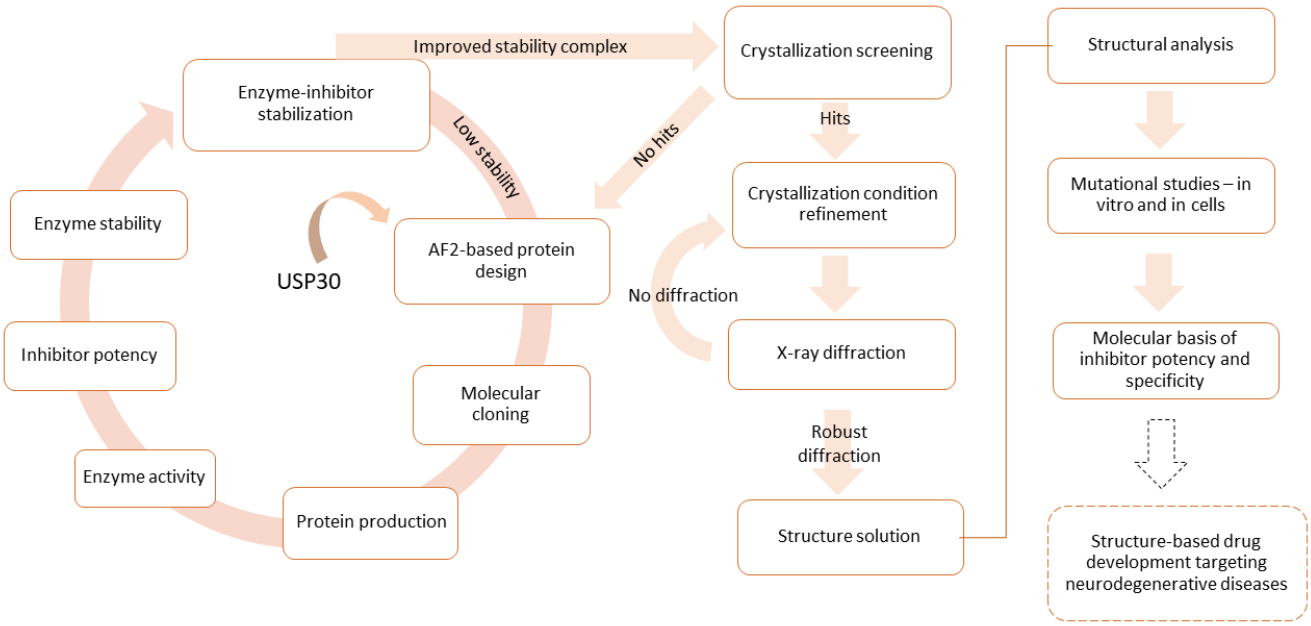

Figure 13 | Workflow of the project
Schematic representation of protein design, cloning, protein production, biochemical and biophysical assays and X-ray crystallography workflow employed for the project.

2.2. Design and characterization of chimeric USP30 constructs

With the aim of improving USP30 crystallizability, the previously engineered construct USP30^{c1} was chosen as the template for applying chimeric engineering **(Fig. 14c)**. Based on previous crystal structure analysis, suitable USP DUBs for chimeric engineering of USP30 were chosen in three phases. In the first phase of chimeric engineering, the finger subdomain of USP7 was chosen as the engineering element, which has the most inhibitor-bound structures so far among all human USP DUBs, and has a zinc free fingers subdomain **(Fig. 14d)**. The USP DUB CYLD, which has highly truncated zinc free fingers subdomain **(Fig. 14g)**, was also included in this phase. In the second phase of engineering, the chimeric design was further modified by including USP14 fingers subdomain **(Fig. 14e)**, as USP14 also has multiple crystal structures in apo and inhibitor-bound forms and zinc free finger subdomains, and interestingly one of the β-sheets of the USP14 fingers sub-domain is highly truncated **(Appendix 3.3)**. A non-chimeric USP30 construct (c2), in which the entire fingers subdomain is deleted and replaced by Gly-Ser linkers **(Fig. 14h)**, was also included in this phase. In the third phase of engineering, it was noticed that the remnant loop of box 4/5 deletion in USP30^{c1} is highly flexible as shown by B-factor spectrum **(Fig. 12b)** and previous HDX-MS analysis. The plan in this phase was to replace this loop by an equivalent region from USP35, which is the only DUB having a structured β hairpin in this equivalent region **(Fig. 14f)**.

In an iterative process, 15 chimeric constructs were explored, starting with boundary design by structure superposition, design validation by AlphaFold2-based modeling **(Fig.14i-l)**, cloning **(Fig. 14m)**, protein purification, and biophysical characterization **(Fig. 15a-e)**. This process is illustrated with four diverse chimeras: Chimera 1 (USP30^{ch1}) features the fingers of USP7, chimera 2 (USP30^{ch2}) features the fingers of USP14, chimera 3 (USP30^{ch3}) features the fingers of USP14

and the box 4/5 insertion of USP35, and chimera 4 (USP30^{ch4}) features the fingers of CYLD **(Fig. 14i-l)**. See Appendix 3.1 and 3.2 for an overview of all chimeric proteins designed and tested.

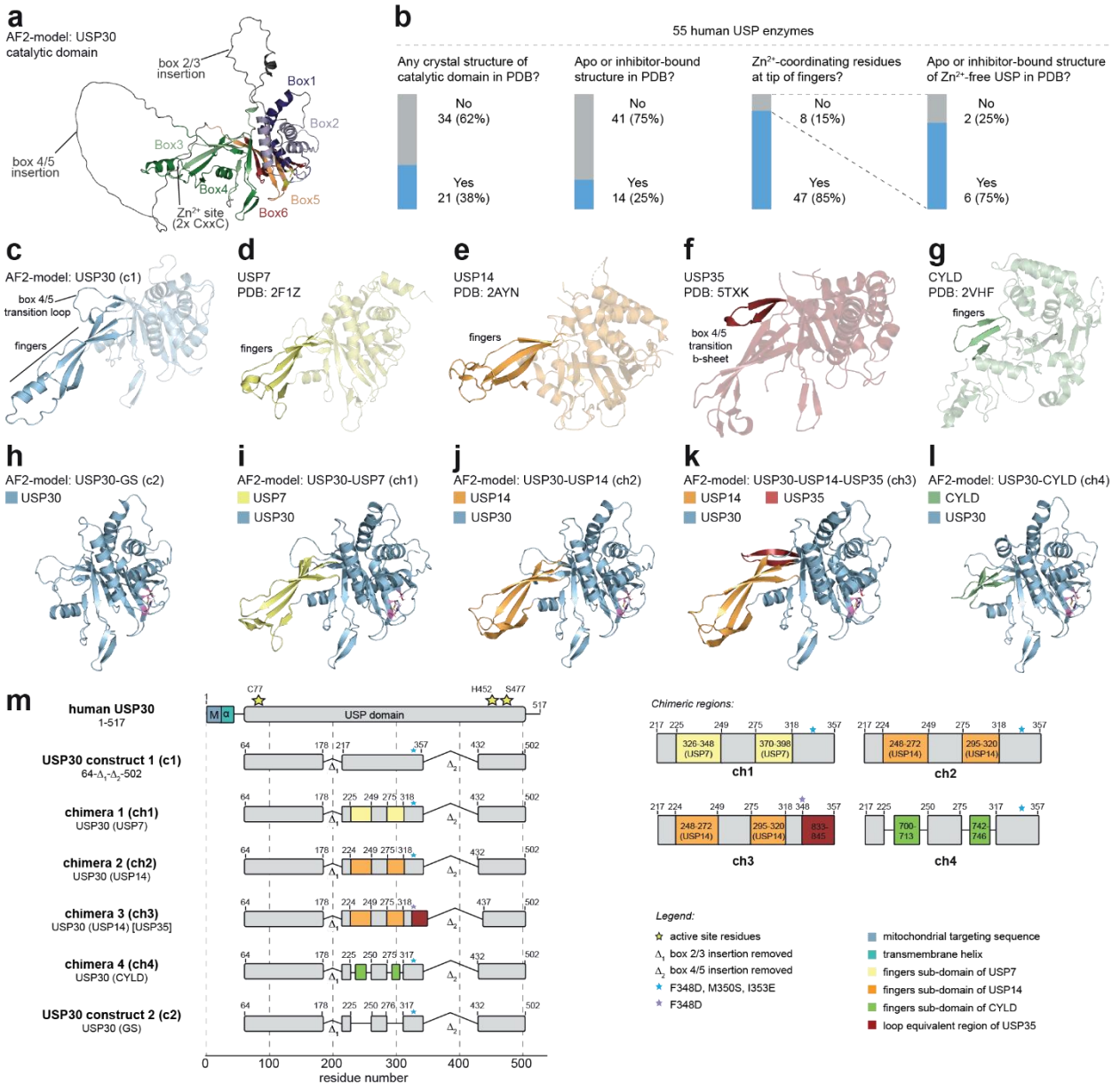

Figure 14 | Design of chimeric USP30 protein constructs

a, AlphaFold2 (AF2)-model of the catalytic domain of human USP30. USP boxes and domain insertions are indicated. **b,** Statistics of human USP enzymes regarding their characterization by crystallography and regarding the presence of Zn^{2+}-coordinating residues in the tip of the fingers subdomain. **c,** AF-model of USP30c1, previously optimized for structural studies and used as a starting point for this project. **d-g**,

Experimental structures of catalytic domains of USP7 (d), USP14 (e), USP35 (f), and CYLD (g). Elements used for USP30 chimeric engineering are highlighted. **h-l,** AF-models of USP30 constructs explored in this study. Catalytic residues are shown in pink. m, Architecture of USP30 constructs with close-up view of the boundaries of the chimeric portions.

All proteins were expressed, purified, and their stability was assessed by thermal shift assay (TSA). Incorporation of USP7 fingers subdomain decreased the stability of USP30, while inclusion of USP14 and CYLD fingers subdomain did not alter protein stability. Interestingly, the stability of the USP14 fingers subdomain containing construct was boosted significantly by the addition of the structured box 4/5 region from USP35 **(Fig. 15a)**. Chimeras 1-3, showed complete reactivity to ubiquitin probe Ub-PA, whereas the reactivity was significantly reduced for the fingers subdomain truncated constructs **(Fig. 15b)**. Probe reactivity results correlated with protein stabilization assay **(Fig. 15c)**. Consistently, chimeras 1-3 showed high catalytic activity towards the fluorogenic substrate Ubiquitin-RhoG (Ub-RhoG), whereas $USP30^{ch4}$ and $USP30^{c2}$ were virtually inactive **(Fig. 15d-e)**. This is in line with the fact that the fingers subdomain is the major ubiquitin binding site, and the observations from these assays indicate smooth replacement of the USP30 fingers subdomain in chimeras 1-3. Importantly, chimeras 1-3 retained their propensity to be inhibited by Compound 39 with IC_{50} values between 0.3 and 0.7 nM compared to 0.8 nM of construct 1 **(Fig. 15f-g)**. To assess inhibitor binding in all proteins, including the catalytically inactive chimeras, inhibitor-induced changes in protein stability were measured. The presence of Compound 39 increased protein stabilities between 7 and 9°C for all samples, which demonstrates that all USP30 constructs retain affinity for the benzenesulfonamide scaffold **(Fig. 15h)**.

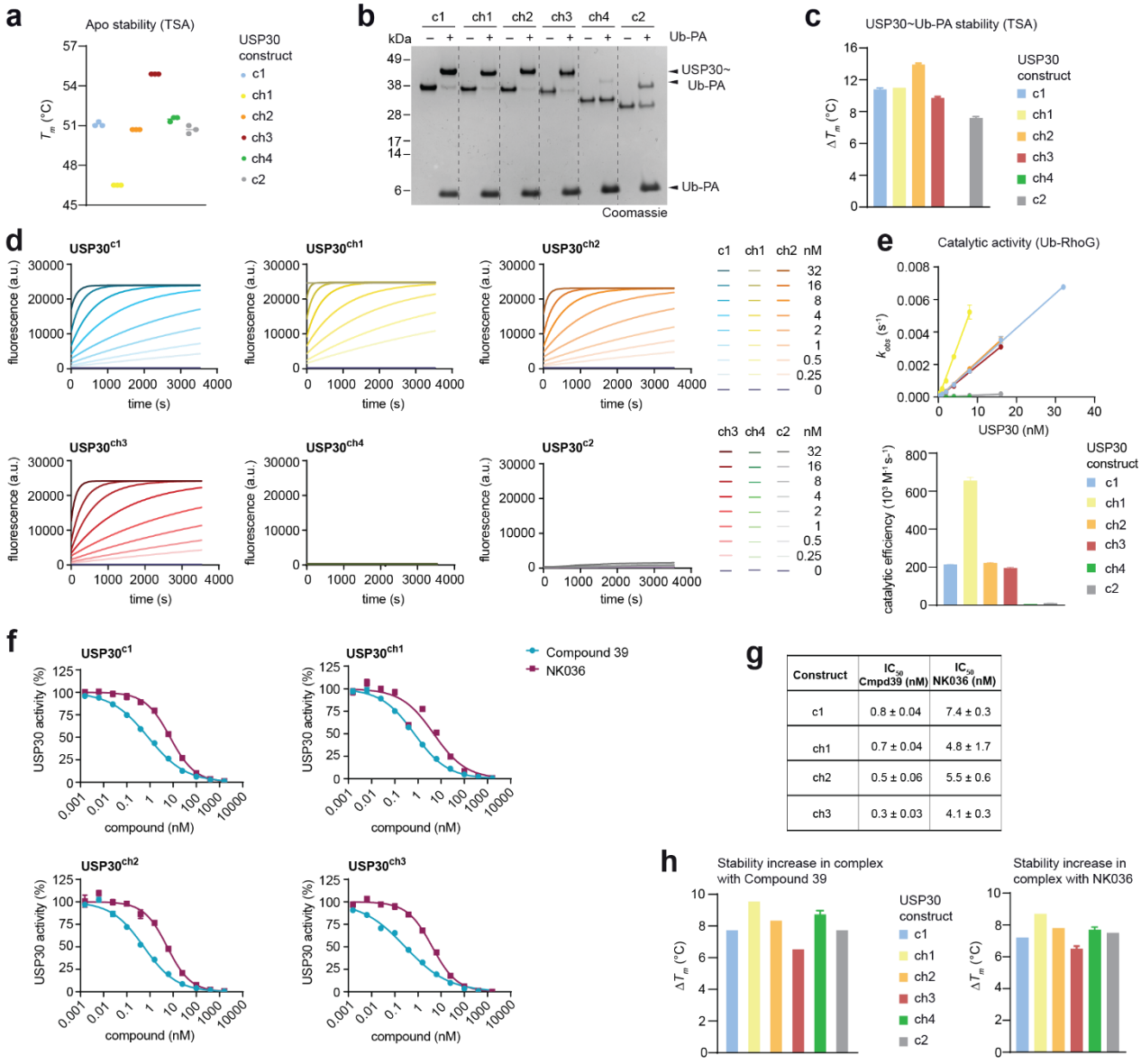

Construct	IC_{50} Cmpd39 (nM)	IC_{50} NK036 (nM)
c1	0.8 ± 0.04	7.4 ± 0.3
ch1	0.7 ± 0.04	4.8 ± 1.7
ch2	0.5 ± 0.06	5.5 ± 0.6
ch3	0.3 ± 0.03	4.1 ± 0.3

Figure 15 | Biochemical characterization of USP30 chimeras

a, Protein stability assessment of USP30 constructs with thermal shift assays. **b,** Ubiquitin probe reactivity assay. Samples were analyzed by SDS-PAGE and Coomassie staining. **c,** Changes in protein stability upon binding to Ub-PA. ΔT_m was calculated as T_m (Ub-PA-bound) subtracted from T_m (apo protein). Mean ± s.d. (N=3). **d,** Quantification of enzyme activity. Varying concentrations of USP30 proteins were incubated with Ubiquitin-RhoG substrate and fluorescence was recorded. **e,** Observed rate constants derived from plots in d were plotted over enzyme concentrations (upper panel) to derive catalytic efficiencies (lower panel). Mean ± s.e.m. **f,** Inhibitory potencies of Compound 39 and NK036. Compounds were pre-incubated with USP30 constructs for 1.5 h, and remaining activities were determined from Ub-RhoG cleavage assays. **g,** IC50 values of assays shown in f. **h,** Assessment of binding of Compound 39 and NK036 to indicated USP30 constructs by thermal shift assays. ΔT_m was calculated as T_m of the inhibitor-bound sample subtracted from the T_m of the apo protein.

Table 2. Biochemical and biophysical characterization of USP30 constructs.

Construct	Catalytic efficiency ($x10^3$ $M^{-1}s^{-1}$)	Apo USP30 stability (avg. T_m in °C)	Compound potency (IC_{50} in nM) inhibitory		Change in stability upon Inhibitor binding (avg. ΔT_m in °C)		USP30 stability in presence of compound (avg. T_m in °C)	
			Cmpd39	NK036	Cmpd39	NK036	Cmpd39	NK036
c1	213.9 ± 2.4	51.1	0.8 ± 0.04	7.4 ± 0.3	7.8	7.2	58.9	58.3
ch1	655.9 ± 17.6	46.5	0.7 ± 0.04	4.8 ± 1.7	9.6	8.7	56.1	55.2
ch2	221.8 ± 3.6	50.7	0.5 ± 0.06	5.5 ± 0.6	8.4	7.8	59.1	58.5
ch3	195.5 ± 2.4	54.9	0.3 ± 0.03	4.1 ± 0.3	6.6	6.5	61.5	61.4
ch4	5.8 ± 0.0	51.5	-	-	8.8	7.7	60.3	59.2
c2	11.3 ± 0.3	50.7	-	-	7.8	7.5	58.5	58.2
ch3 F453Y	62.7 ± 0.7	56.4	531 ± 99	632 ± 119	2.1	1.8	58.5	58.2
ch3 L328F	14.2 ± 0.2	57.0	-	-	1.5	1.2	58.5	58.2
ch3 I154A	-	55.2	79 ± 11	76 ± 8	3.8	3.8	59.0	59.0
ch3 F157A	-	54.9	51 ± 8	97 ± 8	3.9	3.6	58.8	58.5
ch3 A162S	-	55.8	63 ± 9	70 ± 5	4.2	3.9	60.0	59.7

2.3. Design validation and inhibition of a chimeric USP30-(USP14-USP35) construct

Summary of construct characterization data **(Table 2)** favoured $USP30^{ch3}$ as the construct of choice for further analysis, especially considering its highest stability among all the USP30 constructs, which is an important factor for crystallization studies. $USP30^{ch3}$ was designed by incorporating structural components of USP14 and USP35 into USP30 **(Fig. 16a-b)**. The USP30 finger sub-domain (residues 225-248 and 276-317) was replaced with USP14 finger sub-domain (residues 247-271 and 294-319) in which one of the beta sheets is truncated as compared to USP7 finger sub-domain **(Appendix 3.3)**, thus making for a better design of ch3 in terms of finger subdomain compactness as compared to ch1 which has the USP30 finger sub-domain replaced by that of

USP7. In addition to the finger sub-domain engineering, a USP30 flexible loop (residues 349-357) was replaced with a structured equivalent region from USP35 (residues 833-845).

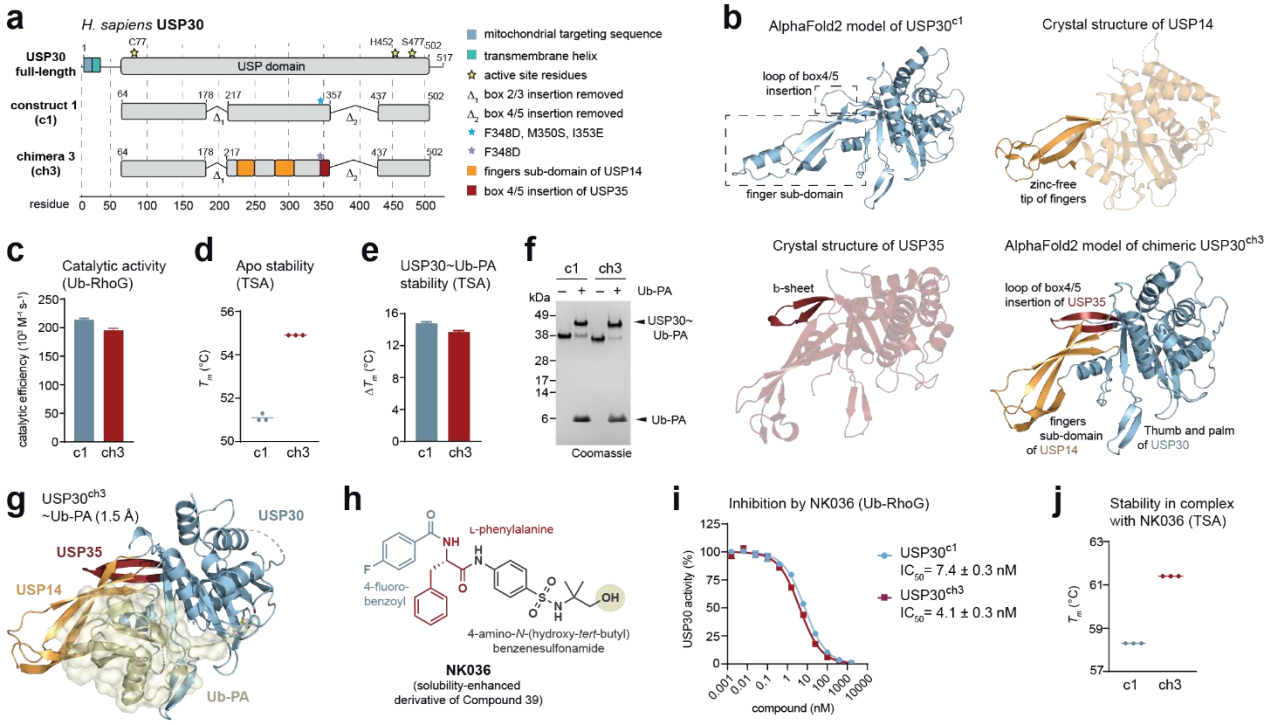

Figure 16 | Design, characterization and inhibition of chimeric USP30

a, Architecture of full-length human USP30, previously used construct c1 (named c13 in 37) and here described USP30 chimera ch3. See Extended Data Fig. 2 for other chimeras. **b**, AlphaFold2-predicted model of USP30c1, crystal structures of the catalytic domains of USP14 (PDB: 2AYN) and USP35 (PDB: 5TXK), and AlphaFold2-predicted model of USP30 chimera ch3. Regions used for grafting are shown in corresponding colors. **c,** Catalytic efficiencies of indicated USP30 constructs, determined from Ubiquitin-RhoG (Ub-RhoG) cleavage assays. See Extended Data Fig. 3 for raw data. Mean ± s.e.m. **d,** Stability assessment of USP30 constructs in their apo states derived from thermal shift assays. T_m, protein melting temperature. **e,** Changes in protein stability upon binding to the Ubiquitin probe Ub-PA. Mean ± s.d. (N=3). **f,** Gel-based Ub-PA binding assay. **g,** Crystal structure of USP30ch3~Ub-PA. See Table 1 for statistics. **h,** Structure of NK036, a solubility-enhanced derivative of Compound 39. **i,** Inhibitory potencies of NK036 for indicated USP30 constructs. IC50 values are given as mean ± s.e.m. **j,** Protein stability of indicated USP30 constructs in the presence of NK036.

USP30^{ch3} features unaltered catalytic activity **(Fig. 16c)**, displays an increased protein stability by approx. 4°C **(Fig. 16d)** and reacts readily with Ub-PA **(Fig. 16e-f)**. To validate this chimeric design, the next step was to solve the crystal structure of the covalent USP30^{ch3}~Ub-PA complex **(Fig. 16g, Table 3)**. Both a rather high rate of initial crystal hits in coarse-screening plates and the high resolution of 1.5 Å without crystallization fine-screening supported the hypothesis of increased crystallizability of this chimeric protein.

Inspection of the electron density revealed that the boundary design allowed seamless chimeric sequence transitions and did not perturb the USP fold **(Fig. 17a)**. Consistently, the structure showed a highly similar arrangement compared to Ub-PA complexes of USP30, USP14 and USP35 **(Fig. 17b)**.

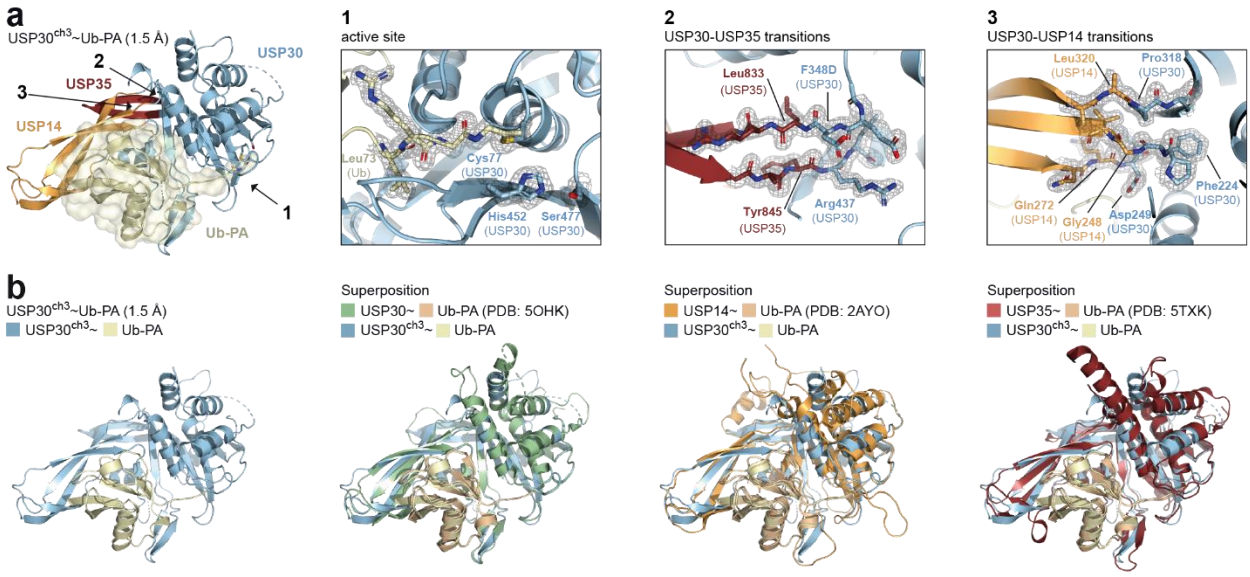

Figure 17 | Crystal structure of USP30^{ch3} in complex with Ub-PA.
a, Cartoon representation of crystal structure of USP30^{ch3}~Ub-PA, with representative 2mFo-DFc electron density (contoured at 1σ shown for indicated areas. **b,** USP30^{ch3}~Ub-PA structure and superpositions with previously reported Ub-PA complexes of USP30c1, USP14 and USP35.

Having validated the chimeric design of USP30^{ch3}, the inhibition of this construct by Compound 39 was next investigated. In the initial crystallization experiments, Compound 39 was noticed to exhibit poor solubility in aqueous buffers. To facilitate the crystallization process, a solubility-enhanced version of Compound 39 called NK036 was developed **(Fig. 16h)**, which features just an additional hydroxyl group at the tert-butyl group, while sharing the 4-fluorobenzoyl group and central L-phenylalanine moiety with Compound 39. Indeed, NK036 showed significantly improved solubility of up to 100 µM in aqueous buffers. While the modification of Compound 39 to NK036 led to decrease in potency by one order of magnitude, NK036 still potently inhibited both USP30^{c1} and USP30^{ch3} similarly at the low nM range **(Fig. 16i)**. More importantly, NK036 significantly improved USP30^{ch3} stability to above 61°C **(Fig. 16j)**, the highest complex stability obtained among all the tested USP30-inhibitor pairs **(Table 2)**. These data underscore the suitability of the highly stable USP30^{ch3}-NK036 pair for co-crystallization studies.

2.4. Crystal structure of USP30^{ch3} in complex with a non-covalent inhibitor

The first crystallization trials of USP30^{ch3}-NK036 yielded moderate-sized crystals which were further improved with fine screening to obtain diffraction quality crystals. The first diffraction measurements yielded rather weak diffraction patterns. A coarse structure solution at 3.2 Å however revealed that the crystals were indeed that of USP30^{ch3}-NK036 complex. This motivated further optimization of crystallization conditions through fine screening and additive screening. The crystal dimensions were improved significantly by 120%, and the diffraction quality from these crystals was also improved. The structure was solved to 2.8 Å, however, with rather high Wilson B-factors because of which clear electron density information for some regions was

missing, especially the 4 β-sheets of the finger sub-domain, and also the placement of the phenyl and fluorophenyl groups of the compound was unclear. To improve the B-factors and resolution, diffraction data from 3 separate crystals were combined through blending/clustering, and after anisotropic scaling, the final structure of USP30^{ch3}-NK036 was solved to a resolution of 2.75 Å **(Table 3, Appendix 3.4-Table 4)**. With the blended data, much of the finger sub-domain (3 out of 4 beta sheets) could be built **(Figs. 18a, 19a)** and the compound had excellent electron density information for all the separate chemical groups **(Figs. 18e-g, 19b)**.

The asymmetric unit contained two copies of the protein-ligand complex. These could be superimposed with a C_α-RMSD of 0.4 Å **(Fig. 18a)** and showed near identical ligand geometries **(Fig. 18b)**. Clear electron density map in a region other than the compound binding site **(Fig. 18c-d)** in both the chains confirmed good quality of the overall structure. However, there were some structural differences noted in between chain A and chain B. Chain A contained more ordered residues near the fingers subdomain, which were partially disordered in chain B, whereas conversely chain B showed ordered loops on the opposite side near the thumb subdomain **(Fig. 18a)**. These differences could be attributed to crystal contacts and notably, these regions are far away from the ligand binding site. Thus, chain A was used for all further analysis. The ligand was embedded in the core of USP30, spatially separated from the chimeric portions. This indicates that the chimeric engineering of USP30 does not influence/affect *bona fide* USP30 inhibition mechanism.

Table 3. Data collection and refinement statistics.

	USP30^{ch3}~Ub-PA (PDB: 9F6G)	**USP30^{ch3} + NK036 (PDB: 9F19)**
Data collection		
Beamline	ESRF ID30A-3	ESRF ID30A-3
Wavelength (Å)	0.9677	0.9677
Space group	$P\ 2_1\ 2_1\ 2_1$	$P\ 2_1\ 2\ 2_1$
Cell dimensions		
a, *b*, *c* (Å)	46.64, 50.71, 156.56	55.83, 73.84, 201.05
α, β, γ (°)	90, 90, 90	90, 90, 90
Anisotropy correction	no	yes
Observed reflections	362,140	214,419
Unique reflections	58,606	15,438
Resolution (Å)	46.64 – 1.50 (1.53 – 1.50)	59.52 – 2.75 (3.23 – 2.75)
Ellipsoidal resolution limits (Å) [direction]	- - -	2.89 [a*] 3.53 [b*] 2.75 [c*]
R_{merge}	0.073 (1.240)	0.166 (1.536)
R_{meas}	0.080 (1.350)	0.173 (1.595)
$I/\sigma(I)$	10.7 (1.4)	9.6 (1.9)
$CC_{1/2}$	0.998 (0.426)	0.998 (0.730)
Spherical completeness (%)	97.1 (96.8)	68.7 (26.2)
Ellipsoidal completeness (%)	-	91.9 (69.0)
Redundancy	6.2 (6.4)	13.9 (13.9)
Wilson *B* (Å^2) [direction]	18	82 [a*] 161 [b*] 71 [c*]
Refinement		
Copies / a.s.u.	1	2
Resolution	1.50 Å	2.75 Å
No. reflections	58,467	15,431
R_{work} / R_{free} (%)	18.3 / 21.1	21.8 / 26.6
No. atoms (non-hydrogen)	3,126	3,932
Protein	2,767	3,791
Ligand	4	72
Water	355	69
B factors (Å^2)	29.0	79.2
Protein (Å^2)	27.6	79.6
Ligand (Å^2)	22.4	68.8
Water (Å^2)	40.0	66.8
R.m.s.d.		
Bond lengths (Å)	0.014	0.008
Bond angles (°)	1.33	1.05

Ramachandran (favored / allowed / outlier) (%)	99.4 / 0.6 / 0.0	97.2 / 2.8 / 0.0
Clashscore	1	3
Rotamer outliers (%)	0.7	1.8

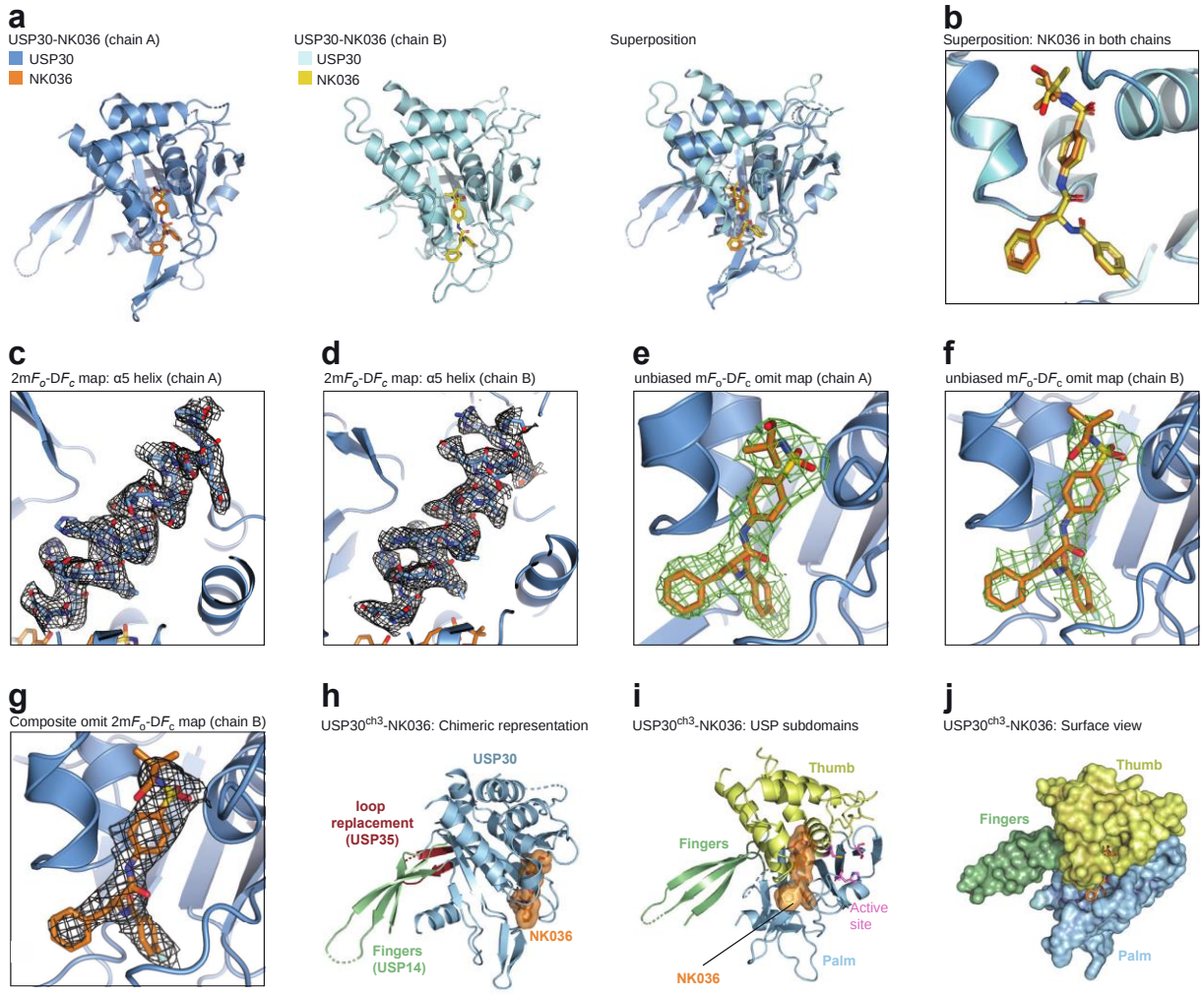

Figure 18 | Crystal structure of USP30 in complex with NK036.

a, Cartoon representations of the two copies within the asymmetric unit in the crystal structure of USP30^{ch3}-NK036. **b,** Close-up view of the superposition shown in a highlighting the ligand geometries in both chains. **c-d,** Representative electron density map of the α5 helix in chain A (panel c) and chain B (panel d). 2mF_o-DF_c density, contoured at 1σ, with –30 Å^2 *B*-factor sharpening, is shown covering all atoms of the region. **e-f,** Unbiased electron density omit map of NK036 in chain A (panel e) and chain B (panel f). A mF_o-DF_c map, contoured at 1σ, covering all atoms of the compound is shown, which was calculated from the protein geometry before the ligand was modelled. **g,** Composite omit electron density map of NK036 in chain B (2mF_o-DF_c, contoured at 1σ, covering all atoms of the compound, created as described for Fig. 2b). **h,** Structure as in a, with chimeric elements shown in different colors. Of note, no chimeric residue is near the

compound binding site. **i,** Cartoon representation of crystal structure of USP30^{ch3}-NK036, highlighting different USP subdomains. The compound is shown under an orange surface, active site residues are shown in pink. **j,** Structure as in panel e with surface representation of USP30 highlighting different USP subdomains.

The structure shows that NK036 binds at the interface of palm and thumb subdomains **(Fig. 18i-j)**. The phenylalanine and fluorophenyl moieties are surrounded by blocking loops 1 and 2 in the palm subdomain, whereas, the benzenesulfonamide moiety is embedded in the core of the thumb subdomain which is enclosed by the switching loop and the helices α1, α4 and α5 **(Fig. 19c-d)**.

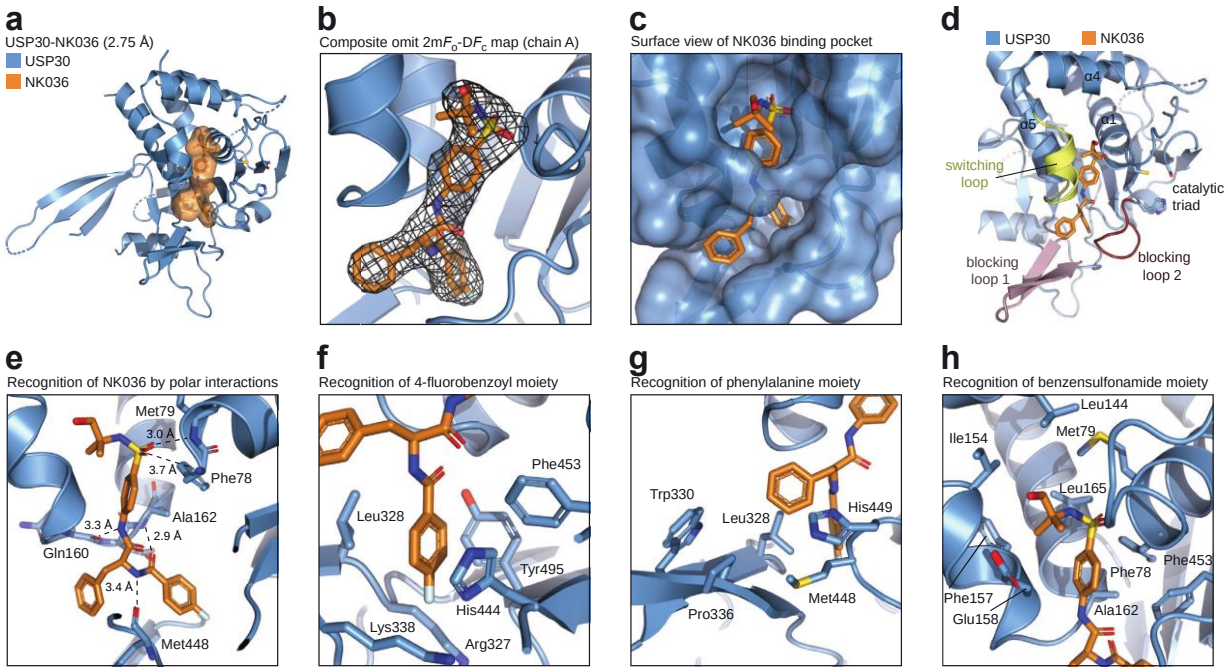

Figure 19 | Compound binding site in the structure of USP30 in complex with NK036.
a, Cartoon representation of the crystal structure of USP30^{ch3} bound to NK036. The compound is shown under an orange surface. **b,** Composite omit electron density map of NK036 in chain A (2mF_o-DF_c, contoured at 1σ, covering all atoms of the compound, created with simulated annealing from the final coordinates). See Extended Data Fig. 5e-f for unbiased mF_o-DF_c maps. **c,** Structure as in panel a, with surface representation of USP30. **d,** Compound binding site highlighting typical USP regions involved in binding to NK036. **e,** Close-up view of the compound binding site highlighting key residues involved in H-bonding. **f,** Close-up view of the USP30 hydrophobic patch engaging the fluorobenzoyl moiety of the compound. **g,** Close-up view of hydrophobic interactions of the phenylalanine group of the compound. **h,** Close-up view of the benzenesulfonamide moiety of the compound engaged by USP30 residues.

The interactions of NK036 with USP30 spread across three distinct regions:

(i) The fluorophenyl group is held in a hydrophobic enclosure formed by the side chains of Leu328, Tyr495, Phe453 and His444, and the main chains of Lys338 and Arg327. The fluorophenyl group forms parallel π- π stacking interaction with His444 **(Fig. 19f)**.

(ii) The central phenyl ring forms hydrophobic interactions with side chain of Leu328 and main chain of Met448 and parallel π- π stacking interaction with His449 **(Fig. 19g)**. It is worth noting that the tip of this phenyl ring is near to Trp330 and Pro336 on blocking loop 1, but not too close to form interactions, thus leaving space for SAR-based modifications. This is in line with featuring sterically more demanding groups instead of the phenyl ring also displaying potent USP30 inhibition (*66*).

(iii) The benzenesulfonamide moiety is surrounded by Ala162, Phe78, Phe453 and the aliphatic part of the Glu158 side chain **(Fig. 19h)**. The sulfonyl group forms polar contacts with Phe78 and Met79 amides **(Fig. 19e)**. The tert-butyl group is bound in a hydrophobic cleft which is formed towards the top by Met79, Leu165 and Leu144 side chains, and on the side by Ile154 and Phe157. The addition of hydroxyl group in this predominantly hydrophobic environment explains the loss in potency of NK036 as compared to Compound 39 **(Fig. 16h-i)**, as well as the tolerance of other hydrophobic structural elements at this position within the compound series **(Fig. 10)** (*66*, *96*).

Thus, the structure of USP30^{ch3}-NK036 shows how the compound is held at the core of USP30 through various interactions expanding in three distinct regions over a large interaction surface of 570 Å^2, which supports the elegant design and high potency of the benzensulfonamide class of USP30 inhibitors. The structure also sheds some light on previously observed SAR behaviours of USP30 compounds and provides opportunities for further SAR-based compound development.

Interestingly, the pocket of USP30, in which the benzenesulfonamide moiety of NK036 is embedded, is a novel cryptic pocket opened up by unexpected conformational changes. The mechanism as to how NK036 binding induces these conformational changes, allowing tight binding of NK036, is further analyzed below.

2.5. Conformational plasticity of the switching loop and engagement of the Leu73 pocket underly USP30 ligand binding: basis of inhibitor potency

To understand how NK036 inhibits USP30, a structural superposition of USP30-NK036 with a previously solved USP30~Ub-PA structure was analyzed **(Fig. 20a-d)**. Structural superposition highlights three observations as to how NK036 inhibits USP30:

(i) NK036 does not directly contact the catalytic residues, but NK036 binding does influence the catalytic site by inducing misalignment of the catalytic triad as shown by His452 which is flipped out of the optimal conformation in the inhibitor-bound state **(Fig. 20d)**.

(ii) The fluorophenyl moiety of NK036 occupies a hydrophobic pocket which generally acts as a ubiquitin Leu73 binding pocket across all USP DUBs **(Fig. 20e)**. This pocket is important in guiding the ubiquitin C-terminus to the catalytic site, and inhibitor binding into this pocket blocks the entry of ubiquitin C-terminus to the active site, thus hampering USP30 catalytic activity in a substrate competitive manner.

(iii) The benzenesulfonamide moiety of NK036 is lodged deeply within the thumb subdomain of USP30 in a cryptic pocket which is opened up by large and unexpected conformational changes of the switching loop **(Fig. 20g-h)**. This mechanism occurs by compound-induced conformational changes of residues on and around the switching loop. Upon compound

binding, Phe78 moves inwards, leading to displacement of Ala162 outwards. This causes the tip of the α5 helix to move outwards by about 3 Å to generate a pocket, allowing entry of the benzenesulfonamide moiety of NK036 into the core of USP30 thumb subdomain **(Fig. 20g)**. Within this pocket, NK036 is further accommodated by a significantly large conformational change of the switching loop represented by Phe157 which moves more than 18 Å to take the place of Trp152 which in turn moves outwards. This surprising conformational change of the switching loop is accompanied by a loop-to-helix transition, with residues 154-159 forming a two-turn alpha helix, further consolidating compound binding within this cryptic pocket **(Fig. 20h)**.

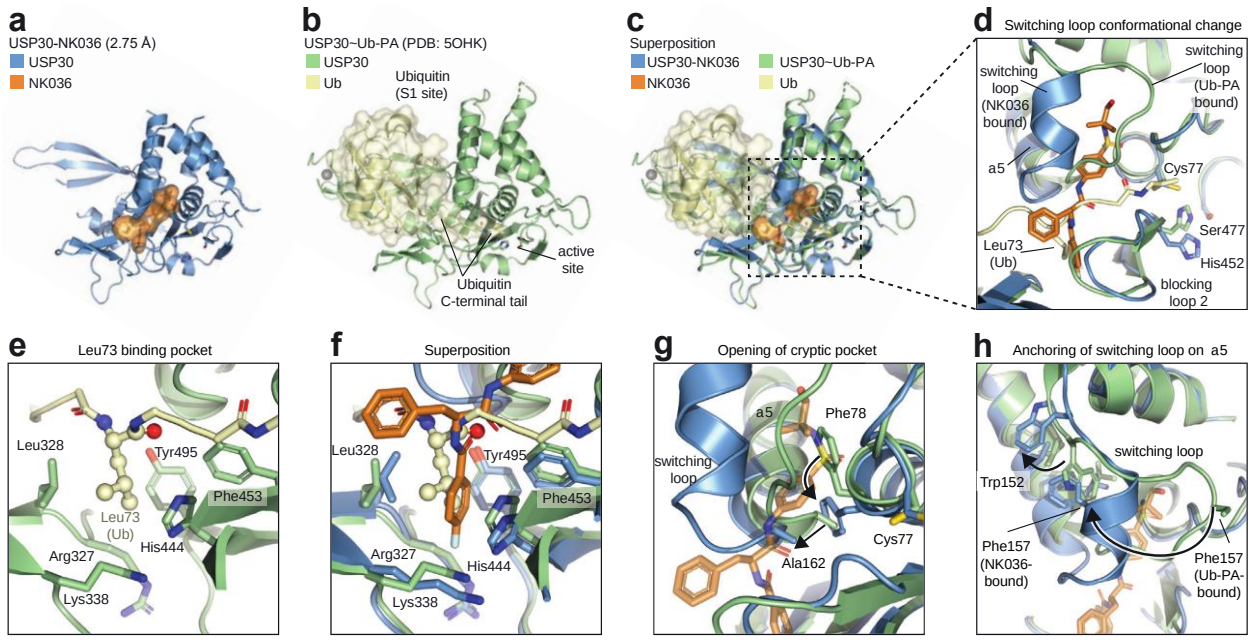

Figure 20 | Engagement of the Leu73 pocket and conformational plasticity of the switching loop underlie ligand engagement by USP30.

a, Cartoon representation of the crystal structure of USP30 bound to NK036. The compound is shown under an orange surface. **b,** Structure of USP30~Ub-PA complex (PDB: 5OHK). Ubiquitin is shown under a yellow surface. **c,** Superposition of panels a and b. **d,** Close-up view of the compound binding site. Catalytic triad residues of USP30 and Leu73 of Ubiquitin are labeled. The conformational change of the USP30 switching loop is indicated. **e,** Close-up view on the engagement of the Ubiquitin Leu73 side chain by USP30, with residues forming the hydrophobic pocket highlighted. **f,** Superposition of the structures,

focused on the Leu73 binding pocket showing its occupation by the fluorobenzoyl group of NK036. **g-h,** Close-up views of the conformational changes of the switching loop, focusing on entry of the cryptic pocket within the thumb subdomain (g) and the anchoring of the switching loop on the α5 helix (h). Putative movements of residues are indicated with arrows.

Thus, the structure reveals NK036 binding to USP30 in two modes: in a substrate competitive manner hampering USP30 catalytic activity, and binding tightly into a cryptic pocket in the USP30 thumb subdomain core by inducing large conformational changes, explaining the basis of high potency of the benzenesulfonamide class of USP30 inhibitors and also the previously observed pseudo-covalent mode of slow and tight binding of Compound 39. Interestingly, such a large shift in the switching loop and loop-to-helix transition upon compound binding has not been observed for USP30 or any USP DUB structures before **(Fig. 21a-h)**. Thus, the structure also reveals a remarkably novel mode of USP DUB inhibition.

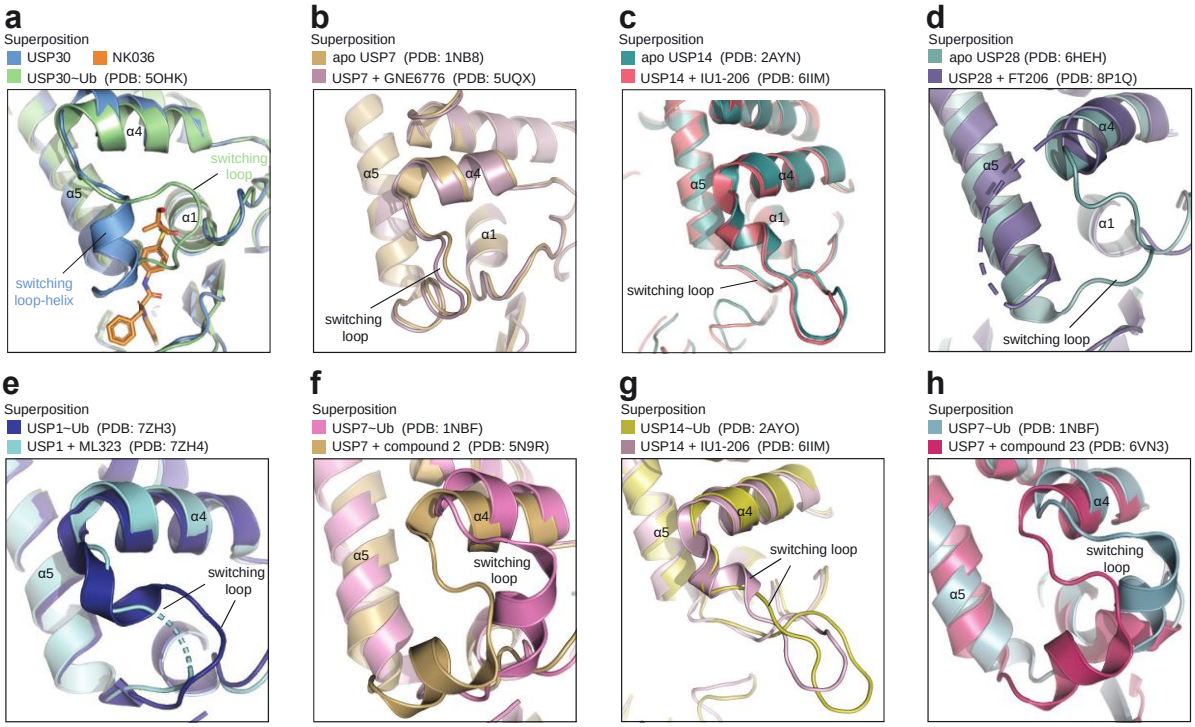

Figure 21 | Conformational change of USP DUB switching loop upon compound binding. **a-h,** Structural superpositions showing the switching loop positions in different USP DUBs, comparing compound-bound to ubiquitin-bound or apo states.

Having established the basis of potency of the benzenesulfonamide class of inhibitors, the next step was to investigate how these inhibitors are so highly selective towards USP30.

2.6. Molecular basis for specific inhibition of USP30

2.6.1. Key specificity factors

To understand the basis of high specificity of the benzenesulfonamide class of USP30 inhibitors both in cells and in vitro (*89, 91*), the NK036 binding site was investigated closely to look for residues unique to USP30. Two residues stood out which are completely unique to USP30 among the entire human USP family members: Leu328 where other DUBs have a phenylalanine, and Phe453 where other DUBs contain a tyrosine **(Fig. 22a)**. Notably, these two residues face the compound directly at the center of the compound binding site **(Fig. 22b)**. Structural superposition with other USP DUBs shows that phenylalanine in place of the Leu328 would clash with the fluorophenyl group of NK036, and the phenolic hydroxyl group of tyrosine in place of the Phe453 would clash with the carbonyl oxygen of the NK036 amide. Thus, Leu328 and Phe453 in USP30 could very well be the specificity factors for compound binding.

To test this hypothesis, two point mutants of USP30^{ch3}: L328F and F453Y were generated. L328F exhibited loss in activity and was not suitable for enzyme inhibition assay **(Figs. 22d, 23a-b)**. F453Y however retained about 1/3 of activity, while maintaining robust Ub-RhoG cleavage **(Figs. 22d, 23a)**, which was suitable enough for enzyme inhibition assay. F453Y mutation led to massive loss in potency of NK036 by two orders of magnitude **(Fig. 22e)**. Consistently, both mutant proteins exhibited significant loss in NK036 binding as shown by thermal shift assay **(Fig. 22f)**. These assays when repeated with Compound 39 yielded similar results **(Fig. 22g-h)**, with F453Y mutation causing loss in

potency of Compound 39 by three orders of magnitude. These mutants were further validated through a competitive probe labeling assay **(Fig. 23h)**. Preincubation of wild type USP30 with inhibitors largely abrogated labeling of USP30 with Ub-PA, whereas USP30 carrying the F453Y and L328F mutations showed complete labeling even in the presence of the inhibitors, thus establishing these two mutants as compound resistant. Together, these assays confirm that Leu328 and Phe453 are indeed the key factors that facilitate specific inhibition of USP30.

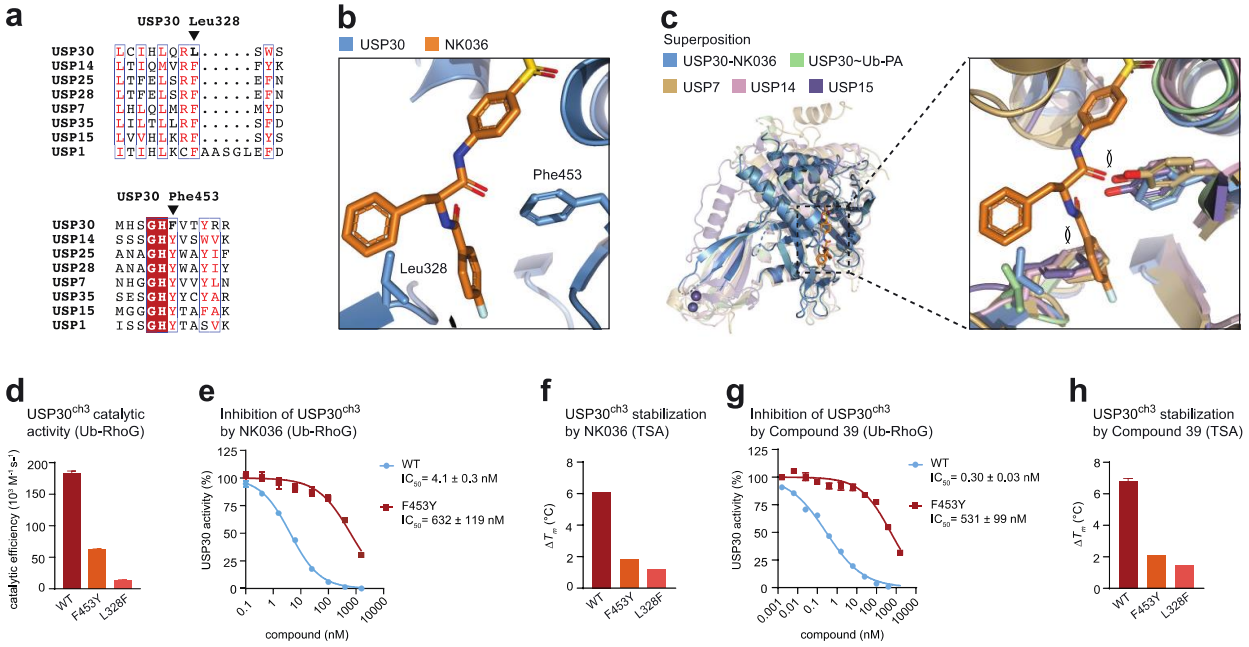

Figure 22 | Molecular basis of inhibitor specificity for USP30.
a, Sequence alignment of indicated human USP DUBs. Arrows indicate the unique Leu328 and Phe453 residues in USP30. **b,** Close-up view of the compound binding site. **c,** Superposition with indicated USP DUB structures in complex with inhibitors (PDB: 5N9R, 6IIN, 6GH9), highlighting how equivalent Phe and Tyr residues in other human USP DUBs interfere with compound binding. **d,** Catalytic activities of indicated wild-type (WT) and mutant USP30 proteins, assessed by Ub-RhoG cleavage. Mean ± s.e.m. **e,** Inhibitory potencies of NK036, pre-incubated with indicated USP30 proteins for 1.5 h, determined from Ub-RhoG cleavage assays. IC50 values are given as mean ± s.e.m. **f,** Protein stability of indicated USP30 proteins in the presence of 20 µM NK036. ΔT_m was calculated as T_m of the compound-bound sample subtracted from T_m of the respective apo protein. Mean ± s.d. (N=3). **g,** Inhibitory potencies of Compound 39, determined as in e. **h,** Protein stability assessment in the presence of Compound 39, determined as in f.

2.6.2. Additional specificity factors

To assess the importance of the USP30 switching loop and the cryptic pocket, three additional compound-resistant mutations were selected based on Phe157 (its large conformation change is described in Fig. 20h), Ala162 (the gatekeeper residue of the cryptic pocket) and Ile154 (in the upper part of the thumb subdomain, contacting the sulfonamide) **(Fig. 20g-h)**. Notably, these residues are unique to USP30 **(Fig. 23c)**. The mutants significantly retained enzyme activity and were suitable for enzyme inhibition assays **(Fig. 23a-b)**. In vitro assays confirmed reduced inhibitory potency as well as reduced stabilization by compounds for the F157A, I154A and A162S mutations **(Fig. 23d-g)**. Through competitive probe labeling assay as described in 2.6.1., it was observed that USP30 carrying these mutations was refractory to inhibition by both NK036 and Compound 39 **(Fig. 23i)**.

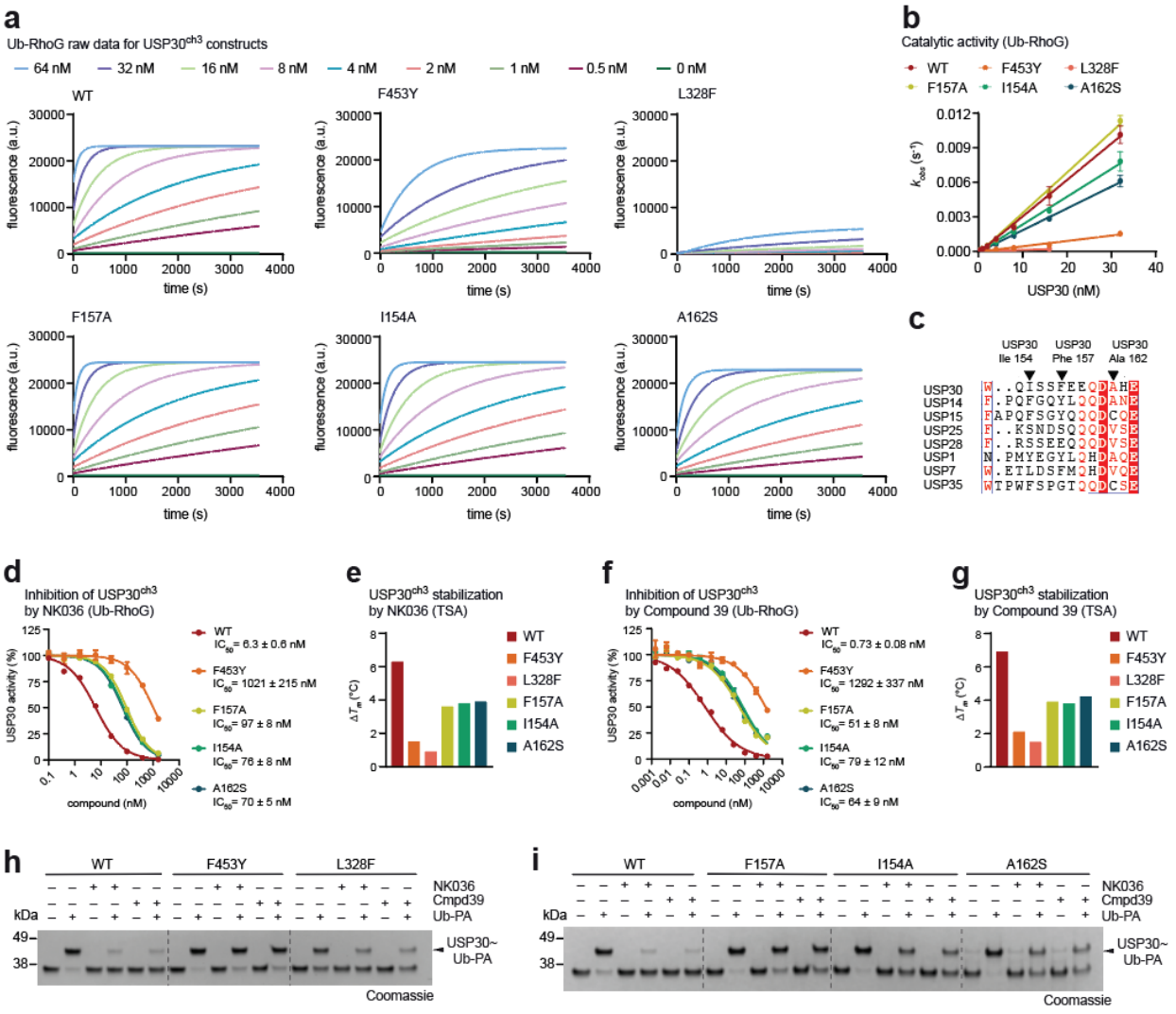

Figure 23 | Profiling of the factors of inhibitor specificity for USP30.

a-b, Quantification of USP30 enzyme activity for WT and indicated mutant proteins, as described in Fig. 15 d-e. **c,** Sequence alignment of indicated human USP DUBs. Arrows indicate Ile154, Phe157 and Ala162 residues in USP30. **d,** Inhibitory potencies of NK036, pre-incubated with indicated USP30 proteins for 1.5 h, determined from Ub-RhoG cleavage assays. IC50 values are given as mean ± s.e.m. **e,** Protein stability of indicated USP30 proteins in the presence of 20 μM NK036. ΔT_m was calculated as T_m of the compound-bound sample subtracted from T_m of the respective apo protein. Mean ± s.d. (N=3). **f,** Inhibitory potencies of Compound 39, determined as in panel d. **g,** Protein stability assessment in the presence of Compound 39, determined as in panel e. **h,** Probe competition assay. USP30 and inhibitors were preincubated, followed by addition of Ub-PA, and analysis of samples by SDS-PAGE and Coomassie staining. **i,** Probe competition assay performed as in panel h with mutations characterized in panels d-g.

2.6.3. Cellular validation of specific inhibition

To assess compound binding to full length endogenous USP30, a competitive probe labeling approach as described in 2.6.1. was used. In presence of the inhibitors, the reactivity of USP30 to Ub-PA was completely abrogated, confirming strong inhibition effects of these compounds towards full length endogenous USP30 **(Fig. 24b)**. Next, Flag-tagged, full-length USP30 was overexpressed in HEK293 cells to compare probe labeling of wild-type and mutant USP30 **(Fig. 24c)**. The F453Y mutant was chosen for analysis as it retained activity and showed clear compound-probe competition behaviour in vitro **(Figs. 23a-b, 23h)**. Treatment of cells for 2 h with either Compound 39 or NK036 abolished probe labeling of the wild-type protein. In contrast, USP30 carrying the F453Y mutation was equally labeled by the ubiquitin probe when cells were previously treated with inhibitors, thus confirming compound resistance of the F453Y mutation in a cellular context **(Fig. 24c)**. To assess the switching loop/cryptic pocket mutants of USP30 in a cellular context, Flag-tagged, full-length USP30 carrying the mutations F157A, A162S and I154A in a competitive probe labeling assay were analyzed as described above. These mutants were observed to be resistant to both the compounds **(Fig. 24d)**.

To assess the mechanism of USP30 inhibition in a cellular context, firstly, the action of NK036 on endogenous USP30 was determined. For this purpose, the established mitophagy model system of HeLa cells constitutively expressing YFP-Parkin (*62*) was used, and the recently introduced ubiquitin binding domain derived from an Orientia tsutsugamushi DUB (OtUBD) was applied to this system for the enrichment of ubiquitinated proteins (*97, 98*). Increased ubiquitination of USP30 substrates was observed upon USP30 inhibition shortly after mitochondrial depolarization **(Fig. 24a)**. Specifically, Compound 39 and NK036 elevated the polyubiquitination of Tom20 and

Tom40, while not affecting the polyubiquitination of Mitofusin-2, thus confirming the mode of action of USP30 inhibitors towards improvement in mitophagy.

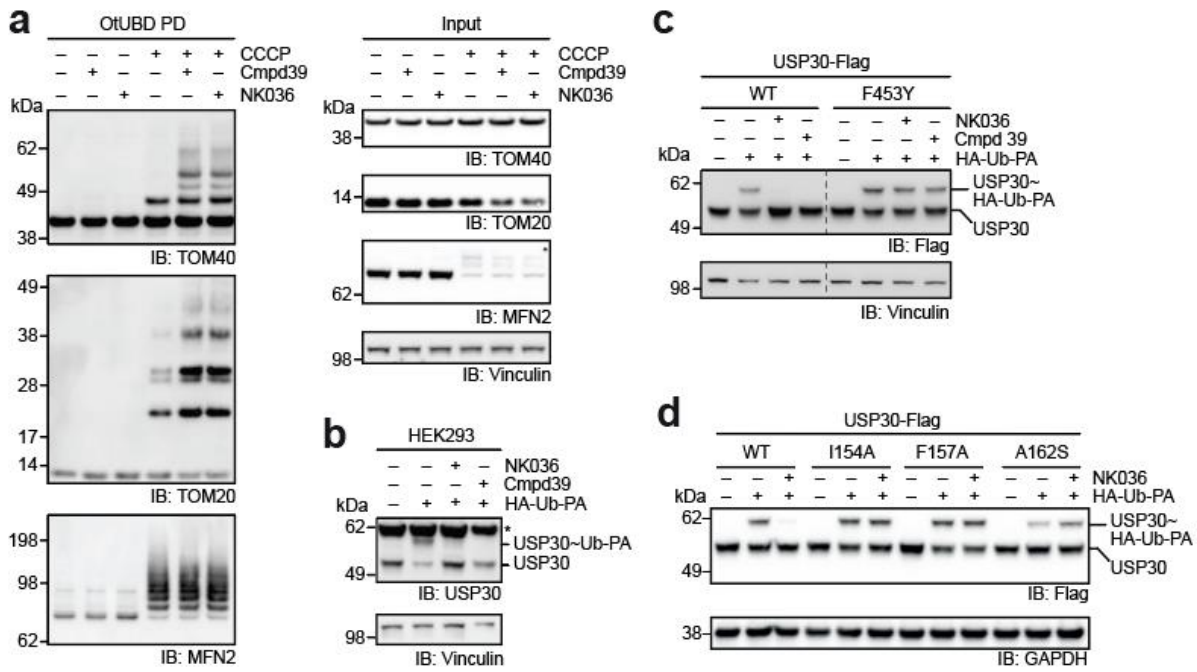

Figure 24 | Cellular evaluation of compound resistant USP30 mutations.
a, Mitochondrial ubiquitination analysis. HeLa cells expressing YFP-Parkin were treated with USP30 inhibitors for 19 h where indicated. Mitophagy was induced with CCCP for 1 h. Ubiquitinated proteins were enriched through pulldowns with OtUBD, and samples were analyzed by Western Blot. **b,** Target engagement assay with endogenous USP30. HEK293 cells were treated with indicated compounds. Lysates were then incubated with ubiquitin probe where indicated and analyzed by western blot for USP30. The asterisk denotes an unspecific band. **c,** Cellular assessment of USP30 inhibition mechanism. C-terminally Flag-tagged USP30 (WT or with compound-resistant mutation F453Y) was overexpressed in HEK293 cells. Cells were analyzed as described in panel b, with a western blot for the Flag tag. **d,** Cellular probe competition assay as described in panel c with mutations characterized in Fig. 23 d-g. All data in this figure were generated by Kai Gallant and Gian-Marvin Kipka (Gersch group – CGC).

Having established the molecular basis of specific inhibition of USP30 and the mechanism of USP30 inhibitors in cells, the study was further expanded to compare the mode of USP30 inhibition with that of other USP DUB inhibitors.

2.7. NK036 engages a USP DUB ligandability hotspot in unique manner

To place the mode of USP30 inhibition by NK036 in context to the overall trends in USP DUB inhibition, some representatives of existing USP DUB-inhibitor co-crystal structures were compared. These included USP7 in complex with hydroxypiperidine inhibitors **(Fig. 25a)** (*50*, *94*, *95*), USP7 in complex with an allosteric inhibitor **(Fig. 25b)** (*93*), USP14 bound to IU1-206 **(Fig. 25c)** (*45*), USP28 in complex with FT206 **(Fig. 25d)**(*55*, *99*), USP1 in complex with ML323 **(Fig. 25e)** (*58*), and USP7 in complex with Compound 23 **(Fig. 25f)** (*51*).

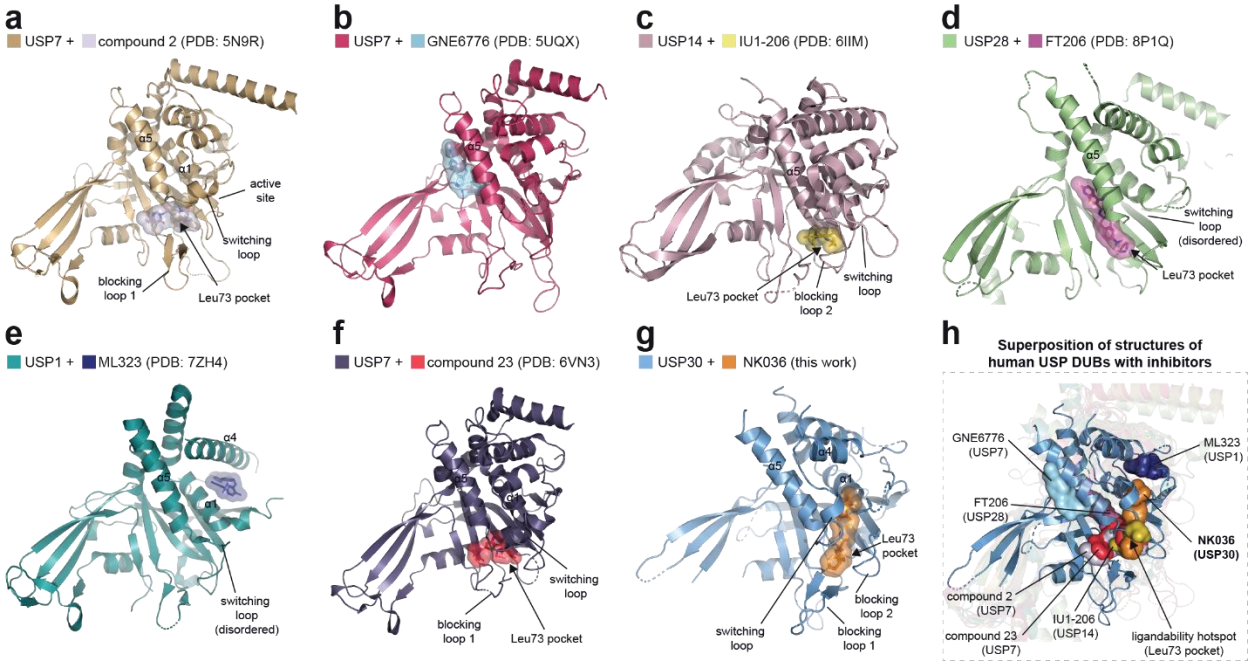

Figure 25 | Inhibition of USP30 by NK036 uses a ligandability hotspot and a cryptic pocket, distinct from other USP DUB inhibitors.

a-g, Cartoon representations of human USP-family deubiquitinase catalytic domains in complex with indicated small molecule inhibitors. Compounds are shown as both sticks and transparent surfaces. Structural elements of DUBs are labeled and PDB codes of structures are given. The Leu73 Ubiquitin binding site is shown with an arrow when engaged by compounds. **h,** Comparison of USP30 inhibition by NK036 to other DUB inhibitors. Superposition of the structure of USP30+NK036 on other structures shown in panels a-f. Compounds are shown as surfaces and are labeled. All USP cartoons except USP30 are semitransparent**.**

In addition, the binding mode to a covalent USP7 inhibitor (*50*) as well as to an inhibitor of the USP-fold SARS-CoV PLpro enzyme were compared **(Fig. 26a-d)** (*100, 101*).

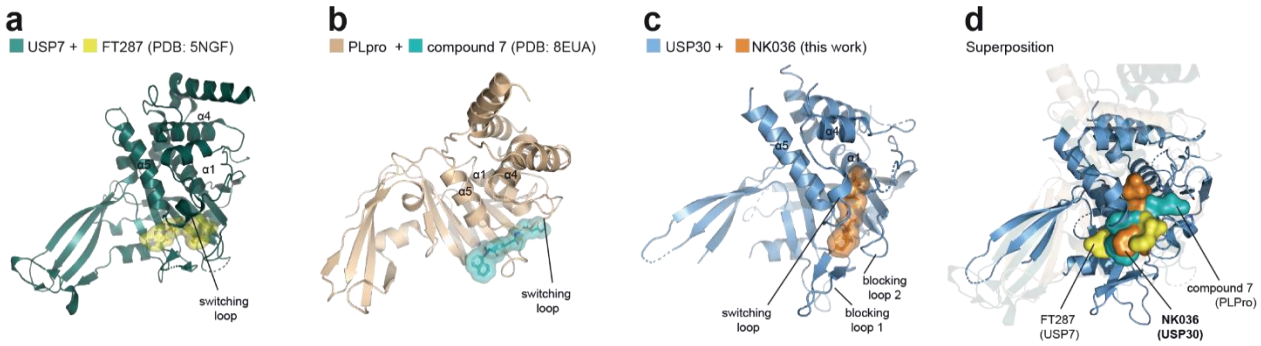

Figure 26 | Comparison of the binding mode of NK036 to covalent USP DUB inhibitors.
a-c, Cartoon representations of the crystal structures of USP7, SARS-CoV2-PLPro and USP30 in complex with respective inhibitors. Compounds are shown as surfaces. **d,** Superposition of the structure of USP30+NK036 on other structures shown in panels a-c. Compounds are shown as surfaces and are labeled. All protein cartoons except USP30 are semitransparent.

Superposition of all structures with the obtained USP30-NK036 geometry revealed the benzenesulfonamide moiety of NK036 to engage a previously unexplored pocket within the USP domain **(Fig. 25g-h)**. NK036 is the only USP DUB inhibitor passing through the switching loop and lodging into the core of the thumb subdomain in between the α4, α5 and α1 helices of the thumb sub-domain while the other USP inhibitors bind in distinct pockets around the thumb core **(Fig. 25h)**.

While the different USP DUB inhibitors bind at different USP pockets, they seem to converge at a particular region, which is the ubiquitin Leu73 binding site **(Fig. 25h)**. This structural analysis hypothesizes that the Leu73 pocket is a common anchoring site for USP DUB inhibitors. This hypothesis is supported by closer analysis of the structural superpositions, revealing the para-fluorophenyl group of NK036 to engage the Leu73 Ubiquitin binding site of USP30 in the same way as the chemically related para-chlorophenyl- and 3-fluoropyrazole groups of USP7 and

USP14 inhibitors, which are otherwise structurally completely unrelated **(Fig. 27)** (*45, 50, 51*). Thus, this dissertation proposes the binding pocket of DUBs for the Ubiquitin Leu73 side chain as a general USP DUB ligandability hotspot. The structural analysis here reveals that NK036 engages USP30 through precisely this hotspot in a unique manner as it also expands through its benzenesulfonamide moiety into a cryptic pocket in the thumb subdomain, which is generated through conformational plasticity of the switching loop.

	DUB	Inhibitor = Leu73 (Ub) position occupying element	Superposition of DUB:inhibitor structure with DUB:Ubiquitin structure highlighting Leu73 →	Superposition of DUB:inhibitor structure with USP30:NK036 structure highlighting Leu73 site occupying element
a	**USP7**	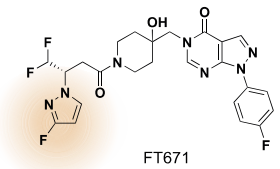 FT671	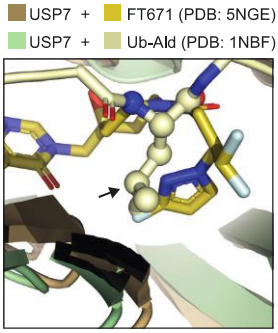 USP7 + FT671 (PDB: 5NGE) USP7 + Ub-Ald (PDB: 1NBF)	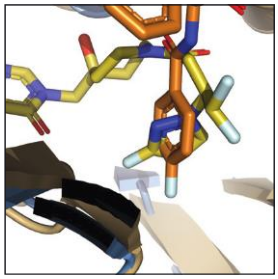 USP7 + FT671 (PDB: 5NGE) USP30 + NK036
b	**USP7**	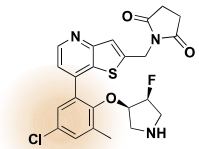 Cpd23	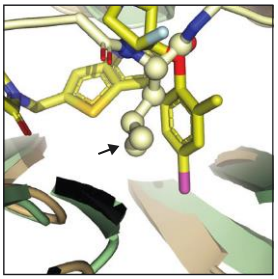 USP7 + Cpd23 (PDB: 6VN3) USP7 + Ub-Ald (PDB: 1NBF)	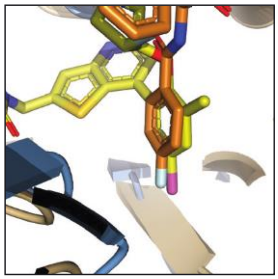 USP7 + Cpd23 (PDB: 6VN3) USP30 + NK036
c	**USP14**	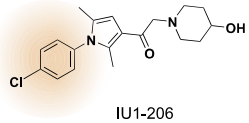 IU1-206	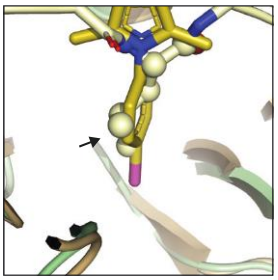 USP14 + IU1-206 (PDB: 6IIM) USP14 + Ub-Ald (PDB: 2AYO)	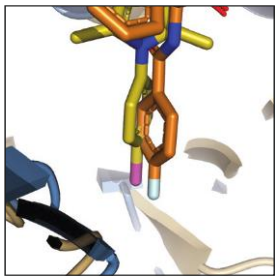 USP14 + IU1-206 (PDB: 6IIM) USP30 + NK036
d	**USP28**	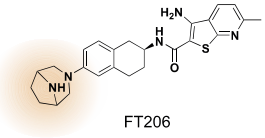 FT206	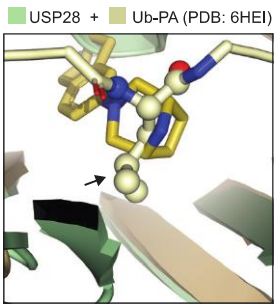 USP28 + FT206 (PDB: 8P1Q) USP28 + Ub-PA (PDB: 6HEI)	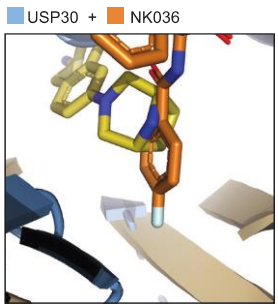 USP28 + FT206 (PDB: 8P1Q) USP30 + NK036

Figure 27 | A common DUB ligandability hotspot and a shared hotspot anchor

a-d, Chemical and structural representations of inhibitors of USP7 (a, b), USP14 (c) and USP28 (d). Shown are the overlays of the inhibitor-bound structures with ubiquitin-bound structures of the respective DUBs (first box) and the inhibitor-bound structures of each DUB overlaid on NK036 bound structure of USP30 (second box). Highlighted is the close-up view of the compound binding site at the ubiquitin Leu73 pocket. Chemically related hotspot anchors are indicated with black arrows. Structural superpositions were aligned taking only the protein residues into account. The chemical moieties of the inhibitors that occupy the Leu73 pocket are highlighted with orange background.

2.8. Summary

The ubiquitin system is at the core of almost all cellular processes, thereby providing great potential in the modulation of ubiquitin signaling with small molecules. A class of enzymes in the ubiquitin system called the Deubiquitinases (DUBs) are emerging as targets for such small molecule-mediated modulation. DUBs are critical regulators of the ubiquitin system and are involved in various diseases. DUB inhibition by small molecules has been proven to amplify ubiquitin-dependent processes, thereby attracting the development of small molecule DUB inhibitors as therapeutics. In fact, inhibitors targeting two DUBs have entered into clinical trials.

One of these is the mitochondrial DUB USP30 which is a critical factor in mitophagy disorders. The role of USP30 inhibitors towards improved mitophagy in Parkinson's disease and kidney disease is currently being explored in clinical trials, with inhibitors recently progressed through phase II. However, the mode of specific inhibition of USP30 at the molecular level is still unknown, because of lack of USP30 structures, which greatly hinders USP30 targeting therapeutics development. This dissertation reports a crystal structure of USP30 in complex with a potent neurodegeneration-relevant inhibitor that was achieved through an advanced chimeric protein engineering approach.

The structural investigation here reveals the molecular basis for potent and specific inhibition of USP30. The inhibitor NK036 uses its fluorobenzoyl moiety to occupy the unique Leu73 recognition pocket of USP30 and additionally occupies a cryptic pocket within the thumb subdomain with its benzenesulfonamide group **(Fig. 28a-b)**. This tight binding mode is facilitated by a large conformational shift in the switching loop and a loop to helix transition of the switching loop upon inhibitor binding. This conformation of the switching loop is unique to USP30, setting it apart from all other DUB:inhibitor complexes. The switching loop adopting a helix was previously observed in the context of USP7 inhibition (*50*), however, this conformation was independent of inhibitor binding as it was already present in the apo and ubiquitin-bound structures of USP7 and did not show large conformational changes upon inhibitor binding, unlike in the case of USP30-NK036. Without an apo structure of USP30 it is difficult to conclude that the unique conformation of the USP30 switching loop is indeed an inhibitor-induced de novo state and is not already present in the apo state or apo/ubiquitin-bound hybrid state, as was observed in the case of UCHL1-inhibitor structures (*102*). However, the observations that the switching loop shows very high flexibility by HDX-MS in the apo state (*71*, *91*) and that the observed conformation is incompatible with ubiquitin binding strongly suggest that this conformation of the switching loop is neither present in the apo state nor in the apo/ubiquitin-bound hybrid state, but is definitely an inhibitor-induced conformation, which is facilitated by structural plasticity of the switching loop. This study thus highlights that conformational changes of the DUB need to be considered when assessing modes of inhibition.

Structural comparisons also showed that a hydrophobic DUB pocket used for the anchoring of ubiquitin Leu73 sidechain is also used by DUB inhibitors as an anchoring spot, thus emerging as a DUB ligandability hotspsot. It is striking to observe that DUB inhibitors bind commonly at this

hotspot and branch out to distinct specific pockets of the USP catalytic domain to achieve selective DUB inhibition **(Fig. 28c)**. Covalent USP7, PLpro and UCHL1 inhibitors extend towards the catalytic cysteines to bind these with electrophilic handles, whereas non-covalent USP7, USP14 and PLpro inhibitors extend into the opposite direction towards the S1 Ubiquitin binding site and the blocking loops. USP28 inhibitors extend into a pocket underneath the α5 helix, while NK036 extends into a cryptic pocket formed by the switching loop adjacent to α5.

Excitingly, this analysis also allowed the identification of highly related chemical moieties which occupy the hydrophobic Leu73 ligandability hotspots in structurally otherwise unrelated DUB inhibitors for different enzymes (compare the para-chlorophenyl groups in USP7 and USP14 inhibitors Compound 23 and IU1-206, respectively, and the 4-fluorophenyl group in NK036 as hotspot anchor elements, **Figs. 28d, 27b-c**). This chemical feature thus appears to be a privileged structure for non-covalent DUB inhibition.

Based on the structural analysis of common chemical moieties in USP DUB inhibitors, this dissertation proposes a conceptual framework for specific USP DUB inhibition which is centered on the engagement of a common ligandability hotspot in the Leu73-Ubiquitin binding site paired with diverse compound extensions (**Fig. 28c-d**). With more structures emerging, this framework can be applied to design DUB inhibitors with common hotspot anchoring moieties as well as distinct branching moieties that bind to distinct and possibly unexplored DUB pockets (like in the case of USP30-NK036), thus establishing a roadmap towards rapid development of novel DUB inhibitors in a global manner similar to well established inhibitor development systems such as kinases.

This work also underscores the practical importance of such a chimeric engineering approach to enhance the crystallization propensity of USP catalytic domains. The chimeric engineering

approach in this dissertation is supported by previous engineering strategies for DUB crystallization including insertion deletion for USP4, USP25, USP28, USP30 (*53*, *55*, *71*, *99*, *103*), domain swapping for USP11 (*104*), and surface residue mutations for USP9X, USP30 (*71*, *105*). We expect that this approach will lead to a generalizable crystallization platform to enable structure-based drug design for other USP DUBs.

Collectively, this dissertation illuminates the potential of cryptic pockets and conformational dynamics to obtain specific DUB inhibitors and advances the structure-based design of therapeutics targeting neurodegenerative diseases.

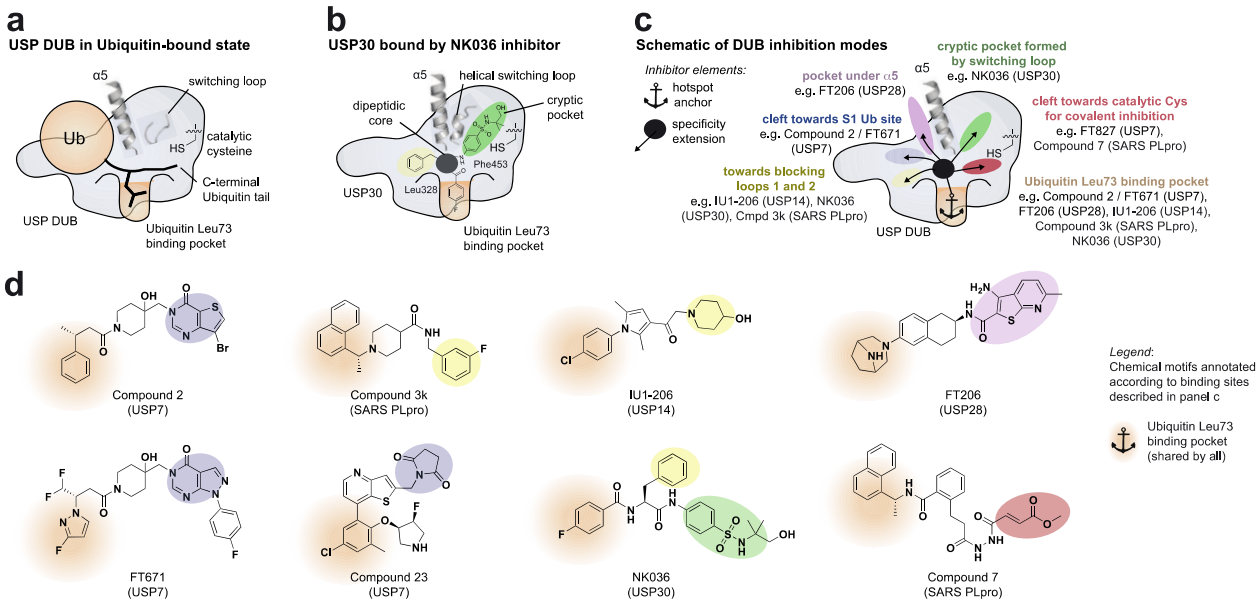

Figure 28 | A framework for specific USP DUB inhibition

a, Schematic of a Ubiquitin-bound USP DUB. Structural elements are labeled. **b,** Schematic of USP30 in complex with an inhibitor of the benzenesulfonamide scaffold, occupying the Ubiquitin Leu73 pocket (sand), the cryptic pocket (green) and the cleft towards the S1 Ubiquitin binding site (blue) with shown chemical moieties. **c,** Schematic of DUB inhibition with compounds being composed of a hotspot anchor element (occupying the Ubiquitin Leu73 pocket) and one or two specificity extensions (occupying the shown other USP DUB structural elements). Compounds featuring the respective extensions are named together with their cognate DUBs (*45*, *50*, *51*, *55*, *95*, *99*, *100*). See Fig. 27 for structural superpositions focused on the Leu73 binding pocket. **d,** Chemical structures of specific DUB inhibitors. Chemical motifs occupying the distinct binding sites are colored according to panel c. The hotspot anchor motifs shared by all are highlighted.

2.9. Outlook

The work presented in this dissertation sets the foundations for an advanced chimeric protein engineering strategy to facilitate USP30 crystallization in complex with inhibitors. Having characterized the non-covalent mode of USP30 inhibition, the next step would be to unravel the structural basis of USP30 inhibition by covalent inhibitors, which hold significant therapeutic potential. These inhibitors are currently in clinical trials and have demonstrated efficacy in improving mitophagy defects in a Parkinson's disease mouse model (*64*). To advance this goal, the design strategy used to generate the 15 chimeric constructs profiled in this dissertation could be expanded to facilitate USP30 crystallization with covalent inhibitors. In an initial crystallization screening as part of this dissertation work, the USP30-CYLD chimeric construct **(Fig. 14l)** in complex with a covalent inhibitor yielded some micro-crystalline forms **(Appendix 3.2)**. This construct could be further modified to yield diffraction quality crystals by replacement of the flexible USP30 loop with an equivalent structured β-hairpin from USP35, a strategy when applied to the USP30-USP14 chimeric construct in this dissertation **(Fig. 14k)**, greatly improved the crystal forms of USP30-NK036 complex. Since the chimeric design principle presented in this dissertation is focussed on the fingers subdomain, which is a common feature of all USP DUBs, there is high potential in the application of such a chimeric engineering strategy to other USP DUBs in a generalizable manner to create a streamlined platform facilitating USP DUB-inhibitor co-crystallization.

From an inhibitor development perspective, a key next step is to optimize the design of the USP30 inhibitors Compound 39 or NK036 to make them more "drug-like". By replacing the peptidic core of these inhibitors, their pharmacological properties could be improved. Inspiration for such inhibitor development could be drawn from USP7 inhibitor development campaigns (*51*), in which

the amidic property of initial USP7 compounds was replaced with simpler non-amidic linkages, such as ether linked morpholine in Compound 23 **(Fig. 27b)**. Even better designs were made in this campaign by introducing carbon-linked morpholine that improved the pharmacokinetic properties of USP7 compounds. Similar scaffold modifications for USP30 inhibitors could be guided by the valuable structural insights obtained from the crystal structure of USP30-NK036 complex solved in this dissertation.

This structure underscores the critical role of the benzenesulfonamide and fluorophenyl moieties of NK036 in forming key interactions with USP30 **(Fig. 19e-h)**, explaining the basis of high potency of this compound class. So, further SAR-based development of USP30 inhibitors could be focussed on replacing the peptidic scaffold with other simpler non-amidic linkages, while preserving these crucial chemical moieties around the scaffold. Additionally, the structure indicates that the binding pocket of the NK036 central phenyl ring could accommodate bulkier groups **(Fig. 19g)**. This observation aligns with previous SAR-based designs (*66*) of USP30 inhibitors that retained high potency even with sterically demanding groups in this region. Thus, this site can be exploited to introduce various groups for fine-tuning the properties of USP30 inhibitors developed using scaffold hopping approach.

Overall, the work in this dissertation provides a comprehensive protein engineering, biochemical, biophysical and structural biology framework to facilitate a generalizable application of the chimeric design principle to other USP DUBs. Moreover, the structure of USP30-inhibitor solved in this work provides valuable information that would guide the rational development of next-generation USP30 inhibitors, further underscoring the significance of structural information in inhibitor development.

3. Appendix

3.1. Protein sequence design for chimeric engineering

Construct c1 – USP30Δ

boundaries: **64-178; GSGS; 217-357; SNA; 432-502**

mutations: **F348D, M350S, I353E**

KGLVPGLVNLGNTCFMNSLLQGLSACPAFIRWLEEFTSQYSRDQKEPPSHQYLSLTLLHL
LKALSCQEVTDDEVLDASCLLDVLRMYRWQISSFEEQDAHELFHVITSSLEDERDGSGS
HWKSQHPFHGRLTSNMVCKHCEHQSPVRFDTFDSLSLSIPAATWGHPLTLDHCLHHFIS
SESVRDVVCDNCTKIEAKGTLNGEKVEHQRTTFVKQLKLGKLPQCLCIHLQRLSWSSHG
TPLKRHEHVQFNE**D**L**S**MD**E**YKYHSNASTYLFRLMAVVVHHGDMHSGHFVTYRRSPPS
ARNPLSTSNQWLWVSDDTVRKASLQEVLSSSAYLLFYERV

Construct ch1 – USP30 (USP7)

boundaries: **64-178; GSGS; 217-225 (326-348) 249-275 (370-398) 318-357; SNA; 432-502**

mutations: **F348D, M350S, I353E**

KGLVPGLVNLGNTCFMNSLLQGLSACPAFIRWLEEFTSQYSRDQKEPPSHQYLSLTLLHL
LKALSCQEVTDDEVLDASCLLDVLRMYRWQISSFEEQDAHELFHVITSSLEDERDGSGS
HWKSQHPFHGKMVSYIQCKEVDYRSDRREDYYDSLSLSIPAATWGHPLTLDHCLHHFIS
VEQLDGDNKYDAGEHGLQEAEKGVKFLTLPQCLCIHLQRLSWSSHGTPLKRHEHVQFN
E**D**L**S**MD**E**YKYHSNASTYLFRLMAVVVHHGDMHSGHFVTYRRSPPSARNPLSTSNQWL
WVSDDTVRKASLQEVLSSSAYLLFYERV

Construct ch2 – USP30 (USP14)

boundaries: **64-178; GSGS; 217-224 (248-272) 249-275 (295-320) 318-357; SNA; 432-502**

mutations: **F348D, M350S, I353E**

KGLVPGLVNLGNTCFMNSLLQGLSACPAFIRWLEEFTSQYSRDQKEPPSHQYLSLTLLHL
LKALSCQEVTDDEVLDASCLLDVLRMYRWQISSFEEQDAHELFHVITSSLEDERDGSGS
HWKSQHPFGVEFETTMKCTESEEEEVTKGKENQDSLSLSIPAATWGHPLTLDHCLHHFIS
QEEITKQSPTLQRNALYIKSSKISRLPQCLCIHLQRLSWSSHGTPLKRHEHVQFNE**D**L**S**MD
EYKYHSNASTYLFRLMAVVVHHGDMHSGHFVTYRRSPPSARNPLSTSNQWLWVSDDT
VRKASLQEVLSSSAYLLFYERV

Construct ch3 – USP30 (USP14) [USP35]

boundaries: **64-178; GSGS; 217-224 (248-272) 249-275 (295-320) 318-348 [833-845] 437-502**

mutations: **F348D**

KGLVPGLVNLGNTCFMNSLLQGLSACPAFIRWLEEFTSQYSRDQKEPPSHQYLSLTLLHL
LKALSCQEVTDDEVLDASCLLDVLRMYRWQISSFEEQDAHELFHVITSSLEDERDGSGS
HWKSQHPFGVEFETTMKCTESEEEEVTKGKENQDSLSLSIPAATWGHPLTLDHCLHHFIS
QEEITKQSPTLQRNALYIKSSKISRLPQCLCIHLQRLSWSSHGTPLKRHEHVQFNE**D**LRLP
LAGGRGQAYRLMAVVVHHGDMHSGHFVTYRRSPPSARNPLSTSNQWLWVSDDTVRK
ASLQEVLSSSAYLLFYERV

Construct ch4 – USP30 (CYLD)

boundaries: **64-178; GSGS; 217-225 (700-713) 250-275 (742-746) 317-357; SNA; 432-502**

mutations: **F348D, M350S, I353E**

KGLVPGLVNLGNTCFMNSLLQGLSACPAFIRWLEEFTSQYSRDQKEPPSHQYLSLTLLHL
LKALSCQEVTDDEVLDASCLLDVLRMYRWQISSFEEQDAHELFHVITSSLEDERDGSGS
HWKSQHPFHLKIRSAGQKVQDCYSLSLSIPAATWGHPLTLDHCLHHFISNLKFALPQCLC
IHLQRLSWSSHGTPLKRHEHVQFNE**D**L**S**MD**E**YKYHSNASTYLFRLMAVVVHHGDMHS
GHFVTYRRSPPSARNPLSTSNQWLWVSDDTVRKASLQEVLSSSAYLLFYERV

Construct c2 – USP30 (GS)

boundaries: **64-178; GSGS; 217-225; GSGS; 250-276; GSGSGS; 317-357; SNA; 432-502**

mutations: **F348D, M350S, I353E**

KGLVPGLVNLGNTCFMNSLLQGLSACPAFIRWLEEFTSQYSRDQKEPPSHQYLSLTLLHL
LKALSCQEVTDDEVLDASCLLDVLRMYRWQISSFEEQDAHELFHVITSSLEDERDGSGS
HWKSQHPFHGSGSSLSLSIPAATWGHPLTLDHCLHHFISGSGSGSLPQCLCIHLQRLSWSS
HGTPLKRHEHVQFNE**D**L**S**MD**E**YKYHSNASTYLFRLMAVVVHHGDMHSGHFVTYRRSP
PSARNPLSTSNQWLWVSDDTVRKASLQEVLSSSAYLLFYERV

3.2. Overview of all constructs designed and tested

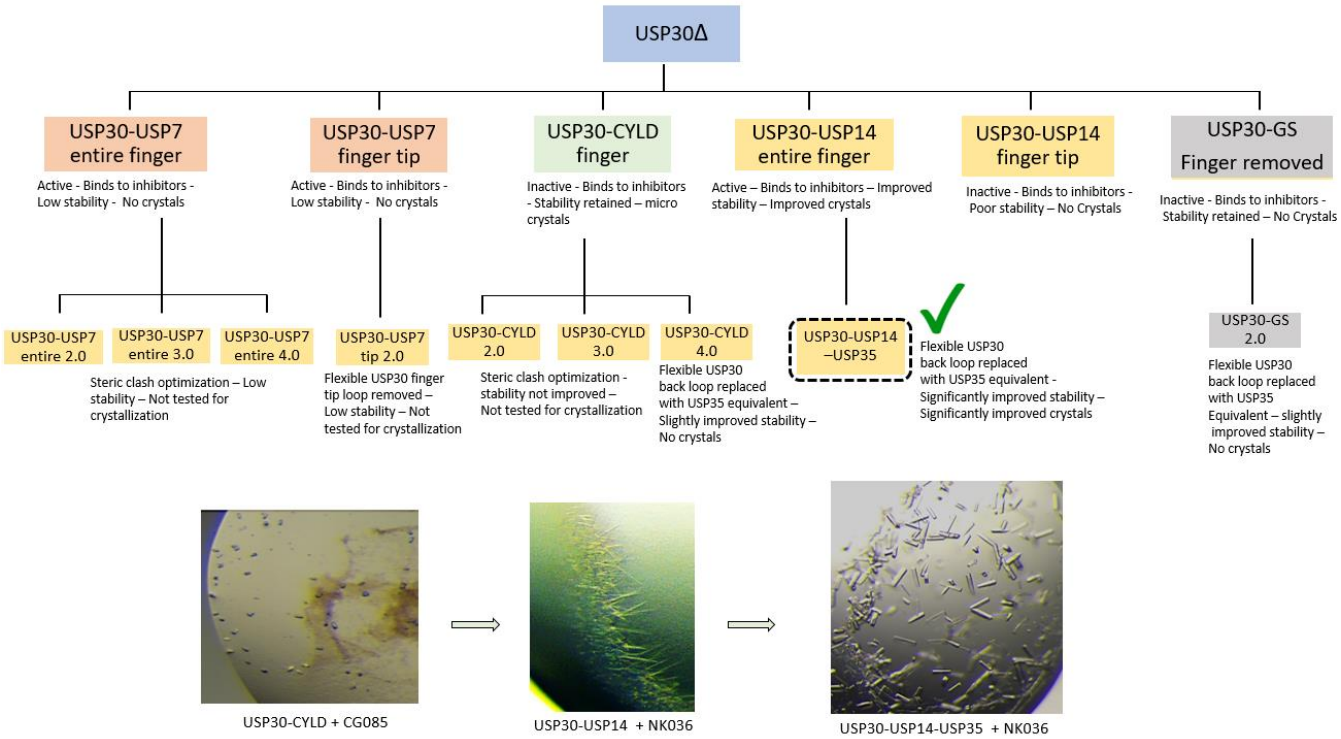

3.3. USP7 vs USP14 finger subdomain: switch from no crystals to crystals

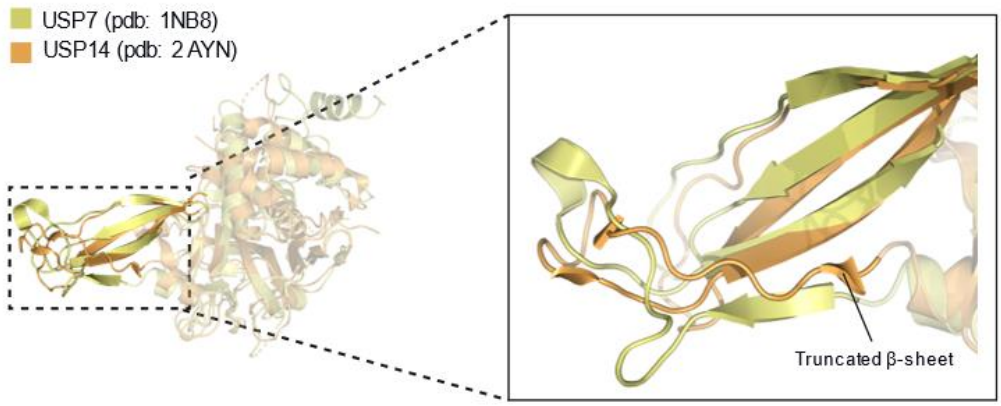

3.4. Multi-crystal averaging

Table 4. Statistics of individual datasets used for multi-crystal averaging.

	USP30 + NK036 (crystal 1)	**USP30 + NK036 (crystal 2)**	**USP30 + NK036 (crystal 3)**	**USP30 + NK036 (blended from crystals 1+2+3)**
Data collection				
Beamline	ESRF ID30A-3	ESRF ID30A-3	ESRF ID30A-3	ESRF ID30A-3
Wavelength	0.9677 Å	0.9677 Å	0.9677 Å	0.9677 Å
Space group	$P\,2_1\,2\,2_1$	$P\,2_1\,2\,2_1$	$P\,2_1\,2\,2_1$	$P\,2_1\,2\,2_1$
Cell dimensions				
a, *b*, *c* (Å)	55.90, 73.64, 201.66	55.96, 73.15, 200.37	55.92, 74.14, 201.67	55.83, 73.84, 201.05
α, β, γ (°)	90, 90, 90	90, 90, 90	90, 90, 90	90, 90, 90
Anisotropy correction	yes	yes	yes	yes
Observed reflections	59,699	49,129	62,471	214,419
Unique reflections	12,735	11,139	12,592	15,438
Resolution (Å)	48.89 – 2.95 (3.23 – 2.95)	68.71 – 3.03 (3.37 – 3.03)	53.89 – 3.01 (3.31 – 3.01)	59.52 – 2.75 (3.23 – 2.75)
Ellipsoidal resolution limits (Å) [direction]	2.95 [a*] 3.81 [b*] 2.95 [c*]	2.97 [a*] 3.67 [b*] 3.28 [c*]	2.95 [a*] 3.84 [b*] 3.01 [c*]	2.89 [a*] 3.53 [b*] 2.75 [c*]
R_{merge}	0.131 (1.274)	0.120 (0.729)	0.134 (1.079)	0.166 (1.536)
R_{meas}	0.147 (1.397)	0.137 (0.888)	0.150 (1.193)	0.173 (1.595)
$I/\sigma(I)$	7.2 (1.4)	6.6 (1.7)	7.3 (1.4)	9.6 (1.9)
$CC_{1/2}$	0.955 (0.611)	0.997 (0.526)	0.959 (0.631)	0.998 (0.730)
Spherical completeness (%)	69.7 (20.2)	66.8 (14.9)	72.8 (25.6)	68.7 (26.2)
Ellipsoidal completeness (%)	89.3 (56.6)	85.2 (48.8)	90.7 (62.1)	91.9 (69.0)
Redundancy	4.7 (5.4)	4.4 (3.2)	5.0 (5.6)	13.9 (13.9)
Wilson *B* ($Å^2$) [direction]	85 [a*] 166 [b*] 77 [c*]	84 [a*] 177 [b*] 56 [c*]	77 [a*] 158 [b*] 70 [c*]	82 [a*] 161 [b*] 71 [c*]

3.5. Comparison of covalent and non-covalent mode of inhibition of USP30

Two structures of USP30 in complex with covalent inhibitors are available through the protein data bank. These were determined with a previously reported construct, which was stabilized through a custom antibody fragment. However, due to the lack of an associated manuscript, accessory information e.g. on the antibody, validation of the binding mode or compound specificity are lacking. We carried out a comparison of the binding modes of covalent and non-covalent USP30 inhibitors **(Fig. 29a-h)**. Importantly, both binding modes are drastically different, with unique conformational changes of the switching loop associated with both. This comparison shows that both binding modes are very distinct, and the obtained data are thus highly complementary.

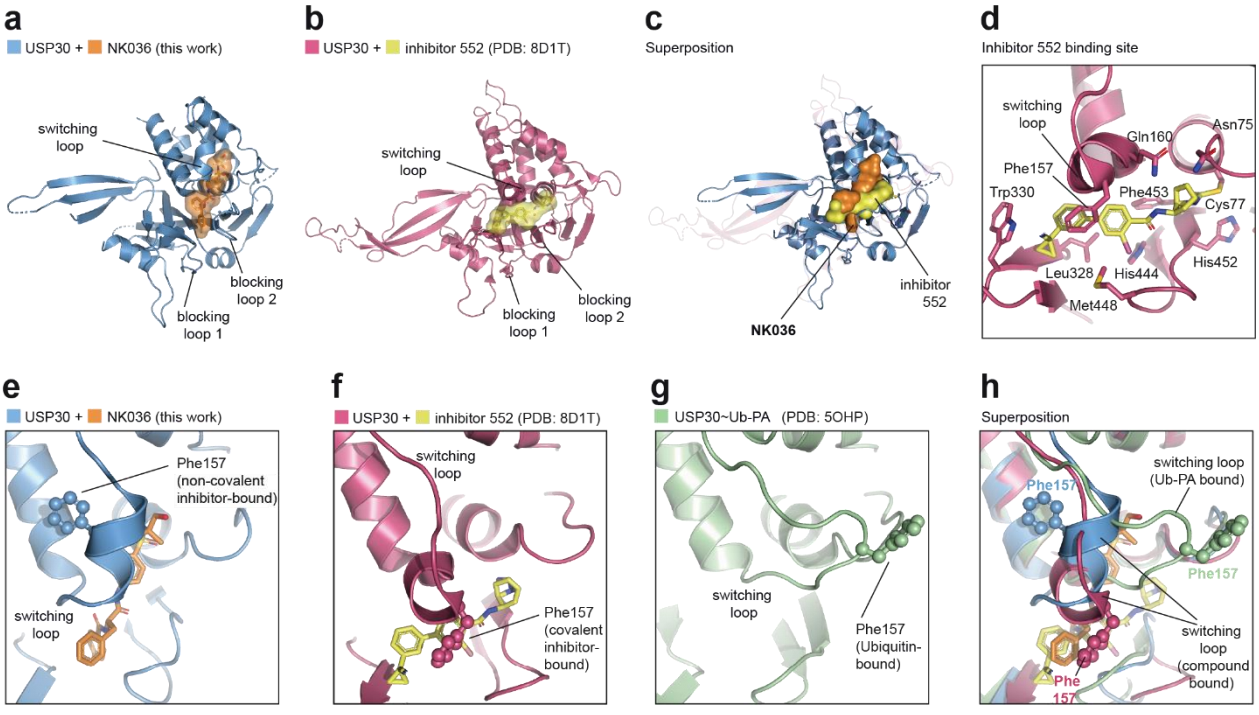

Figure 29 | Comparison of binding modes of covalent and non-covalent USP30 inhibitors
a-b, Cartoon representations of the crystal structures of USP30 in complex with non-covalent inhibitor NK036 and covalent inhibitor 552. The fragment antigen-binding region (Fab) present in the structure 8D1T is not shown. **c,** Superposition of the structure of USP30+NK036 on the structure of USP30~inhibitor 552.

d, Close-up view of the inhibitor 552 binding site highlighting key residues. The chemical structure of inhibitor 552 is shown in Extended Data Fig. 1. **e-h,** Close-up views of the conformational changes of the switching loop in the structures of USP30+NK036, USP30~inhibitor 552 and USP30~Ub-PA. Highlighted are different orientations of the switching loop residue Phe157 in the respective structures. Upon binding of the non-covalent compound, Phe157 moves backwards leading to the formation of the cryptic pocket. In contrast, upon binding of the covalent compounds, Phe157 moves forward which creates a shielded tunnel between the modified catalytic cysteine and the S1 Ubiquitin site.

3.6. Profiling of a covalent USP30 inhibitor

A Mission Therapeutics patent (*106*) revealed a class of N-cyanopyrrolidines as effective covalent inhibitors of USP30. With two related compounds in clinical trials addressing the role of USP30 in acute kidney injury (*65*), structurally characterizing these compounds is of high interest.

To this end, Gian-Marvin Kipka (Gersch group, CGC) synthesized a highly potent USP30 inhibitor, GK287. I profiled the binding of GK287 to the chimeric USP30 construct USP30^{ch3}, which was generated and characterized, and yielded a crystal structure in complex with a non-covalent inhibitor, as presented in this dissertation. In vitro LC-MS analysis confirmed covalent binding of GK287 to USP30^{ch3} **(Fig. 30a)**. Additionally, USP30^{ch3} exhibited higher stability in complex with GK287 as compared to the parent construct USP30^{c1} **(Fig. 30b)**, thus making this chimeric design suitable for the structural characterization of covalent inhibition as well.

To further investigate the binding mechanism of GK287, I tested the non-covalent compound resistant mutants of USP30^{ch3}: F453Y and L328F against GK287 **(Fig. 30c)**. The L328F mutant showed significant loss in GK287 binding, while the F453Y mutant retained GK287 binding. This suggests that GK287 follows a distinct binding mechanism as compared to the non-covalent compound NK036, likely engaging a pocket guarded by Leu328 and extending directly towards the catalytic Cys, bypassing the gatekeeper Phe453. This is in line with the observation from the

previously solved (unpublished) crystal structure of USP30 in complex with a covalent inhibitor 552 **(Fig. 29c-d)**.

Having obtained promising assay data, I then set up preliminary crystallization trials of $USP30^{ch3}$ in complex with GK287. I also included the highly truncated $USP30^{c2}$ **(Fig. 14h)** and a modified form of $USP30^{ch4}$ chimera **(Fig. 14l)** which has the flexible loop of USP30 replaced with an equivalent structured β hairpin from USP35 **(Fig. 14k)**. Putative crystal forms were obtained for the $USP30^{ch3}$~GK287 and the $USP30^{ch4}$-USP35~GK287 complexes. This is a promising first trial for further crystallization condition screening and refinement.

The study in this section demonstrates that such a chimeric design principle has the potential to be applied for profiling different modes of USP30 inhibition and possibly more broadly could be applied to other USP DUBs.

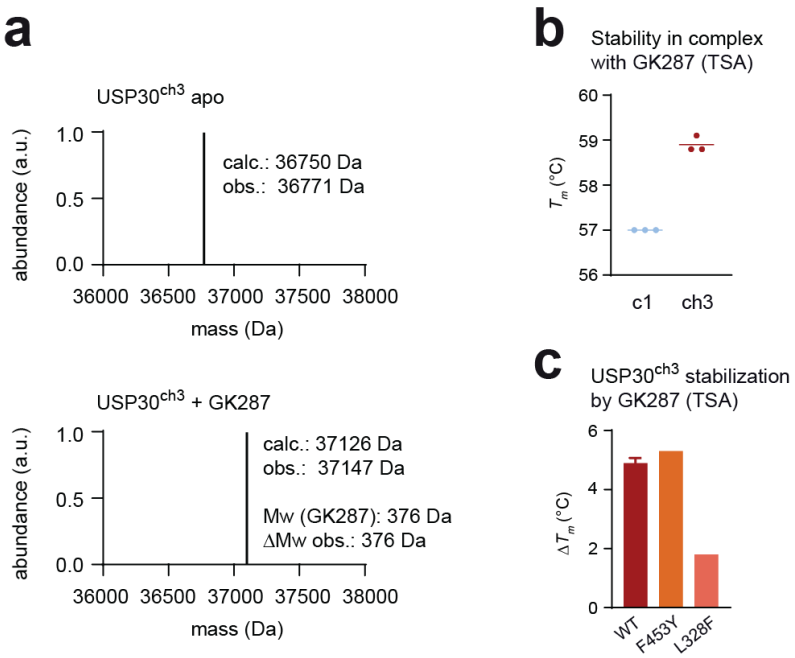

Figure 30 | Characterization of a covalent USP30 compound GK287

a, Intact protein mass spectrometry revealing covalent binding of GK287 to USP30^{ch3}. USP30^{ch3} (2.5 µM) was treated with GK287 (10 µM) for 2 h. **b,** Protein stability of indicated USP30 constructs in the presence of 20 µM GK287. **c,** Protein stability of indicated USP30 proteins in the presence of 20 µM GK287. ΔT_m was calculated as T_m of the compound-bound sample subtracted from T_m of the respective apo protein. Mean ± s.d. (N=3).

4. Methods

4.1. Cloning and protein expression

Chimeric USP30 constructs for bacterial expression were generated by amplifying protein-coding part from plasmids or by incorporating sequences as overhangs into primers. The following sequences were used: Codon-optimized human USP30 catalytic domain, Addgene #110746, uniprot: Q70CQ3 with modifications described previously (*71*) and in the Supplementary Materials; human USP7, uniprot: Q93009; human USP14, uniprot: P54578; human USP35, uniprot: Q9P2H5; human CYLD, uniprot: Q9NQC7. All protein sequences are shown in the Supplementary Materials. DNA fragments were joined through SOE-PCR and subsequently ligated into the pOPINK vector using the In-Fusion HD Cloning Kit (Takara Clonetech). A pOPINE vector containing C-terminally Flag-tagged human USP30 (1-517) was used for transient transfection as described previously (*71*). Point mutants were introduced through vector QuikChange PCR. Constructs were confirmed by Sanger sequencing.

Bacterial expression was performed in Rosetta2(DE3) pLacI cells. An overnight culture was diluted 1:100 in 2xTY medium supplemented with appropriate antibiotics. Cultures were grown at 30°C with shaking at 180 rpm until an optical density (OD600) of 0.8-1.0 was reached. After cooling to 18°C, protein expression was induced by addition of isopropyl β-D-thiogalactopyranoside (IPTG) to a final concentration of 0.5 mM and cells were kept shaking at 18°C for 18 h. Harvested bacterial cells were stored at -80°C.

4.2. Protein purification

Cells were resuspended in lysis buffer (50 mM sodium phosphate pH 8.0, 300 mM NaCl, 20 mM imidazole, 4 mM β-mercaptoethanol) supplemented with DNAseI and lysozyme. The cell suspension was lysed by sonication (55% amplitude, 10 s on/10 s off) on ice, cleared by centrifugation at 33,500xg for 30 min at 4°C and filtered through a 0.45 µm filter.

All purification steps were performed on Äkta Pure systems (GE Healthcare) at 4°C. For affinity chromatography, lysate was loaded onto a pre-equilibrated 5 mL HisTrap fast flow column (GE Healthcare), washed with 20 column volumes (CV) of lysis buffer and then eluted with a linear gradient of 3.5 CV into elution buffer (50 mM sodium phosphate pH 8.0, 300 mM NaCl, 500 mM imidazole, 4 mM β-mercaptoethanol). Protein-containing fractions were pooled, supplemented with His6-tagged 3C protease and dialyzed against 25 mM Tris pH 8.5, 100 mM NaCl, 4 mM DTT overnight at 4°C. The dialyzed sample was diluted two-fold with 20 mM Tris pH 8.5, filtered through a 0.45 µm filter, and directly loaded onto a 6 mL Resource Q column, equilibrated with 25 mM Tris pH 8.5, 50 mM NaCl, 4 mM DTT, for anion exchange chromatography. Elution was achieved with a gradient into high salt buffer (25 mM Tris pH 8.5, 500 mM NaCl, 4 mM DTT). Further purification was carried out on a HiLoad 16/600 Superdex 75 pg column in 20 mM Tris pH 8.0, 100 mM NaCl, 4 mM DTT for samples used for crystallography. Purity of peak fractions was assessed by SDS-PAGE before pooling, concentrating at 4°C/3200xg in spin concentrators (10 kDa MWCO, Amicon) and flash freezing in liquid nitrogen. Protein concentrations were determined on a Nanodrop (Thermo Fisher).

4.3. Construct design and modelling

Protein construct design was guided by the annotation of USP domain boxes (*25*) and available crystal structures of human USP DUBs including those of USP30 (*71, 107*), USP7 (*38, 50, 93, 94*), USP14 (*39, 45*), USP35 (*108*) and CYLD (*109*) (Supplementary Table 1). Chimeric USP30 protein sequences were based on the sequence used for PDB entry 5OHK (*71*). Structures of chimeric sequences were predicted with AlphaFold2 (*110*) and analyzed with PyMOL, and proteins were experimentally prepared and biochemically characterized in an iterative process.

4.4. Crystallization

Protein samples for crystallization were prepared by mixing USP30 (30 mg/mL in gel filtration buffer) with 1.4 equivalents of NK036 which was added in two steps from a 100 mM DMSO stock. Following incubation for 30 min at room temperature, the sample was passed through a Proteus mini clarification spin column (Protein Ark) and used directly for crystallization trials. Screening plates were set up by a mosquito HTS robot (TTP Labtech) in 96 well sitting-drop vapor diffusion plates in MRC format (Molecular Dimensions) and incubated at 20°C. Drop ratios of 200 nL + 200 nL and 500 nL + 500 nL were used for coarse screening and fine screening, respectively.

Initial crystals of USP30 construct ch3 in complex with NK036 were found in 0.1 M Bicine pH 9.0, 5% (w/v) PEG 20,000, 1% (v/v) dioxane. Moderately sized cylindrical crystals (60 x 16 x 16 µm3) were obtained through fine screening in 88 mM NaOH, 100 mM Bicine, 11% (w/v) PEG 20,000, 1% (v/v) dioxane.

Crystal size and diffraction quality were further improved through the Hampton additive screen on the above-mentioned condition. Larger cylindrical crystals (130 x 25 x 25 µm3) of diffraction quality were obtained in 76 mM NaOH, 100 mM Bicine, 10.2% (w/v) PEG 20,000, 1% (v/v) dioxane, 10 mM L-proline (Crystal 1) and 85 mM NaOH, 100 mM Bicine, 10.2% (w/v) PEG 20,000, 1% (v/v) dioxane, 10 mM L-proline (Crystal 2) and 88 mM NaOH, 100 mM Bicine, 11% (w/v) PEG 20,000, 1% (v/v) dioxane, 10 mM sarcosine (Crystal 3). Crystals were soaked in mother liquor supplemented with 25% (v/v) glycerol (Crystals 1 and 2) or ethylene glycol (Crystal 3) before vitrification in liquid nitrogen.

The covalent Ubiquitin complex was obtained by mixing USP30 after ResQ purification with 1.2 equivalents of Ub-PA. Following incubation at room temperature for 2 hours, USP30~Ub-PA was purified on a HiLoad 16/600 Superdex 75 pg column as described above and concentrated to 12 mg/mL. Diffraction-quality crystals were obtained from coarse screening plates in 0.56 M sodium citrate pH 7.0. Crystals were soaked in mother liquor supplemented with 25% (v/v) ethylene glycol before vitrification in liquid nitrogen.

4.5. Data collection, structure solution and refinement

Diffraction data were collected at 100 K at the European Synchrotron Radiation Facility (ESRF) on beamline ID30A-3. Datasets from different crystals of the USP30-NK036 complex were separately integrated with DIALS (*111*). Multi-crystal data averaging was employed as implemented in CCP4 blend (*112*) to improve resolution, lower B-factors and ultimately enhance features in the electron density. Multiple datasets and combinations were explored, resulting in the chosen data averaged from crystals 1-3 as the best cluster. The final combined data was then

corrected for anisotropy by the Staraniso webserver (*113*). Table 1 displays data collection and refinement statistics, and data for anisotropically scaled individual datasets are provided in Supplementary Table 3 for comparison. The final structure was solved to a resolution of 2.75 Å from the averaged data by molecular replacement using MR Phaser (*114*) and a search model based on the Alphafold-derived structure model of the chimera. The final model was obtained by multiple cycles of structure building in Coot (*115*) and refinement with Phenix Refine (*116*). The compound geometry was optimized through ORCA (*117*) at the B3LYP/def2-SVP level of theory. Geometry restraints were generated by ELBOW (*118*).

Diffraction data leading to the USP30~Ub-PA structure were integrated with DIALS. The final structure was obtained by molecular replacement with MR Phaser and refinement with Phenix Refine as described above. Final data collection and refinement statistics are shown in Table 3.

4.6. Ub-PA labeling assay

Purified proteins were diluted in 20 mM Tris pH 8.0, 300 mM NaCl, 2 mM DTT, 5% glycerol. Protein and probe were combined at 2.5 μM and 10 μM final concentrations, respectively, and reacted for 1 h at room temperature. For the in vitro compound-probe competition assay, 1 μM protein was pre-incubated with 8 μM compound at room temperature for 2 h. Following compound incubation, 4 μM of probe was added and reacted for 1 h at 37°C. Probe binding was assessed by SDS-PAGE and Coomassie staining.

4.7. Ub-RhoG cleavage assay

Enzyme kinetics were performed in black, low-volume, non-binding surface 384 well plates. For activity assays, 2x Ub-RhoG substrate (final concentration: 50 nM) and 2x enzyme (final concentration: 0.25 nM – 32 nM) were prepared in 20 mM HEPES pH 8.0, 50 mM NaCl, 5 mM DTT, 0.1 mg/mL BSA. 10 µL of 2x enzyme solution was added in triplicates to the plate. The reaction was started by addition of 10 µL of 2x substrate solution. For enzyme inhibition assays, 2x substrate (final concentration: 100 nM), 4x enzyme (final concentration: 0.1 nM) and 4x inhibitor (final concentration: 1.6 pM – 1.6 µM) were prepared in 50 mM Tris-HCl pH 8.0, 0.05 mg/mL BSA, 4 mM DTT, 0.01% Tween 20. 4x inhibitor solution was added to 4x enzyme solution to create a 2x enzyme-inhibitor mixture. 10 µL of this 2x enzyme-inhibitor mixture was then added to the plate in triplicates and incubated at room temperature for 90 mins. The reaction was started by addition of 10 µL of 2x Ub-RhoG substrate. Substrate cleavage was monitored by measurement of cleaved RhoG fluorescence (excitation = 492 nm, emission = 525 nm) every 30 s for 1 h at 25 °C on a TECAN Spark plate reader.

4.8. Thermal shift assay

The thermal stability of USP30 constructs and effects of inhibitor/Ub-PA binding were determined by thermal shift assays. Inhibitor, Ub-PA and Sypro orange dye (Sigma, stock: 5000x in DMSO) solutions were prepared in 1x PBS, 4 mM DTT. Inhibitor/Ub-PA were pre-diluted to 100 µM and Sypro orange dye was pre-diluted to 50x (from the commercial stock). Mixtures of protein, inhibitor/Ub-PA and Sypro were prepared having inhibitor/Ub-PA at a final concentration of 20 µM, Sypro at a final concentration of 4x and protein at a final concentration of 2 µM for c1, 4 µM

for ch1, ch4 and c2 and 3 μM for ch2 and ch3. Samples were added in triplicates to a white 96-well PCR plate (Bio-Rad). Fluorescence intensity was monitored (excitation = 450-490 nm, emission = 560-580 nm) at a 20-90°C gradient (increment: 0.3 °C, hold for 5 s before read) on a Real-time PCR system (Bio-Rad).

4.9. Intact protein mass spectrometry

Purified proteins were diluted in 20 mM Tris pH 8.0, 100 mM NaCl, 2 mM DTT to a final concentration of 2.5 μM and treated with 10 μM DMSO/compound. Followed by incubation at room temperature for 1 h, 1 μg of protein was injected into an Agilent 1260 (II) infinity system and passed through a desalting cartridge prior to mass spectra recording according to a previously described method (*102*). Deconvoluted spectra were analyzed using ProMass (Enovatia).

5. References

1. N. H. Kazi, N. Klink, K. Gallant, G.-M. Kipka, M. Gersch, Chimeric deubiquitinase engineering reveals structural basis for specific inhibition of USP30 and a framework for DUB ligandability. *bioRxiv*, 2024.2009.2022.613429 (2024).
2. R. B. Damgaard, The ubiquitin system: from cell signalling to disease biology and new therapeutic opportunities. *Cell Death Differ* **28**, 423-426 (2021).
3. A. Ciechanover, The unravelling of the ubiquitin system. *Nat Rev Mol Cell Bio* **16**, 322-324 (2015).
4. M. J. Clague, S. Urbé, D. Komander, Breaking the chains: deubiquitylating enzyme specificity begets function. *Nat Rev Mol Cell Bio* **20**, 338-352 (2019).
5. B. Zhao *et al.*, Specificity of the E1-E2-E3 Enzymatic Cascade for Ubiquitin C-Terminal Sequences Identified by Phage Display. *Acs Chem Biol* **7**, 2027-2035 (2012).
6. W. Li, Y. Ye, Polyubiquitin chains: functions, structures, and mechanisms. *Cell Mol Life Sci* **65**, 2397-2406 (2008).
7. D. Komander, M. Rape, The Ubiquitin Code. *Annu Rev Biochem* **81**, 203-229 (2012).
8. J. J. Sims, R. E. Cohen, Linkage-Specific Avidity Defines the Lysine 63-Linked Polyubiquitin-Binding Preference of Rap80. *Mol Cell* **33**, 775-783 (2009).
9. Y. Sato *et al.*, Structural basis for specific recognition of Lys 63-linked polyubiquitin chains by tandem UIMs of RAP80. *Embo J* **28**, 2461-2468 (2009).
10. Y. Sato, A. Yoshikawa, M. Yamashita, A. Yamagata, S. Fukai, Structural basis for specific recognition of Lys 63-linked polyubiquitin chains by NZF domains of TAB2 and TAB3. *Embo J* **28**, 3903-3909 (2009).
11. Y. Kulathu, M. Akutsu, A. Bremm, K. Hofmann, D. Komander, Two-sided ubiquitin binding explains specificity of the TAB2 NZF domain. *Nature Structural & Molecular Biology* **16**, 1328-1330 (2009).
12. B. Skaug, X. M. Jiang, Z. J. Chen, The Role of Ubiquitin in NF-κB Regulatory Pathways. *Annual Review of Biochemistry* **78**, 769-796 (2009).
13. A. Yoshikawa *et al.*, Crystal structure of the NEMO ubiquitin-binding domain in complex with Lys 63-linked di-ubiquitin. *Febs Lett* **583**, 3317-3322 (2009).
14. S. M. B. Nijman *et al.*, A genomic and functional inventory of deubiquitinating enzymes. *Cell* **123**, 773-786 (2005).
15. U. L. Burska *et al.*, Deubiquitinating Enzyme Usp12 Is a Novel Co-activator of the Androgen Receptor. *J Biol Chem* **288**, 32641-32650 (2013).
16. T. Imamura, Y. Oshima, A. Hikita, Regulation of TGF-beta family signalling by ubiquitination and deubiquitination. *J Biochem* **154**, 481-489 (2013).
17. G. Lopez-Castejon, M. J. Edelmann, Deubiquitinases: Novel Therapeutic Targets in Immune Surveillance? *Mediators Inflamm* **2016**, 3481371 (2016).
18. Z. Gu, W. Shi, Manipulation of viral infection by deubiquitinating enzymes: new players in host-virus interactions. *Future Microbiol* **11**, 1435-1446 (2016).
19. S. K. Mungamuri *et al.*, USP7 Enforces Heterochromatinization of p53 Target Promoters by Protecting SUV39H1 from MDM2-Mediated Degradation. *Cell Rep* **14**, 2528-2537 (2016).
20. U. L. McClurg, C. N. Robson, Deubiquitinating enzymes as oncotargets. *Oncotarget* **6**, 9657-9668 (2015).

21. D. Mennerich, K. Kubaichuk, T. Kietzmann, DUBs, Hypoxia, and Cancer. *Trends Cancer* **5**, 632-653 (2019).
22. X. I. Ambroggio, D. C. Rees, R. J. Deshaies, JAMM: A metalloprotease-like zinc site in the proteasome and signalosome. *Plos Biol* **2**, 113-119 (2004).
23. A. Y. Amerik, M. Hochstrasser, Mechanism and function of deubiquitinating enzymes. *Bba-Mol Cell Res* **1695**, 189-207 (2004).
24. N. J. Schauer, R. S. Magin, X. Liu, L. M. Doherty, S. J. Buhrlage, Advances in Discovering Deubiquitinating Enzyme (DUB) Inhibitors. *J Med Chem* **63**, 2731-2750 (2020).
25. Y. Ye, H. Scheel, K. Hofmann, D. Komander, Dissection of USP catalytic domains reveals five common insertion points. *Mol Biosyst* **5**, 1797-1808 (2009).
26. T. E. T. Mevissen *et al.*, OTU Deubiquitinases Reveal Mechanisms of Linkage Specificity and Enable Ubiquitin Chain Restriction Analysis. *Cell* **154**, 169-184 (2013).
27. M. Albrecht, M. Golatta, U. Wüllner, T. Lengauer, Structural and functional analysis of ataxin-2 and ataxin-3. *Eur J Biochem* **271**, 3155-3170 (2004).
28. T. Maurer, I. E. Wertz, Length Matters: MINDY Is a New Deubiquitinase Family that Preferentially Cleaves Long Polyubiquitin Chains. *Mol Cell* **63**, 4-6 (2016).
29. D. Kwasna *et al.*, Discovery and Characterization of ZUFSP/ZUP1, a Distinct Deubiquitinase Class Important for Genome Stability. *Mol Cell* **70**, 150-+ (2018).
30. R. K. Shrestha *et al.*, Insights into the Mechanism of Deubiquitination by JAMM Deubiquitinases from Cocrystal Structures of the Enzyme with the Substrate and Product. *Biochemistry-Us* **53**, 3199-3217 (2014).
31. C. Vlasschaert, D. Cook, X. H. Xia, D. A. Gray, The Evolution and Functional Diversification of the Deubiquitinating Enzyme Superfamily. *Genome Biol Evol* **9**, 558-573 (2017).
32. J. Näsvall, L. Sun, J. R. Roth, D. I. Andersson, Real-Time Evolution of New Genes by Innovation, Amplification, and Divergence. *Science* **338**, 384-387 (2012).
33. T. Hermanns *et al.*, An evolutionary approach to systematic discovery of novel deubiquitinases, applied to. *Life Sci Alliance* **3**, (2020).
34. D. Komander, M. J. Clague, S. Urbé, Breaking the chains: structure and function of the deubiquitinases. *Nat Rev Mol Cell Bio* **10**, 550-563 (2009).
35. N. Keijzer *et al.*, Variety in the USP deubiquitinase catalytic mechanism. *Life Sci Alliance* **7**, (2024).
36. V. Quesada *et al.*, Cloning and enzymatic analysis of 22 novel human ubiquitin-specific proteases. *Biochem Bioph Res Co* **314**, 54-62 (2004).
37. M. Békés *et al.*, DUB-Resistant Ubiquitin to Survey Ubiquitination Switches in Mammalian Cells. *Cell Rep* **5**, 826-838 (2013).
38. M. Hu *et al.*, Crystal structure of a UBP-family deubiquitinating enzyme in isolation and in complex with ubiquitin aldehyde. *Cell* **111**, 1041-1054 (2002).
39. M. Hu *et al.*, Structure and mechanisms of the proteasome-associated deubiquitinating enzyme USP14. *Embo J* **24**, 3747-3756 (2005).
40. W. F. Zhang *et al.*, Contribution of Active Site Residues to Substrate Hydrolysis by USP2: Insights into Catalysis by Ubiquitin Specific Proteases. *Biochemistry-Us* **50**, 4775-4785 (2011).

41. N. J. Schauer, R. S. Magin, X. X. Liu, L. M. Doherty, S. J. Buhrlage, Advances in Discovering Deubiquitinating Enzyme (DUB) Inhibitors. *Journal of Medicinal Chemistry* **63**, 2731-2750 (2020).
42. E. J. Ruiz *et al.*, USP28 deletion and small-molecule inhibition destabilizes c-MYC and elicits regression of squamous cell lung carcinoma. *Elife* **10**, (2021).
43. F. Wang, S. Ning, B. M. Yu, Y. F. Wang, USP14: Structure, Function, and Target Inhibition. *Front Pharmacol* **12**, (2022).
44. M. Boselli *et al.*, An inhibitor of the proteasomal deubiquitinating enzyme USP14 induces tau elimination in cultured neurons. *J Biol Chem* **292**, 19209-19225 (2017).
45. Y. Wang *et al.*, Small molecule inhibitors reveal allosteric regulation of USP14 via steric blockade. *Cell Res* **28**, 1186-1194 (2018).
46. J. Shan, W. H. Zhao, W. Gu, Suppression of Cancer Cell Growth by Promoting Cyclin D1 Degradation. *Mol Cell* **36**, 469-476 (2009).
47. M. I. Davis *et al.*, Small Molecule Inhibition of the Ubiquitin-specific Protease USP2 Accelerates cyclin D1 Degradation and Leads to Cell Cycle Arrest in Colorectal Cancer and Mantle Cell Lymphoma Models. *J Biol Chem* **291**, 24628-24640 (2016).
48. M. D. Tomala *et al.*, Identification of small-molecule inhibitors of USP2a. *Eur J Med Chem* **150**, 261-267 (2018).
49. S. Bhattacharya, D. Chakraborty, M. Basu, M. K. Ghosh, Emerging insights into HAUSP (USP7) in physiology, cancer and other diseases. *Signal Transduct Tar* **3**, (2018).
50. A. P. Turnbull *et al.*, Molecular basis of USP7 inhibition by selective small-molecule inhibitors. *Nature* **550**, 481-+ (2017).
51. P. R. Leger *et al.*, Discovery of Potent, Selective, and Orally Bioavailable Inhibitors of USP7 with In Vivo Antitumor Activity. *Journal of Medicinal Chemistry* **63**, 5398-5420 (2020).
52. F. Sauer *et al.*, Differential Oligomerization of the Deubiquitinases USP25 and USP28 Regulates Their Activities. *Mol Cell* **74**, 421-+ (2019).
53. M. Gersch *et al.*, Distinct USP25 and USP28 Oligomerization States Regulate Deubiquitinating Activity. *Mol Cell* **74**, 436-+ (2019).
54. J. D. Wrigley *et al.*, Identification and Characterization of Dual Inhibitors of the USP25/28 Deubiquitinating Enzyme Subfamily. *Acs Chem Biol* **12**, 3113-3125 (2017).
55. J. V. Patzke *et al.*, Structural basis for the bi-specificity of USP25 and USP28 inhibitors. *Embo Rep* **25**, 2950-2973 (2024).
56. M. L. Rennie, C. Arkinson, V. K. Chaugule, R. Toth, H. Walden, Structural basis of FANCD2 deubiquitination by USP1-UAF1. *Nature Structural & Molecular Biology* **28**, 356-+ (2021).
57. Q. Liang *et al.*, A selective USP1-UAF1 inhibitor links deubiquitination to DNA damage responses. *Nat Chem Biol* **10**, 298-+ (2014).
58. M. L. Rennie, C. Arkinson, V. K. Chaugule, H. Walden, Cryo-EM reveals a mechanism of USP1 inhibition through a cryptic binding site. *Sci Adv* **8**, (2022).
59. L. Cadzow *et al.*, The USP1 Inhibitor KSQ-4279 Overcomes PARP Inhibitor Resistance in Homologous Recombination-Deficient Tumors. *Cancer Res* **84**, 3419-3434 (2024).
60. N. Nakamura, S. Hirose, Regulation of mitochondrial morphology by USP30, a deubiquitinating enzyme present in the mitochondrial outer membrane. *Mol Biol Cell* **19**, 1903-1911 (2008).

61. S. M. Jin *et al.*, Mitochondrial membrane potential regulates PINK1 import and proteolytic destabilization by PARL. *J Cell Biol* **191**, 933-942 (2010).
62. D. P. Narendra *et al.*, PINK1 Is Selectively Stabilized on Impaired Mitochondria to Activate Parkin. *Plos Biol* **8**, (2010).
63. B. Bingol *et al.*, The mitochondrial deubiquitinase USP30 opposes parkin-mediated mitophagy. *Nature* **510**, 370-+ (2014).
64. T. S. Z. Fang *et al.*, Knockout or inhibition of USP30 protects dopaminergic neurons in a Parkinson's disease mouse model. *Nat Commun* **14**, (2023).
65. A. Agarwal *et al.*, Cellular and Molecular Mechanisms of AKI. *J Am Soc Nephrol* **27**, 1288-1299 (2016).
66. A. F. Kluge *et al.*, Novel highly selective inhibitors of ubiquitin specific protease 30 (USP30) accelerate mitophagy. *Bioorg Med Chem Lett* **28**, 2655-2659 (2018).
67. A. Clancy *et al.*, The deubiquitylase USP9X controls ribosomal stalling (vol 220, e202004211, 2021). *J Cell Biol* **220**, (2021).
68. J. Yi *et al.*, Spautin-1 promotes PINK1-PRKN-dependent mitophagy and improves associative learning capability in an alzheimer disease animal model. *Autophagy* **20**, 2655-2676 (2024).
69. W. C. Chan *et al.*, Accelerating inhibitor discovery for deubiquitinating enzymes. *Nat Commun* **14**, (2023).
70. S. M. Lange, L. A. Armstrong, Y. Kulathu, Deubiquitinases: From mechanisms to their inhibition by small molecules. *Mol Cell* **82**, 15-29 (2022).
71. M. Gersch *et al.*, Mechanism and regulation of the Lys6-selective deubiquitinase USP30. *Nature Structural & Molecular Biology* **24**, 920-+ (2017).
72. T. Wauer *et al.*, Ubiquitin Ser65 phosphorylation affects ubiquitin structure, chain assembly and hydrolysis. *Embo J* **34**, 307-325 (2015).
73. L. Gu *et al.*, The IKKβ-USP30-ACLY Axis Controls Lipogenesis and Tumorigenesis. *Hepatology* **73**, 160-174 (2021).
74. F. Wang *et al.*, USP30: Structure, Emerging Physiological Role, and Target Inhibition. *Front Pharmacol* **13**, (2022).
75. K. Kobayashi *et al.*, Involvement of PARK2-Mediated Mitophagy in Idiopathic Pulmonary Fibrosis Pathogenesis. *J Immunol* **197**, 504-516 (2016).
76. E. Marcassa *et al.*, Dual role of USP30 in controlling basal pexophagy and mitophagy. *Embo Rep* **19**, (2018).
77. V. Riccio *et al.*, Deubiquitinating enzyme USP30 maintains basal peroxisome abundance by regulating pexophagy. *J Cell Biol* **218**, 798-807 (2019).
78. S. Bandres-Ciga, M. Diez-Fairen, J. J. Kim, A. B. Singleton, Genetics of Parkinson's disease: An introspection of its journey towards precision medicine. *Neurobiol Dis* **137**, (2020).
79. M. Saito *et al.*, Autosomal recessive juvenile parkinsonism. *Brain Dev-Jpn* **22**, S115-S117 (2000).
80. A. M. Pickrell, R. J. Youle, The Roles of PINK1, Parkin, and Mitochondrial Fidelity in Parkinson's Disease. *Neuron* **85**, 257-273 (2015).
81. C. N. Cunningham *et al.*, USP30 and parkin homeostatically regulate atypical ubiquitin chains on mitochondria. *Nat Cell Biol* **17**, 160-+ (2015).
82. A. Ordureau *et al.*, Global Landscape and Dynamics of Parkin and USP30-Dependent Ubiquitylomes in iNeurons during Mitophagic Signaling. *Mol Cell* **77**, 1124-+ (2020).

83. Y. Q. Wang *et al.*, Deubiquitinating enzymes regulate PARK2-mediated mitophagy. *Autophagy* **11**, 595-606 (2015).
84. A. Sanchez-Martinez, A. Martinez, A. J. Whitworth, FBXO7/ntc and USP30 antagonistically set the ubiquitination threshold for basal mitophagy and provide a target for Pink1 phosphorylation in vivo. *Plos Biol* **21**, (2023).
85. L. Phu *et al.*, Dynamic Regulation of Mitochondrial Import by the Ubiquitin System. *Mol Cell* **77**, 1107-+ (2020).
86. W. Yue *et al.*, A small natural molecule promotes mitochondrial fusion through inhibition of the deubiquitinase USP30. *Cell Research* **24**, 482-496 (2014).
87. J. Okarmus *et al.*, USP30 inhibition induces mitophagy and reduces oxidative stress in parkin-deficient human neurons. *Cell Death Dis* **15**, (2024).
88. S. Miller, M. M. K. Muqit, Therapeutic approaches to enhance PINK1/Parkin mediated mitophagy for the treatment of Parkinson's disease. *Neurosci Lett* **705**, 7-13 (2019).
89. E. V. Rusilowicz-Jones *et al.*, Benchmarking a highly selective USP30 inhibitor for enhancement of mitophagy and pexophagy. *Life Sci Alliance* **5**, (2022).
90. E. V. Rusilowicz-Jones *et al.*, USP30 sets a trigger threshold for PINK1-PARKIN amplification of mitochondrial ubiquitylation. *Life Sci Alliance* **3**, (2020).
91. D. P. O'Brien *et al.*, Structural Premise of Selective Deubiquitinase USP30 Inhibition by Small-Molecule Benzosulfonamides. *Mol Cell Proteomics* **22**, (2023).
92. H. K. Luo, J. Krigman, R. H. Zhang, M. C. Yang, N. Sun, Pharmacological inhibition of USP30 activates tissue-specific mitophagy. *Acta Physiol* **232**, (2021).
93. L. Kategaya *et al.*, USP7 small-molecule inhibitors interfere with ubiquitin binding. *Nature* **550**, 534-+ (2017).
94. I. Lamberto *et al.*, Structure-Guided Development of a Potent and Selective Non-covalent Active-Site Inhibitor of USP7. *Cell Chem Biol* **24**, 1490-+ (2017).
95. G. Gavory *et al.*, Discovery and characterization of highly potent and selective allosteric USP7 inhibitors. *Nat Chem Biol* **14**, 118-+ (2018).
96. D. Romero, L., Johnson, M., Garrett, Lee, A., David, Behrouz, B. & Fritzen Jr., E., Lawrence. . (2021), vol. WO/2021/050992.
97. M. W. Zhang, J. M. Berk, A. B. Mehrtash, J. Kanyo, M. Hochstrasser, A versatile new tool derived from a bacterial deubiquitylase to detect and purify ubiquitylated substrates and their interacting proteins. *Plos Biol* **20**, (2022).
98. K. Wendrich *et al.*, Discovery and mechanism of K63-linkage-directed deubiquitinase activity in USP53. *Nat Chem Biol*, (2024).
99. D. Zhou *et al.*, Structure-based discovery of potent USP28 inhibitors derived from Vismodegib. *Eur J Med Chem* **254**, (2023).
100. Y. M. Báez-Santos *et al.*, X-ray Structural and Biological Evaluation of a Series of Potent and Highly Selective Inhibitors of Human Coronavirus Papain-like Proteases. *Journal of Medicinal Chemistry* **57**, 2393-2412 (2014).
101. B. C. Sanders *et al.*, Potent and selective covalent inhibition of the papain-like protease from SARS-CoV-2. *Nat Commun* **14**, (2023).
102. C. Grethe *et al.*, Structural basis for specific inhibition of the deubiquitinase UCHL1. *Nat Commun* **13**, (2022).
103. M. Clerici, M. P. A. Luna-Vargas, A. C. Faesen, T. K. Sixma, The DUSP-Ubl domain of USP4 enhances its catalytic efficiency by promoting ubiquitin exchange. *Nat Commun* **5**, (2014).

104. S. K. Maurer *et al.*, Ubiquitin-specific protease 11 structure in complex with an engineered substrate mimetic reveals a molecular feature for deubiquitination selectivity. *J Biol Chem* **299**, (2023).
105. P. Paudel *et al.*, Crystal structure and activity-based labeling reveal the mechanisms for linkage-specific substrate recognition by deubiquitinase USP9X. *Proc. Natl. Acad. Sci. U. S. A.* **116**, 7288-7297 (2019).
106. C. A. L. Mark Ian Kemp, Paul William Thompson, M. Therapeutics, Ed. (2021).
107. Y. Sato *et al.*, Structural basis for specific cleavage of Lys6-linked polyubiquitin chains by USP30. *Nature Structural & Molecular Biology* **24**, 911-+ (2017).
108. P. Leznicki *et al.*, Expansion of DUB functionality generated by alternative isoforms-USP35, a case study. *J Cell Sci* **131**, (2018).
109. D. Komander *et al.*, The structure of the CYLD USP domain explains its specificity for Lys63-linked polyubiquitin and reveals a B box module. *Mol Cell* **29**, 451-464 (2008).
110. J. Jumper *et al.*, Highly accurate protein structure prediction with AlphaFold. *Nature* **596**, 583-+ (2021).
111. G. Winter *et al.*: implementation and evaluation of a new integration package. *Acta Crystallogr D* **74**, 85-97 (2018).
112. J. Foadi *et al.*, Clustering procedures for the optimal selection of data sets from multiple crystals in macromolecular crystallography. *Acta Crystallogr D* **69**, 1617-1632 (2013).
113. I. Tickle, Staraniso: Use of a Webgl-Based 3-D Interactive Graphical Display to Represent and Visualise Data Quality Metrics for Anisotropic Macromolecular Diffraction Data. *Acta Crystallogr A* **75**, E162-E162 (2019).
114. A. J. Mccoy *et al.*, crystallographic software. *J Appl Crystallogr* **40**, 658-674 (2007).
115. P. Emsley, B. Lohkamp, W. G. Scott, K. Cowtan, Features and development of. *Acta Crystallographica Section D-Biological Crystallography* **66**, 486-501 (2010).
116. P. D. Adams *et al.*, The Phenix software for automated determination of macromolecular structures. *Methods* **55**, 94-106 (2011).
117. F. Neese, F. Wennmohs, U. Becker, C. Riplinger, The ORCA quantum chemistry program package. *J Chem Phys* **152**, (2020).
118. N. W. Moriarty, R. W. Grosse-Kunstleve, P. D. Adams: a tool for ligand coordinate and restraint generation. *Acta Crystallogr D* **65**, 1074-1080 (2009).